

6-7-2016

# Droplet-based Mechanical Actuator Utilizing Electrowetting Effect

Qi Ni

University of South Florida, qni@mail.usf.edu

Follow this and additional works at: <http://scholarcommons.usf.edu/etd>

 Part of the [Mechanical Engineering Commons](#)

## Scholar Commons Citation

Ni, Qi, "Droplet-based Mechanical Actuator Utilizing Electrowetting Effect" (2016). *Graduate Theses and Dissertations*.  
<http://scholarcommons.usf.edu/etd/6337>

This Thesis is brought to you for free and open access by the Graduate School at Scholar Commons. It has been accepted for inclusion in Graduate Theses and Dissertations by an authorized administrator of Scholar Commons. For more information, please contact [scholarcommons@usf.edu](mailto:scholarcommons@usf.edu).

Droplet-based Mechanical Actuator Utilizing Electrowetting Effect

by

Qi Ni

A dissertation submitted in partial fulfillment  
of the requirements for the degree of  
Doctor of Philosophy  
Department of Mechanical Engineering  
College of Engineering  
University of South Florida

Major Professor: Nathan Crane, Ph.D.  
Nathan Gallant, Ph.D.  
Rasim Guldiken, Ph.D.  
Julie Harmon, Ph.D.  
Andrés Tejada-Martinez, Ph.D.

Date of Approval:  
May 27, 2016

Keywords: EWOD, Fluid bearing, Surface tension, Micro actuator, Droplet force

Copyright © 2016, Qi Ni

## DEDICATION

To my parents and my lovely wife, who supported me throughout my academic endeavors.

## ACKNOWLEDGMENTS

Over the length of this project, many people provided their support to make this dissertation possible.

First and foremost, I would like to thank Professor Crane, my advisor and mentor whom guided me throughout my Ph.D. career. Dr. Crane's technical knowledge and expertise provided valuable guidance in every project that I have worked on. Professionally, his high standard and always-positive attitude made me push myself harder. Personally, his consistence and patience helped me to overcome my stubbornness. Never once, I was turned away from his office when I showed up unannounced - despite his busy work schedule. For this, I am forever grateful.

I would also like to acknowledge my committee members' contribution in evaluating the dissertation project, as well as the fruitful feedback and discussion during the project proposal. In addition, I want to thank Professor Harmon for agreeing to take part in this project evaluation at a moment's notice.

Colleagues such as Jose Carballo, Matthew Trapuzzano, Justin Nussbaum and Clayton Neff have all contributed to my project by sharing their knowledge and insight. My undergraduate peers such as Daniel Capecci and Millicent Schlafly provided valuable support to push the project forward.

I would also like to acknowledge the help and support from the staff members in the Nanotechnology Research and Education Center (NREC) here at the University of South Florida.

Mr. Richard Everly, has gone above and beyond to help me in all the fabrication both inside and outside of the cleanroom.

## TABLE OF CONTENTS

LIST OF TABLES .....	iv
LIST OF FIGURES .....	v
ABSTRACT.....	viii
CHAPTER 1: INTRODUCTION.....	1
1.1 Mechanical Actuators .....	1
1.1.1 Macro Actuators.....	2
1.1.2 Micro Actuators .....	3
1.2 Surface Tension-based Actuators .....	5
1.2.1 Phase Change Materials.....	5
1.2.2 Microfluidics.....	6
1.2.3 Electrowetting.....	7
1.3 Advantages of Using Electrowetting Droplets for Mechanical Actuation .....	8
1.4 Objective and Scope .....	9
1.5 Dissertation Outline .....	9
CHAPTER 2: LITERATURE REVIEW .....	11
2.1 Wetting Basics .....	11
2.2 Droplet Actuation Methods.....	12
2.2.1 Surface Tension Modification.....	12
2.2.1.1 Altering Liquid Surface Tension .....	12
2.2.1.2 Altering Solid Surface Tension.....	14
2.2.2 External Field.....	15
2.2.2.1 Leidenfrost Droplet.....	15
2.2.2.2 Vibration .....	16
2.2.2.3 Magnetic .....	17
2.2.2.4 Dielectrophoresis .....	18
2.2.2.5 Summary .....	18
2.2.3 Electrowetting on Dielectric .....	19
2.3 Electrowetting on Dielectric (EWOD).....	19
2.3.1 Basic Phenomena.....	19
2.3.2 Origin of the Electrowetting Effect.....	20
2.3.3 Equivalent Circuit Models .....	22

2.3.3.1	Grounded Droplet .....	22
2.3.3.2	Floating Droplet .....	23
2.3.3.3	Diode-based Circuits.....	24
2.3.3.4	Continuous Electrowetting.....	25
2.4	EWOD-based Actuators.....	25
2.4.1	Electrical Arrangement .....	25
2.4.2	Physical Arrangement.....	26
2.4.3	Control Method.....	26
2.4.4	Summary .....	27
2.4.5	EW-based Solid Actuation.....	28
2.4.5.1	Out of Plane Actuation.....	28
2.4.5.2	Horizontal Actuation.....	30
2.5	Area of Improvements Needed .....	30
2.6	Current Work's Contribution to EWOD-based Actuation.....	31
2.7	Conclusion .....	33
<b>CHAPTER 3: ELECTROWETTING ACTUATION FORCE.....</b>		<b>34</b>
3.1	Abstract .....	34
3.2	Introduction.....	35
3.3	Electrowetting Force.....	37
3.4	Experimental Setup.....	39
3.4.1	Electrowetting Force Measurement .....	39
3.4.2	Contact Angle Measurements .....	41
3.5	Results and Discussion .....	41
3.5.1	Direct Force Measurements .....	41
3.5.2	Contact Angle Measurements.....	42
3.5.3	Comparison between Measured Force and Calculated Force from Contact Angle .....	43
3.6	Considerations for Electrowetting Velocity.....	46
3.6.1	Free Deforming Droplet.....	47
3.6.2	Fixed-shape Droplet.....	48
3.6.3	Friction Effect .....	50
3.7	Conclusion .....	54
<b>CHAPTER 4: DROPLET MICRO-STEPPING USING ELECTROWETTING.....</b>		<b>55</b>
4.1	Abstract .....	55
4.2	Introduction.....	56
4.3	Background .....	59
4.4	Electrical Model and Simulation .....	62
4.5	Model Validation .....	66
4.6	Time Response.....	68
4.7	Accuracy and Repeatability .....	69
4.8	Conclusion .....	72
<b>CHAPTER 5: RELIABLE CONTINUOUS ELECTROWETTING USING DIODES.....</b>		<b>74</b>
5.1	Abstract .....	74
5.2	Introduction.....	75

5.3	Operating Principle .....	77
5.4	Electrochemical Diodes Combined with Schottky Diode .....	78
5.5	Materials and Fabrication .....	84
5.6	Electrical Measurements .....	86
5.7	Droplet Speed Testing.....	88
5.8	Actuation Reliability .....	90
5.9	Conclusion .....	92
CHAPTER 6: VERTICAL LOAD OF DROPLETS .....		93
6.1	Introduction.....	93
6.2	Normal Force Estimates.....	95
6.3	Simulation Results .....	99
6.3.1	Type 1 - Symmetrical Non-wetting .....	99
6.3.2	Type 2 - Defined Wetting Region.....	101
6.3.3	Type 3 - Constrained Top Wetting .....	102
6.4	Design Considerations and Application in Electrowetting-based Actuator .....	104
6.4.1	Design Case 1 - Fixed Gap Height .....	105
6.4.2	Design Case 2 - Fixed Stiffness and Droplet Diameter .....	107
6.5	Opposing Droplets .....	108
6.5.1	Design Case 3 - Droplets with Fixed Gap .....	111
6.5.2	Design Case 4 - Opposing Droplets with Fixed Gap and Preload (Reduced Gap Height) .....	112
6.6	Conclusion .....	113
CHAPTER 7: CONCLUSION AND FUTURE WORK .....		115
7.1	Key Contributions.....	115
7.1.1	Electrowetting Force.....	115
7.1.2	Novel Electrowetting Actuation-based on Diodes.....	116
7.1.3	Vertical Force and Stiffness Analysis.....	117
7.2	Future Work.....	118
7.2.1	Force and Velocity Considerations .....	118
7.2.2	Potential Applications and Future Directions .....	119
REFERENCES .....		121
APPENDIX A: COPYRIGHT PERMISSIONS .....		130
APPENDIX B: SURFACE EVOLVER SIMULATION CODE.....		136



## LIST OF TABLES

Table 1-1: Single stage MEMS positioners and their displacement range, resolution, and device footprint. ....	3
Table 2-1: Common EWOD setup and their performance characteristics. ....	27
Table 3-1: Surface tension values (mN/m) extracted from contact angle measurements. ....	43
Table 3-2: Measured electrowetting force and the friction force during actuation. ....	53
Table 4-1: Simulated voltages as a function of the capacitance of the left and right capacitors. ....	64
Table 4-2: The accuracy and the repeatability of the actuation system as a function of the step size. ....	71
Table 6-1: Simulation parameters used. ....	99
Table 6-2: Case study of droplet(s) supporting a fixed load at a constant gap height, the contact angle is 110° top and bottom. ....	106
Table 6-3: Case study of droplet(s) with constant stiffness (162 N/m); the contact angle is 110° on top and bottom. ....	108
Table 6-4: Case study of droplet(s) with constant height (1 mm) and wetting area. ....	112
Table 6-5: Case study of droplet(s) with constant height (0.5 mm), and wetting area. ....	113

## LIST OF FIGURES

Figure 2-1: Equilibrium force balance for a droplet sitting on a non-deformable solid. ....	12
Figure 2-2: Thermocapillary pumping (TCP) of drops of liquid. ....	13
Figure 2-3: Droplet actuation based on a solid surface tension gradient. ....	14
Figure 2-4: Schematic describing the motion of a droplet in the Leidenfrost state (hot surface). ....	16
Figure 2-5: Schematic of a droplet oscillating on a vibrating surface. ....	17
Figure 2-6: Grounded droplet with no top plate and its equivalent circuit configuration. ....	23
Figure 2-7: Floating droplet and its equivalent circuit configuration. ....	23
Figure 2-8: Diode-based continuous electrowetting and its equivalent circuit configuration. ....	24
Figure 2-9: Continuous electrowetting of a mercury plug in a channel and its equivalent circuit. ....	25
Figure 2-10: Schematics of the four steps for micromanipulation using the capillary micro-gripper. ....	29
Figure 2-11: Micro-conveyer system created by a floating EWOD configuration. ....	30
Figure 3-1: A square droplet is created by placing a square glass plate over it. ....	37
Figure 3-2: Force measurement setup. ....	39
Figure 3-3: Experimental procedure. ....	41
Figure 3-4: Measured electrowetting force vs. the applied voltage. ....	42
Figure 3-5: Measured contact angle vs. voltage applied. ....	42
Figure 3-6: The average of the measured electrowetting force is plotted against the average calculated force from the contact angle. ....	43

Figure 3-7: Measured unit force before saturation plotted against (a) electrowetting number ( $\eta$ ), left graph, (b) surface tension times electrowetting number ( $\gamma^*\eta$ ), right graph.....	45
Figure 3-8: Comparing the motion of free deforming droplets sandwiched between two plates during electrowetting actuation. ....	47
Figure 3-9: Plate speed under electrowetting actuation.....	50
Figure 3-10: Normalized friction force vs. velocity. ....	51
Figure 4-1: Proposed actuation scheme and its equivalent electrical circuit representation. ....	61
Figure 4-2: Top: the circuit representation of a co-planer electrowetting droplet with idealized diodes. ....	63
Figure 4-3: The measured plate position vs. duty cycle input. ....	67
Figure 4-4: Left: the position vs. time plot of the actuated plate under different step changes in duty cycle.....	69
Figure 5-1: Bi-directional continuous electrowetting principle.....	78
Figure 5-2: Illustration of the tube measurement setup. ....	80
Figure 5-3: The resulting actuation coefficient vs. the number of actuation cycles with 0.1 M concentration $\text{Na}_2\text{SO}_4$ .....	82
Figure 5-4: Peak current magnitude during cyclic tube tests for electrochemical alone and electrochemical plus Schottky diodes.....	84
Figure 5-5: Illustration of bi-directional actuation prototype. ....	86
Figure 5-6: Current-voltage measurements of the fabricated Schottky diodes.....	87
Figure 5-7: The average velocity of the droplet vs. the voltage. ....	89
Figure 5-8: Droplet centroid position vs. time for different applied voltages. ....	89
Figure 5-9: Cyclic droplet actuation. ....	91
Figure 6-1: Tensile and compressive forces from a capillary bridge formed by two parallel surfaces. ....	94
Figure 6-2: Capillary bridge between two parallel surfaces. ....	96
Figure 6-3: Surface evolver model of a droplet between two parallel surfaces.....	98
Figure 6-4: Normalized force vs. normalized height, type 1. ....	100

Figure 6-5: Force per unit area as the height changes. ....	101
Figure 6-6: Normalized force vs. normalized height, type 2. ....	102
Figure 6-7: Normalized force vs. normalized height, type 3. ....	103
Figure 6-8: Case study 1: fixed gap height (1 mm) and fixed load (1078 $\mu$ N). ....	105
Figure 6-9: Case study 2: fixed stiffness (162 N/m) and fixed droplet diameter. ....	107
Figure 6-10: Opposing droplet configuration. ....	109
Figure 6-11: Opposing droplet configuration for optimal stiffness and precise z-location. ....	110
Figure 6-12: Case study 3 and 4: these cases evaluate the two opposing droplet configurations, and the impact on stiffness. ....	111

## ABSTRACT

The goal of this work is to quantify the key design parameters such as the load capacity, actuation force, positioning repeatability, and reliability for droplet-based electrowetting actuators. Due to the fact that surface tension dominates gravity at both the mesoscale and microscale, droplet-based actuators can provide adequate force in manipulation tasks at those scales. Electrowetting, which uses an electric field to modulate the apparent surface tension of the liquid-ambient, provides a method to actuate droplets, which in turn transports the object carried by the droplet.

Most previous electrowetting actuation efforts have concentrated on manipulating droplets in a closed two-plate configuration. In these configurations, a voltage potential is applied between a series of electrodes. The droplets can merge, split, and mix with only a voltage input, and without any external machinery. While some mechanical actuation demonstrations have been done, limited studies have been performed to investigate the key actuation performance characteristics of droplet-based actuators carrying solid objects. Design criteria for using droplets to carry solid components are still not well defined.

The first part of this work provides fundamental understanding of the forces in electrowetting-based droplet actuation. The actuation force during electrowetting was experimentally validated according to the governing relation (Young–Lippmann equation) on a custom-designed testing apparatus. The results from the experiments show that the electrowetting actuation force is independent of surface tension below saturation, but the peak

force is proportional to surface tension. Higher surface/interfacial tension would increase the actuation force in the horizontal direction, as well as the speed of the actuator.

The second part of the dissertation demonstrates two actuation configurations based on electrowetting. The first actuator uses a droplet to carry a solid object and can be actuated in discrete steps to function as a micro-stepping linear motor. By implementing a leaky dielectric coating, the droplet/substrate contact area acts as an electrical diode. By varying the duty cycle of a square waveform, a range of droplet/part equilibrium position combinations are established. The underlying actuation mechanism was investigated and the position versus duty cycle relation was shown to be symmetrical but non-linear around the center of the electrodes. In contrast to the conventional electrowetting control scheme, the proposed actuation method required no feedback control loop while achieving a repeatability of less than 0.8% of the droplet diameter. Positioning matched a theoretical model based on idealized electrical elements to within 2.5% of the droplet diameter.

The second type of electrowetting actuation uses metal-semiconductor diodes (Schottky diodes) in place of electrochemical diodes. This configuration uses only one pair of electrodes to actuate the droplet over a large distance (5X or more the droplet diameter). While the actuation concept had been previously demonstrated, the reliability of the diodes were shown to be insufficient. The new diodes actuated without degradation under repeated actuation (2000 cycles). Comparing this to electrochemical diodes, a 50% reduction in actuation voltage was also accomplished by Schottky diodes. The measured maximum speed also increased from 32 mm/s (electrochemical diodes) to 240 mm/s (Schottky), a 7.5 fold improvement.

The last part of this dissertation used numerical simulations to investigate the load bearing capability and the stiffness variation of droplet-based actuators. The vertical force and

stiffness - which are the primary figure of merit in designing droplet-based actuators are quantified. Three types of loading conditions were analyzed using simulation software and a simple analytical equation is shown to provide a useful approximation of the droplet force and stiffness. The results were further used in various case studies to demonstrate the optimal design strategy when using an electrowetting driven droplet as a fluidic bearing.

## CHAPTER 1: INTRODUCTION

The goal of this dissertation is to quantify key parameters such as load capability, actuation force, and system resolution/repeatability of a droplet-based mechanical actuator using the electrowetting principle. In this chapter, challenges in designing and fabricating mesoscale actuators are presented. The motivation for using surface tension as an alternative to conventional methods to actuate solid objects is discussed. The objective of the dissertation is then listed with the outline of the manuscript.

### 1.1 Mechanical Actuators

Mechanical actuators take energy input and convert it into useful work. Their primary functions are to exert force/apply pressure, and/or provide translational/rotational motion. In order to meet different requirements, mechanical actuators cover a range of size scales ranging from larger than a building to smaller than a grain of rice. In the mesoscale - which typically ranges from a few millimeters to a few hundred micrometers - mechanical actuators are especially useful due to their ability to provide precise motion. Examples include precision stages, micro-manipulators and positioners. Mesoscale actuators are also useful in manufacturing processes due to the diminishing effectiveness of the manual assembly processes [1]. As the component's size becomes smaller than a millimeter, processes depending on human dexterity are no longer viable. Mechanical actuators provide precise and repeatable force and motion to improve dimensional tolerances and product quality.



For most micro/mesoscale actuators, the size of the actuator is many times larger than the range of motion they can provide, as well as the components they are manipulating. The following discussions will examine actuators by their applicable size scale and the design challenges when transferring either macroscale or microscale actuators to the mesoscale.

### **1.1.1 Macro Actuators**

Conventional mechanical actuators can achieve high precision while maintaining a large range of travel distance in the macroscale. As pointed out by Smith and Seugling [2], in precision macro actuators, the ratio of the range of motion to resolution is typically  $10^5$  or better. An example would be a high-end linear stage (Newport Corp. Model: UTS100CC) [3], which has a motion resolution of  $0.3 \mu\text{m}$  with 100 mm of travel (range to resolution:  $3 \times 10^5$ ). Typically, these actuators are much larger in size compared to the maximum travel they can provide. The same stage quoted earlier has dimensions of 350 x 105 x 32 mm, which is three times longer in length compared to the range of motion.

Advanced manufacturing techniques enable device miniaturization; machine components as small as a few hundred micrometers can be fabricated [4, 5]. However, simply scaling down the conventional actuators to reduce their size brings a new set of challenges. Physical phenomena such as material properties (bulk vs. thin film), surface tension and stiction forces become increasingly dominant below the millimeter range. Variation in the manufacturing processes can cause a change in physical properties - such as elastic modulus - which reduces device performance [6]. Surface tension effects can cause damage to components during fabrication [7]. Secondary forces such as electrostatic and capillary forces can cause contacting surfaces to adhere to each other, which reduces device reliability [8]. Most importantly, effective assembly methods (grasp and release, visual inspection) are still lacking below the millimeter

scale [1]. This in turn, limits the possibility of ever-smaller functional machinery being created by simple scaling.

Since some key characteristics in the macro world - such as gravity and inertia - may become insignificant when down-scaling [2]; implementing novel actuation principles would be necessary in order to reduce the device's footprint.

### 1.1.2 Micro Actuators

Micro Electromechanical Systems (MEMS) actuators have been developed to accommodate the need for compact and precise actuation. Driving mechanisms include electrostatics, piezoelectrics, thermal expansion and magnetics [6]. It was noted by Bell et al. that unlike macro actuators, the resolution of MEMS actuators relative to their maximum displacement is limited [9]. Most on-chip MEMS devices can achieve a resolution range less than one micrometer [9, 10], but only a few can provide a maximum displacement greater than one millimeter (which gives a range to resolution ratio around  $10^3$ ). When considering the total device footprint with respect to the maximum travel and resolution, MEMS devices are often much worse than macro actuators. The table below summarizes common MEMS positioning devices in terms of range of displacement, resolution, and device footprint (adapted from [10]):

Table 1-1: Single stage MEMS positioners and their displacement range, resolution, and device footprint. Adapted from REF [10]. \*Single stage actuator.

	Displacement ( $\mu\text{m}$ )	Resolution (nm)	Displacement to Resolution Ratio	Device Footprint ( $\text{mm}^2$ )
Electrostatic	0.5 - 160	1.5 - 1000	$10 - 5 \times 10^4$	0.1 - 100
Piezoelectric	1 - 200	1 - 500	$10 - 5 \times 10^4$	1 - 40000
Thermal	2 - 550	$\sim 14$	$\sim 10^2$	0.005 - 36
Magnetic	1 - 4000	4 - 1000	$7 - 2 \times 10^4$	0.04 - 4000

Part of the reason that travel range is limited in most MEMS devices is due to the fact that some MEMS operating principles do not scale well. For example, devices based on electrostatic forces (comb drive) utilize the high electric field generated between narrow gaps (fingers) to create motion. The same principle cannot be realized in the mesoscale due to the breakdown of the surrounding air at high potentials [7]. Additional linkages/compliant mechanisms have been implemented to amplify the range of travel [11], but they significantly increase the size of the actuation system.

Different physical driving mechanisms can affect device performance in different ways. Piezoelectric materials use an electric field to cause mechanical strain in crystals. The range of motion is often limited by the mechanical strength of the material; typical devices have a maximum travel of a few micrometers. An example would be a 20 mm long piezo stack that could only achieve a maximum displacement of 11.6  $\mu\text{m}$  (0.06% of piezo length) [10]. Thermal expansion based actuators have a demonstrated actuation frequency of around 500 Hz for a 300  $\mu\text{m}$  long beam in ref [12]. The authors concluded that the need to cool down between cycles limits the response time. Given the large surface to volume ratio in MEMS devices, the heat transfer rate would be expected to deteriorate if it were scaled up to mesoscale dimensions.

In theory, special implementations such as inchworm and scratch drive type devices could have a travel distance as large as the substrate while maintaining high accuracy. However, in practice, environmental conditions (dirt and humidity) limit their reliability [10].

In addition, most MEMS devices use semiconductor fabrication techniques employed in the integrated circuit (IC) industry. Typical processes use a layer by layer approach [7, 10]. The device layer thickness is limited to the micrometer range, which in turn, limits the out-of-plane travel distance of MEMS actuators. Furthermore, each additional layer in fabrication needs

several accompanying steps before moving on to the next layer. A functional MEMS-based actuator could take days or weeks to finish, which might increase the overall cost.

In summary, MEMS mechanical actuators can achieve high precision down to the nanometer range, but the maximum travel is limited below the millimeter range. It is necessary to implement non-traditional actuation mechanisms to extend the working range of currently available devices.

## **1.2 Surface Tension-based Actuators**

As discussed earlier, other physical phenomena such as electrostatic and surface tension forces have become increasingly dominant as the size scale decreases below the millimeter range. Using surface tension in the mesoscale has several advantages in comparison to other forces such as piezoelectrics and electrostatics. Surface tension force provides a wide operating range at different length scales, from millimeters to micrometers [13]. It is also very adaptable, either the fluid/air interface or the fluid/fluid interface can be utilized to create a capillary actuator [14]. Additional actuation mechanisms such as a magnetic field [15] could also be integrated into surface tension-based actuators to assist actuation. More importantly, the deformable fluid interface can provide compliance in fluidic joints to conform geometry irregularities of the component. This in turn eliminates the fixtures that are needed to connect the component to the actuator. As an added benefit, the compliant joint can also protect delicate components and reduce part damage during transportation.

### **1.2.1 Phase Change Materials**

The first process that took advantage of capillary force for positioning was the electronic manufacturers. Energy minimization of the liquid/air interface tends to keep the surface area to a minimum. By altering the wettability of the substrates (patterning metal islands on PCBs), the

surface tension of molten solder creates a restoring force when the parts are misaligned [16].

Developed by IBM in the 60's, surface mounting technology (SMT) enabled even more compact designs for circuit boards.

Due to the rapid miniaturization of computer processors, conventional wire bonding became increasingly inefficient. A sub-category of SMT, the Ball-grid-array (BGA), uses solder balls to connect the silicon chip to the contact pads. By applying thermal energy (reflow), the solid solder would transition to a liquid state. The capillary bridges formed support the weight of the chip and the surface tension forces align the chip to the pads with accuracy in the micrometer range [17].

Using capillary forces to perform mechanical actuation has been an intense research subject [12, 13, 18]. Phase change materials (mostly solder) have been used extensively in self-assembly processes due to their ability to aid in parallel processing [14]. This is done by patterning material in a non-equilibrium shape, such as a flat layer. When molten, the surface tension drives a shape change that provides actuation. Out-of-plane rotation and assembly of discrete components were demonstrated [19]. Since temperature is the control input, multiple locations could be actuated simultaneously; they are highly repeatable and reliable. One drawback is that capillary actuators based on phase change are not reversible processes, which means only single direction actuation is possible.

### **1.2.2 Microfluidics**

In the emerging field of microfluidics, capillary forces have been used to pump liquid [20], stop flow [21], and perform mechanical actuation such as grasp and release operations [22]. By introducing different channel geometries, liquid can be pumped through channels at different flow rates using the surface tension of the liquid. Similarly, an advancing liquid front in the

channel can be stopped by geometry constraints. Droplets have also been used to grasp and release millimeter-sized components by changing the interface curvature. However, specific geometry (channels) and chemistry (hydrophobic and/or hydrophilic surfaces) are usually required for those devices. Reversibility can also be an issue due to the irreversible wetting process.

### 1.2.3 Electrowetting

Various methods exist to modulate surface tension, common methods include thermal input, chemical additives (surfactants), and surface treatments (coatings, surface roughness) [1]. Electrowetting on dielectric uses electrostatic fields to change the shape of a liquid/ambient interface, and is also a commonly used method.

Electrowetting (EW) or electrowetting on dielectric (EWOD) is a technique used to modulate the apparent surface tension of a liquid/ambient interface. Modern electrowetting techniques usually use a thin insulating layer to separate the conducting droplet from the solid [23, 24]. When a voltage potential is applied between the droplet and the substrate, the electrical stress at the contact line between the liquid and solid causes the droplet to spread [25]. By creating a series of underlying electrodes that can be energized independently, asymmetric voltages can be applied and the resulting unbalanced forces would move the droplet that is in contact with the electrodes. Both linear [26] and rotational motion [27] are possible by implementing different electrode designs.

Prior work in electrowetting mainly concentrated on moving droplets for biological and diagnostic applications [28-30]. EWOD can perform merging, splitting, and mixing operations on a single device (lab-on-chip) with droplets ranging from microliters to nanoliters [31]. EWOD has also been used in optical technologies such as variable focus lenses [32], optical mirrors [33]

and electronic paper [34]. Variable focus lenses uses electrowetting to change the curvature of a fluid/fluid interface, which in turn changes the focal length. Electronic displays are made by adding different colorant to the actuating liquid, individual pixels can reflect lights and show different colors. Video speed electronic paper has been demonstrated [34].

### **1.3 Advantages of Using Electrowetting Droplets for Mechanical Actuation**

Surface tension can provide adequate force in size scales ranging from millimeters to micrometers. Electrowetting has proven to be a powerful method to modulate either discrete droplets or interface curvature [35]. It is highly repeatable and reversible. A variable focus lens reported [32] has switching cycle frequency greater than  $10^8$  [36]. It also has adequate response time for a given electrical input with reported droplet velocities as high as 250 mm/s [30]. In addition, the power requirements for electrowetting are extremely low due to the capacitive load. Common actuation voltage is around tens of volts [37, 38] and in extreme cases, actuation voltage as low as 1 volt has been demonstrated [39]. Electrowetting actuation can also supply fast response time while keeping manufacture fairly simple. In its simplest form, an electrowetting substrate can be fabricated by a single mask process to pattern the electrodes with the addition of a spun coated polymer to serve as dielectric.

Combining these characteristics, a droplet-based mechanical actuator using electrowetting can bridge the gap between macroscale and microscale.

Using droplets in mechanical actuation can reduce the device footprint by eliminating external fixtures. Small droplets can be used to carry components in similar size to the droplet itself. The range of motion of electrowetting-based actuators can be as large as the substrate. The resulting total size of the actuator could be comparable in size to the maximum travel of the device.

However, currently available electrowetting control is limited to single step (on/off) actuation and precision can only be gained through a feedback control loop, which usually complicates the fabrication scheme [40, 41]. In addition, little is known about the key mechanical actuation parameters like force, accuracy, repeatability, and stiffness.

#### **1.4 Objective and Scope**

Significant prior work has been done in characterizing electrowetting phenomena. However, the majority of the previous work has centered on the use of electrowetting to manipulate the liquid interface. Thus, the characterization is often in terms of the liquid interface shape (contact angle) and on configurations (Grounded top-plate) that are unsuitable for mechanical actuation. The objective of this dissertation is to characterize the key design parameters for a droplet-based actuator using electrowetting. The vertical load capability, the horizontal actuation force and its relation to the surface tension of the droplet, as well as the volume of the droplet will be examined in detail. Throughout this study, the relationship between the minimum required device footprint and maximum load will be established for designing such a device.

Furthermore, technical issues in electrowetting actuation - such as material reliability and control strategy - will be addressed. In addition, device prototypes will be built and tested to demonstrate the accuracy and repeatability of the proposed droplet actuators.

#### **1.5 Dissertation Outline**

The following chapter will first review methods that could be used to modulate surface tension and their advantages and drawbacks will be discussed. Then the electrowetting principle is reviewed. Various configurations used in electrowetting will be presented; their advantages



and drawback will be considered. Then a performance review of currently available droplet actuators based on electrowetting will be conducted.

Chapter 3 will present an experimental study on horizontal forces such as electrowetting actuation force and frictional force. The design parameters such as surface tension and actuation voltage requirements will be established.

Since current droplet-based actuators have relatively modest precision capabilities compared to mechanical actuators, chapter 4 will discuss a method to improve precision that is analogous to stepper motors with microstepping. The actuation mechanism will be analyzed and a theoretical relationship will be developed based on a simplified circuit model. The actuation accuracy and repeatability are presented.

Chapter 5 will present another novel electrowetting actuator which closely resembles a continuous linear servo motor. The reliability of the system will be demonstrated and the performance will be evaluated.

In chapter 6, the forces involved in the vertical direction will be investigated using numerical simulation (Surface Evolver). Key relationships between the droplet parameters (volume, surface tension, and wetting angles) and the system characteristics such as load capability, accuracy, and the optimal device footprint will be evaluated using both numerical and analytical studies of the droplets.

The last chapter (chapter 7) concludes the overall work and outlines the future work that is needed.

## CHAPTER 2: LITERATURE REVIEW

The overall goal of this dissertation is to characterize the key parameters in designing a droplet-based mechanical actuator using electrowetting. The previous chapter presented the challenges when designing actuators for mesoscale application. The electrowetting phenomenon was proposed to serve as a driving mechanism to transport droplets which could support solid objects. This chapter will first discuss other droplet actuation methods, their actuation principles, and their performances will be reviewed. Then, the electrowetting principle and common configurations will be presented. Finally, advantages/disadvantages of droplet-based actuators, which use electrowetting, will be discussed. The key areas that need improvement will be identified.

### 2.1 Wetting Basics

For a droplet sitting on a solid, non-deformable surface, the two-dimensional force balance is demonstrated in Figure 2-1. At the point of contact, the surface tensions ( $\gamma_{12}$ ,  $\gamma_{23}$ ,  $\gamma_{13}$ ) are balanced as shown by the Young's equation:

$$\cos(\theta_{app}) = \frac{\gamma_{13} - \gamma_{23}}{\gamma_{12}} \quad \text{Equation 2-1}$$

where  $\gamma_{13}$ ,  $\gamma_{23}$ , and  $\gamma_{12}$  are the surface tensions (N/m) of solid-ambient, solid-liquid, and liquid-ambient, respectively. The resulting apparent contact angle ( $\theta_{app}$ ) is the wedge formed between the solid and liquid. The ambient fluid can be either liquid or vapor.

Various methods have been used to change either the surface tension or the apparent contact angle in order to manipulate droplets, the discussion below will examine a few commonly used techniques.

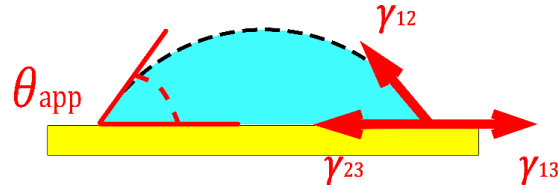


Figure 2-1: Equilibrium force balance for a droplet sitting on a non-deformable solid.  $\theta_{app}$  is the resulting apparent contact angle formed.  $\gamma_{13}$ ,  $\gamma_{23}$ , and  $\gamma_{12}$  are the surface tensions of solid-ambient, solid-liquid, and liquid-ambient, respectively.

## 2.2 Droplet Actuation Methods

Other than electrowetting, methods used to actuate discrete droplets in planer fashion can be further divided into two sub-categories by their actuation principles. The first group directly modify either the liquid-ambient surface tension or the solid-liquid surface tension. The second group uses external stimulants to apply force to the droplet. We will first review the direct modification approach.

### 2.2.1 Surface Tension Modification

#### 2.2.1.1 Altering Liquid Surface Tension

Thermocapillary pumping uses localized heating to create droplet motion [42]. For most liquids, higher temperature will result in lower surface tension. Non-homogeneous heating can cause a surface tension gradient between the hot and cold end of the droplet. The resulting motion depends on the wetting condition of the substrate. If the substrate is hydrophilic (wetting is preferred by the liquid), the droplet is pumped to the cold spot (Figure 2-2, a). If the substrate

is hydrophobic (non-wetting), the droplet is pumped to the hot spot (Figure 2-2, b). Darhuber et al. embedded a series of resistive heaters on a substrate; when the heaters were turned on sequentially, droplets were moved in a predefined path [43]. Alkanes, poly(ethylene glycol) and water actuation were demonstrated. Kotz et al. used a laser to heat one side of a droplet that was sitting on a polystyrene surface (non-wetting). The reported maximum velocity was 3 mm/s for droplet volumes ranging from 14 picoliter to 1.7 microliter [44].

As pointed out by Jiao and co-workers [45], thermocapillary driven actuation is better suited for non-aqueous liquids, because for aqueous solutions the surface tension and temperature dependency is rather weak comparing to other non-aqueous liquids. For mechanical actuators based on droplets, thermocapillary effects are not the ideal actuation principle due to the slow response time of the droplets.

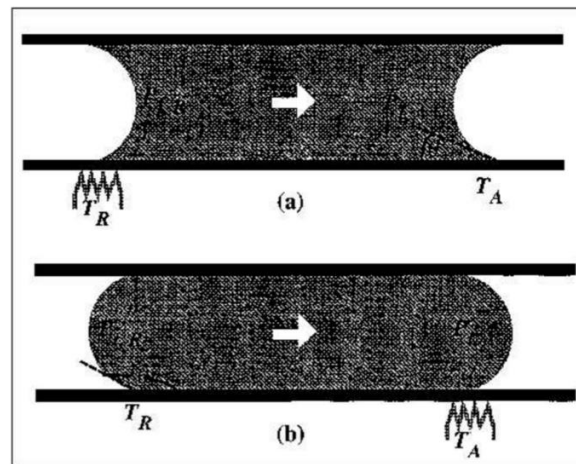


Figure 2-2: Thermocapillary pumping (TCP) of drops of liquid. In (a) hydrophilic (contact angle less than  $90^\circ$ ) substrates and (b) hydrophobic (contact angle greater than  $90^\circ$ ) substrates.  $T_a$  and  $T_r$  are the advancing and receding ends of the droplets. Reprinted with permission from [42]. Copyright John Wiley and Sons. Copyright permission is included in the appendix.

### 2.2.1.2 Altering Solid Surface Tension

Since all three surface tensions at the liquid-solid contact line balance each other, it is also possible to actuate droplets by modifying the liquid-solid surface tension either chemically or mechanically (see Figure 2-3).

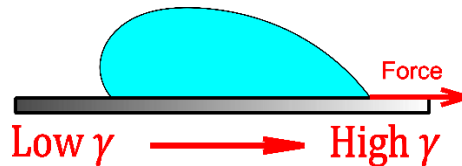


Figure 2-3: Droplet actuation based on a solid surface tension gradient. The liquid-solid surface tension ( $\gamma$ ) varies spatially from left to right, and the non-symmetric wetting causes droplet motion.

Chemical coatings such as self-assembled monolayers (SAM) [46] and fluorinated polymers [47] can render hydrophilic (wetting) surfaces hydrophobic (non-wetting). One way to create a liquid-solid surface tension gradient is to induce a chemical concentration difference across a surface. Chaudhury and Whitesides used a diffusing vapor front of decyltrichlorosilane ( $\text{Cl}_3\text{Si}(\text{CH}_2)_9\text{CH}_3$ ) to create a surface tension gradient over a 10 mm distance on a silicon wafer. The absorbed vapor on the silicon surface resulted in a concentration gradient on the silicon wafer. The resulting contact angle of water changed from  $97^\circ$  to  $25^\circ$  as the concentration of the absorbed vapor decreased [48]. Droplets of water between 1 to 2  $\mu\text{L}$  were used to demonstrate the mobility, and the reported velocity was approximately 2 mm/s.

Another approach to create a surface tension gradient is by patterning narrowing geometry on a solid surface. Bliznyuk and co-workers used lithography techniques to pattern rectangular stripes of self-assembled monolayer (SAM) on a silicon dioxide wafer [49]. As the strip's pattern width changes, a surface tension gradient was created along the direction of the strip. A droplet of glycerol/water mixture (2  $\mu\text{L}$ ) covered a distance of 3 mm in one second.

Mechanically induced surface roughness can also alter the wetting behavior of a liquid on a solid. Sun et al. used laser etching combined with a surface treatment (SAM) to pattern a silicon surface. The resulting surface roughness created a single direction surface tension gradient over a 6 mm distance [50]. Water droplets as large as 10  $\mu\text{L}$  were actuated with velocity of around 3 mm/s. Yang and co-workers used lithography-defined polymers (photoresists) to create similar structures. The reported average velocity of their droplet was much higher ( $\sim 62.5$  mm/s) due to the non-wetting surface property of the polymer [51].

A surface tension gradient on a solid substrate can be used to propel liquid droplets at low to moderated speed. However, one major drawback is that the actuation distance is limited due to the static friction at the contact line (also called contact angle hysteresis) [48]. More importantly, the process is not reversible due to the wetting process (the droplet transit from a higher energy state to a lower energy state). As for mechanical actuation, modifying the surface tension of either liquid or solid is not the ideal approach.

## **2.2.2 External Field**

### **2.2.2.1 Leidenfrost Droplet**

When a droplet is in contact with a solid surface at elevated temperature (above the boiling temperature of the liquid), a vapor film is created between the droplet and the solid; this is termed the Leidenfrost effect. The vapor film can support the droplet while providing a near-ideal frictionless contacting surface [52]. As a result, very little force is needed to propel and sustain the motion of the droplet. By introducing directional surface roughness (ratchet type surface) [52, 53], droplets can be actuated on hot surfaces by the non-symmetric vapor pressure (see Figure 2-4). By patterning different scales of roughness, actuation distance and velocity as high as 100 mm and 400 mm/s, respectively, were reported [54].

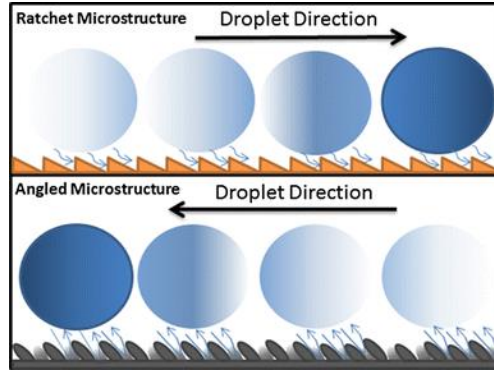


Figure 2-4: Schematic describing the motion of a droplet in the Leidenfrost state (hot surface). The directionalities shown correspond to a conventional ratchet surface and the angled surface formed via femtosecond laser surface processing (FLSP). Reprinted with permission from [53]. Copyright permission is included in the appendix.

Although capable of high speed and large actuation distance, Leidenfrost droplets will have to rely on specific substrate patterning as well as a uniform high surface temperature (200° C for water droplets in [53]). The major drawback for this type of actuation is that the droplet's position cannot be controlled effectively. Once the droplet is in contact with the surface, the droplet starts to move along the designed path. Neither position holding nor reversible motion is possible. This eliminated the possibility of using Leidenfrost droplets as a droplet-based mechanical actuator.

#### 2.2.2.2 Vibration

External vibrations can be applied directly to the substrate by external oscillators [55]. Under periodic lateral vibration, the competing forces such as contact angle hysteresis and the bulk inertial force cause the droplet/ambient interface to deform. The resulting pressure difference within the droplet could be adjusted by changing the waveform shape, the input amplitude, or the frequency (see Figure 2-5).

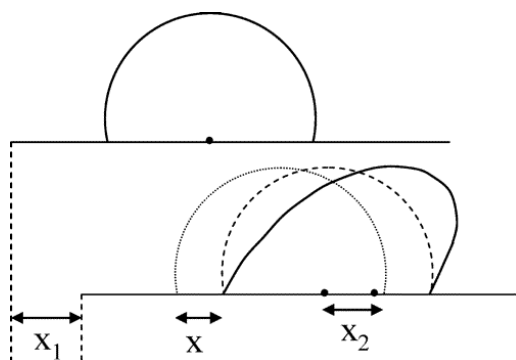


Figure 2-5: Schematic of a droplet oscillating on a vibrating surface. The upper diagram shows the static droplet profile before the substrate moves. In the lower diagram, the undisturbed profile of the drop is shown by the dashed gray line, whereas its new profile is shown by the solid line.  $x_1$  indicates the displacement of the substrate during oscillation,  $x$  is the displacement of the contact line with respect to the plate, and  $x_2$  is the displacement of the droplet's center of mass. The new position of the droplet with respect to its old depends on the phase shift that occurs near resonance; i.e., it is possible for  $x$  and  $x_2$  to be either positive or negative. Reprinted with permission from [55]. Copyright 2005 American Chemical Society. Copyright permission is included in the appendix.

A more elaborate setup integrated side wall ratchets and vibration to sequentially move the droplets on a planer surface [56]. The reported maximum velocity was 100 mm/s.

Surface acoustic waves (SAW) have also been used to induce a pressure difference within a droplet. Limited by the small amplitude (nanometer range) of the substrate surface, applicable droplet size was confined in the nanoliter range [57].

Vibration induced droplet actuation can move droplets large distances and is also reversible. But, the required external fixture and oscillator would increase device size. In addition, droplet velocity is very sensitive to operating parameters such as frequency, amplitude, and droplet volume. Initial optimization of the device is required.

### 2.2.2.3 Magnetic

Liquids containing magnetic nano-particles (ferrofluids) are essentially a liquid magnet which responds to an external magnetic field [58]. Using permanent magnets combined with



electromagnets, Nguyen et al. demonstrated linear motion of a ferrofluid droplet. The average velocity was approximately 0.4 mm/s [59]. Probst et al. arranged four electromagnets in a square pattern, and 2D spiral motion was achieved by controlling the currents in the electromagnets [60]. Limited by the speed of the actuation and the applicable fluids that can be used, magnetic field driven droplet actuation is not suitable for droplet-based actuators.

#### **2.2.2.4 Dielectrophoresis**

Similar to electrowetting, dielectrophoresis (DEP) droplet actuation uses an electric field to actuate droplets. When a droplet with finite conductivity is placed in an electric field, both the conductivity and the permittivity of the droplet will influence the force exerted on the droplet [61, 62]. A net force on the droplet is developed when the applied field is non-homogeneous. The resulting force can be used to move a droplet in 2D space. Gascoyne and co-workers used CMOS technology and fabricated a multilayer substrate. The substrate included voltage switching circuits which were buried under the electrodes. The reported velocity was 0.6 mm/s for a 0.3 nL droplet [61].

Unlike electrowetting, DEP-based actuation does not require physical contact between the actuating electrodes and the droplet. This indicates the possibility of actuating droplets in 3D space. However, in practice, this is very difficult to implement due to the effect of gravity. Also, the fabrication is fairly complicated due to the stringent requirements for individually addressable electrodes.

#### **2.2.2.5 Summary**

The above discussion reviewed a range of droplet actuation methods, their working principles, and their performances. Reversibility, droplet speed, and response time were the main

obstacles which limited their potential to be used as actuation mechanisms for droplet-based mechanical actuators. The following section will discuss electrowetting on dielectric in detail.

### **2.2.3 Electrowetting on Dielectric**

The above mentioned limitations such as reversibility, actuation force and speed, as well as the system response time imposed by other droplet actuation methods can be solved by using the electrowetting principle. Electrowetting on dielectric uses an external electric field to change the apparent contact angle of a droplet sitting on a solid. Usually a thin dielectric layer is used to separate the conducting liquid from the substrate to avoid electrochemical reactions. Upon voltage application between the liquid and solid, the electrical stress imposed on the contact line causes the droplet to spread [23, 24]. By embedding electrodes into the substrate, asymmetric voltage can be applied to the two sides of the droplet to create motion. Electrowetting actuation is highly reversible, it can provide large actuation force from the micro to millimeter scale. The response time is usually on the order of milliseconds [63]. It can also actuate a droplet over a large distance [64]. It is simple to fabricate, as single mask lithography can be sufficient [37]. EWOD also does not impose stringent requirements on the fluid—as long as the droplet is conductive [65]. The following discussion will review the principle of electrowetting on dielectric and its common configuration in detail.

## **2.3 Electrowetting on Dielectric (EWOD)**

### **2.3.1 Basic Phenomena**

Electrowetting originally referred to the change of the interface curvature in response to an applied voltage in a mercury/electrolyte system [66]. Modern electrowetting usually uses a thin dielectric layer to separate the conducting liquid and the electrode underneath. Upon the

application of the voltage, the electrical stress around the contact line causes the droplet to spread. Although the true contact angle does not change on the microscopic scale, the macro-apparent contact angle reduction is usually used to quantify the electrowetting response. Under the assumption that the characteristic length of the system is much less than the capillary length, gravity is neglected.

The relationship between the zero voltage contact angle ( $\theta_0$ ), the contact angle under applied potential ( $\theta_{EW}$ ), and the applied voltage ( $V$ ) is captured by the Young–Lippmann equation:

$$\cos(\theta_{EW}) - \cos(\theta_0) = \frac{\epsilon_0 \epsilon_r}{2\gamma d} V^2 \quad \text{Equation 2-2}$$

where  $\epsilon_0 \epsilon_r$  is the dielectric constant,  $d$  is the dielectric thickness, and  $\gamma$  is the surface tension of the liquid/ambient interface. Under applied voltage, the contact angle decreases until it reaches a limit, beyond which additional voltage could not reduce the contact angle any further. This is termed contact angle saturation. The mechanism that causes this phenomenon is still under debate [67, 68], but the primary possible mechanisms could be either dielectric break down and/or droplet charging.

The dimensionless electrowetting number is defined as  $\eta = \frac{\epsilon_0 \epsilon_r}{2\gamma d} V^2$ , which can be interpreted as a ratio of the capacitive energy per unit area to the interfacial energy. The response is identical for both positive and negative charges to the first order. However, variations are commonly observed due to effects such as ion trapping in the dielectric [69, 70].

### 2.3.2 Origin of the Electrowetting Effect

Jones [71] provided a simple approach to derive the electrowetting force. The electrical energy input can be related to the mechanical force output using a “co-energy” function. When

the input voltage is controlled, a capacitor is formed between the droplet and the electrode - the droplet is the other electrode with variable surface area. The change in the energy of the system is then related to the change in the capacitance ( $C(r)$ ) in terms of droplet/substrate contact area. If circular symmetry is assumed, the droplet radius ( $r$ ) can be used in the following equation:

$$d(U_{electrical}) = \frac{V^2}{2} * dC(r) = \frac{\epsilon_0 \epsilon_r}{2d} V^2 * dA = \frac{\epsilon_0 \epsilon_r}{d} V^2 * \pi r dr \quad \text{Equation 2-3}$$

On the other hand, the mechanical force acts in the direction parallel to the substrate at the vicinity of the contact line. The droplet deforms and the contact area changes. The force per unit contact line can also be formulated by the principle of virtual work:

$$d(U_{electrical}) = -f_{electrical} da = -f 2\pi r dr \quad \text{Equation 2-4}$$

Since the competing energies are balanced at equilibrium ( $d(U_{mechanical}) - d(U_{electrical}) = 0$ ); we have:  $f_{electrical} = \frac{\epsilon_0 \epsilon_r}{2d} V^2$ . Adding this additional outward force to the force balance at the contact line we get:

$$\cos(\theta_{EW}) = \frac{\gamma_{23} - \gamma_{13} + f_{electrical}}{\gamma_{12}} \quad \text{Equation 2-5}$$

where  $\gamma_{12}$ ,  $\gamma_{23}$ , and  $\gamma_{13}$  denote the interfacial tension of liquid/ambient, liquid/solid, and ambient/solid, respectively. Combining Equation 2-5 with Young's equation for a droplet in equilibrium,  $\cos(\theta_{EW}) = \frac{\gamma_{23} - \gamma_{13}}{\gamma_{12}}$ , we have:

$$\cos(\theta_{EW}) = \frac{\gamma_{23} - \gamma_{13} + f_{electrical}}{\gamma_{12}} = \cos(\theta_0 + \frac{\epsilon_0 \epsilon_r}{2d} V^2) \quad \text{Equation 2-6}$$

The electromechanical approach described above considers only the system capacitance without knowledge of the contact angle. It is important to note that the interfacial tension does not vary with respect to the applied voltage. The force per unit contact line length can be

calculated by simply measuring the change in apparent contact angle with respect to the applied voltage by using the following equation:

$$f = [\cos(\theta_{EW}) - \cos(\theta_Y)] * \gamma_{12} \quad \text{Equation 2-7}$$

### 2.3.3 Equivalent Circuit Models

Many possible configurations can be implemented in electrowetting on dielectric. Other than DC signal input, AC signal can also be used in actuation. An input frequency in the 1–5 kHz range is often used. When analyzing AC input, the RMS voltage is used with the Young-Lippmann equation. Below are some common arrangements and their representative circuit models using lumped circuit elements.

#### 2.3.3.1 Grounded Droplet

The grounded droplet is the most common configuration. A thin dielectric layer covers the individual bottom electrodes with one having an opening (Figure 2-6). When a voltage potential is applied to the electrodes, the droplet moves to the electrodes with no defect and covers that electrode fully. Continuous motion requires a grounding wire from the top, which is usually done with a metal coated plate that has a hydrophobic layer. For continuous motion, multiple electrodes need to be turned on and off sequentially. Sawtooth boundaries on the neighboring electrodes are necessary to facilitate reliable droplet motion - the droplet has to be touching at least two electrodes at any given time in order to move. Electrical ground can also be provided from the bottom dielectric layer [72]. The voltage across the dielectric does not change with displacement of the droplet. This creates a strong alignment force that improves the accuracy and repeatability of the fluid position.

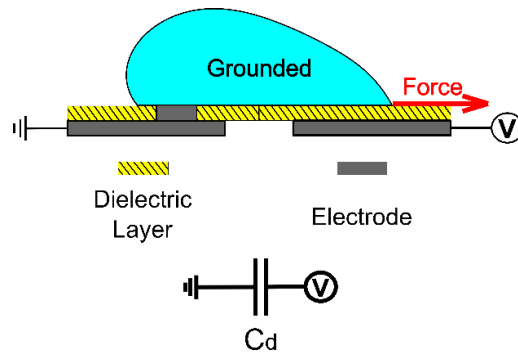


Figure 2-6: Grounded droplet with no top plate and its equivalent circuit configuration.  $C_d$  is the capacitance of the dielectric. Adapted from [73]

### 2.3.3.2 Floating Droplet

The floating droplet uses the voltage difference between the activated electrodes to move the droplet; the droplet is insulated from both electrodes. The equivalent circuit used here has two capacitors connected in series (Figure 2-7). When potential is applied to one of the electrodes, the droplet tries to cover both electrodes to minimize the surface energy [74]. The centering of the droplet could provide precise positioning control of the droplet. However, the actuation force is highly dependent on the location of the droplet - the further away the droplet is from the electrodes' center position, the higher the actuation force. Conversely, when the droplet is near the center position, the actuation force may be too low to overcome the static friction. This could introduce additional error in positioning.

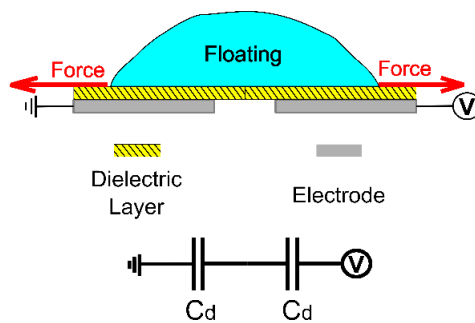


Figure 2-7: Floating droplet and its equivalent circuit configuration.  $C_d$  is the capacitance of the dielectric. Adapted from [73]

### 2.3.3.3 Diode-based Circuits

Diode-based electrowetting circuits use the electrochemical effect between the metal substrate and the working electrolyte to create polarity-dependent actuation properties. Under voltage application, valve metals such as aluminum and titanium in contact with an electrolyte, could either be passivated (forming oxide) or etched, depending on the voltage polarity. When an oxide forms, the current is blocked by the newly formed layer. This mechanism has been used to improve the reliability of the electrowetting system [75]. The most useful equivalent circuit for actuation is composed of two diodes and two capacitors (Figure 2-8). One diode is connected in parallel with one capacitor and another identical pair is then connected to it back-to-back so one is always reversely biased (no current flow). Depending on the polarity of the applied voltage, the droplet will move towards the higher potential side [26]. This type of setup has the advantage of using a single pair of electrical inputs to achieve large travel distance (5X or more of the droplet diameter), and was demonstrated [76]. However, specific combinations of fluid/metal have to be used even though detailed investigation shows that isolated electrochemical diodes could be reliable under repeated actuation, no actual device has been demonstrated to be so [77].

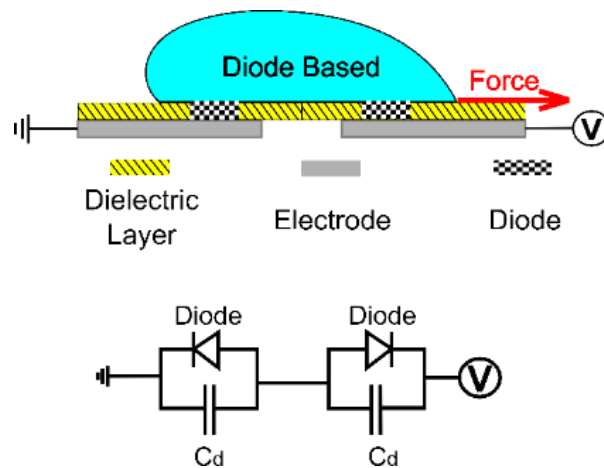


Figure 2-8: Diode-based continuous electrowetting and its equivalent circuit configuration.  $C_d$  is the capacitance of the dielectric. Adapted from [73].

### 2.3.3.4 Continuous Electrowetting

The continuous electrowetting effect modulates the electric double layer of a mercury/electrolyte interface [78]. A mercury plug is embedded in a microfluidic channel (Figure 2-9). When a voltage is applied to the two ends of the channel, the charged double layer changes the interface curvature. The advantage of this type of actuation is similar to the diode-based circuits - only 2 electrodes are needed to propel the droplet across a large distance. However, geometrical requirements (closed channels and additional reservoirs for fluid exchange) impose additional challenges. Also, due to the use of toxic material (mercury), the application area of continuous electrowetting is still limited.

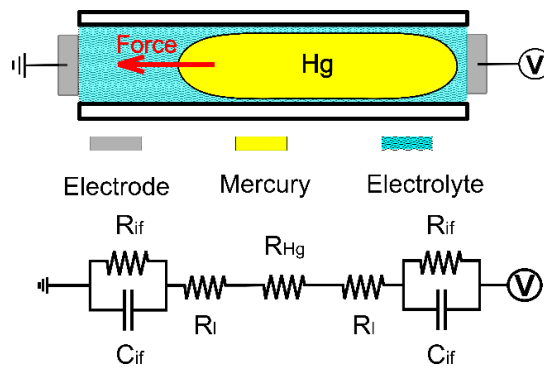


Figure 2-9: Continuous electrowetting of a mercury plug in a channel and its equivalent circuit.  $R_i$  and  $R_{Hg}$  are the resistance of the mercury plug and the liquid electrolyte.  $R_{if}$  and  $C_{if}$  are the interfacial resistance and capacitance, respectively. Adapted from [73]

## 2.4 EWOD-based Actuators

### 2.4.1 Electrical Arrangement

Electrowetting is a versatile tool that can be used to manipulate discrete droplets on a planar surface [24, 66]. Electrically, floating or grounding configurations can be used. For a floating droplet, the actuation force per unit contact line is position dependent (see section 2.3). Upon voltage application, the droplet will center itself between the two electrodes (see Figure 2-7). Larger deviations of the droplet from the center position will result in a larger actuation



force. For grounded droplets, the actuation force per unit contact line is constant with position [73]. When a voltage is applied to the actuating electrode, the droplet will cover the electrode fully (see Figure 2-6).

For both cases, the size of the electrode determines the step size. For floating configuration, the droplet has to cover at least three electrodes in order to move continuously, while grounding the droplet only needs two.

### **2.4.2 Physical Arrangement**

The grounding approach is favored due to a constant, maximum actuation force compared to the position dependent force of a floating droplet. Physically, either closed or open configurations can be used when implementing electrowetting. Closed configuration uses a top plate to sandwich the droplet between the top plate and the bottom substrate. The top plate could also be used to provide an electrical ground from above [79]. On the other hand, open configuration uses the bottom substrate only. In order to implement grounded actuation, which provides the maximum actuation force, multilayer fabrication is needed. Cooney et al. demonstrated a ground-from-below approach which employed additional metal lines on top of the dielectric layer as grounding wires [72].

For droplet-based actuators, an electrically grounded droplet with open configuration is an attractive method. The droplet can be actuated from the bottom substrate while carrying a solid object on top. In order to have a low cost and efficient droplet-based actuator, the drawback in the fabrication requirement will need to be addressed.

### **2.4.3 Control Method**

To be able to control the droplet's position, either open or closed loop control can be used in EWOD actuation. Open loop control requires optimization of the voltage input pattern. The

electrodes can be energized sequentially to achieve motion [78]. One problem is that if the droplet's motion and the input were out of sync (say a missed step) or if the output force is too large and the droplet overshoots, the device would stop functioning all together [78].

Closed loop control requires feedback such as capacitance measurement [40] or real-time imaging. In capacitive monitoring, a low voltage AC signal can be used to probe the droplet's location on an electrode. Typical setup requires closed configuration to keep the linear relationship between the capacitance changes with respect to the footprint of the droplet. Additional hardware is needed which would likely increase the device's size and overall cost.

#### 2.4.4 Summary

To summarize electrowetting-based actuation, the following Table 3-2 is constructed to list basic types of EWOD droplet actuations. Their performance characteristics are listed in the "remarks" column.

Table 2-1: Common EWOD setup and their performance characteristics. The physical configuration of "open" and "closed" refers to with or without a top cover plate, respectively.

Electrical Configuration	References	Physical Configuration	Remarks
Floating	[64, 80]	open	Reliable but less repeatable due to position dependent actuation force. Special electrode geometry is needed.
Grounded	[31, 40, 81]	closed	High precision with feedback which requires a top plate. Grounding from below needs multilayer and through hole, no feedback has been shown.
Continuous	[78, 82, 83]	closed channel	Fast and reliable, but uses mercury.
Diode-based	[26, 76]	open	Simple wiring, but reliability is an issue

For actuating solid objects, it is preferred to use a grounding droplet with an open configuration. The discussion below will list works by others using EWOD to actuate solid objects.

#### **2.4.5 EW-based Solid Actuation**

The prior works reviewed above have been concentrated mainly on transporting droplets by electrowetting actuation. A few researchers have been looking into using droplets to perform mechanical actuations.

##### **2.4.5.1 Out of Plane Actuation**

When a capillary bridge is formed between two parallel surfaces, EWOD can be used to change the shape of the capillary bridge, which in turn results a vertical tension force between the two surfaces. Vasudev and Zhe used EWOD to control the curvature of a droplet hanging from above. When the droplet came into contact with a solid sphere (~14 mg), the capillary bridge formed between the two solid surfaces could grasp the sphere. When the applied voltage was decreased, the change in curvature caused a lower gripping force, and the sphere was released (see Figure 2-10: Schematics of the four steps for micromanipulation using the capillary micro-gripper.) [84].

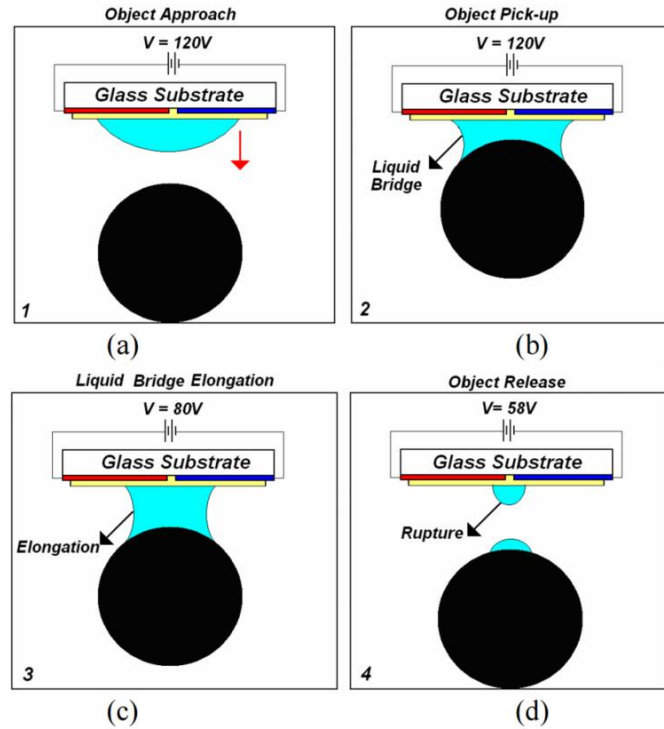


Figure 2-10: Schematics of the four steps for micromanipulation using the capillary micro-gripper. Reprinted with permission from [84]. The copyright agreement is attached in the appendix.

Another example of using EWOD to modulate the capillary bridge is demonstrated by Wang et al [85]. The authors used MEMS fabrication methods to create a cavity which was filled by liquid. When EWOD was applied on the bottom surface, the increased contact area on the bottom caused a vertical downward force on the top surface. The measured actuation force was around  $200 \mu\text{N}$ . The authors stated that a parallel plate electrostatic actuator of the same size could only generate  $3 \mu\text{N}$  of force which was over 60 times less than a capillary actuator.

Knospe *et al.* also investigated the actuation of EWOD in the vertical direction by means of a numerical study [86]. The authors concluded that the maximum stable displacement of the capillary bridge is about one third of the nominal bridge height, which is much greater than similar parallel plate actuators.

### 2.4.5.2 Horizontal Actuation

When using droplets to carry solid objects, EWOD can also be used to achieve horizontal motion. Moon and Kim used a floating configuration to move droplets across patterned electrodes and created a conveyor system (see Figure 2-11, left) [64]. Four 6 microliter sized droplets were used carry loads up to 180 mg. However, the authors did notice that if the droplet was sitting in-between two adjacent electrodes (Figure 2-11, top right), the symmetric forces on either side of the droplet would block the motion. One solution was to implement finger like geometry to the electrodes as shown in Figure 2-11, bottom right.

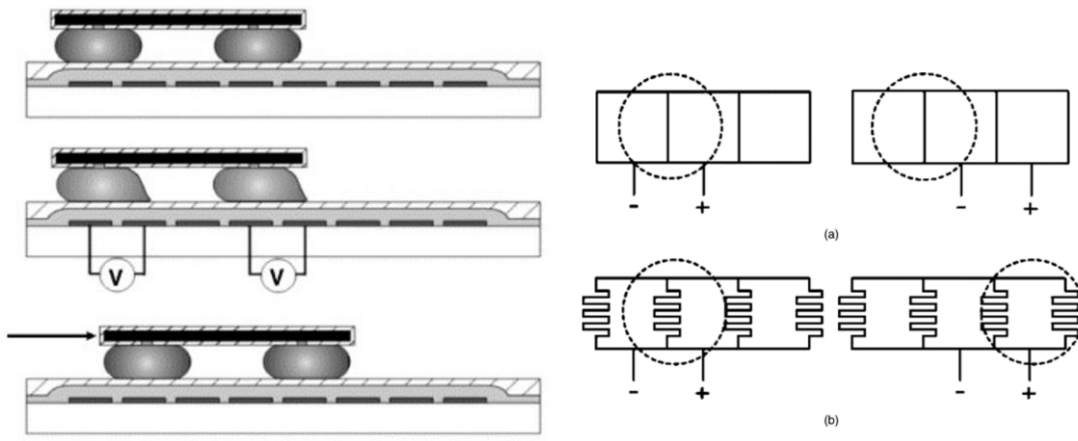


Figure 2-11: Micro-conveyor system created by a floating EWOD configuration. Left: droplets carrying a plate. Top right: droplet unable to move. Bottom right: New design to enable motion. Reprinted with permission from [64], the copyright agreements are attached in the appendix.

## 2.5 Area of Improvements Needed

While the prior work has demonstrated that EW can be used to actuate solid objects, critical knowledge is missing, which limits wider use of EW actuation. For example, the above work concentrates on the vertical actuation force and is largely limited to the tension force of a concave capillary bridge. For droplet-based actuators, the droplets are used to support a solid

object, and the shape of the capillary bridge would likely be convex when the load is compressive. It is important to understand the load capability in the vertical direction, as well as the actuation force in the horizontal direction. The load capability will determine the device footprint, as well as the efficiency of the actuator; the horizontal force will determine the speed and the accuracy of the actuator. In addition, current EWOD technology uses relatively coarse step control for droplet positioning. Precise positioning requires feedback control which increases the device footprint. It would be ideal if fine positioning could be maintained without feedback control.

## **2.6 Current Work's Contribution to EWOD-based Actuation**

Current EWOD-based actuators can achieve high force in the vertical direction [86]. Fine positioning in the horizontal motion is also possible with the help of a feedback control loop [40]. However, some key understandings are still missing.

As discussed in section 2.3, several approaches can be used to calculate the EWOD actuation force. While a few indirect methods are available to quantify the actuation force during electrowetting [62, 87, 88], only one direct electrowetting force measurement was reported previously [89]. Additionally, the most widely used measurement technique is to measure the apparent contact angle change under EWOD actuation. However, the difference in advancing contact line and the receding contact line (contact angle hysteresis) can impose significant resistance to contact line motion. Due to the fact that virtually all surfaces are rough, contact angle hysteresis is unavoidable [90]. Variations between the advancing and receding contact angles ( $\sim 10^\circ$ ) have been reported in electrowetting literature [91], and much larger are possible. This in turn, affects the results of EWOD force approximation.

This work reports on the design and testing of a custom-built EWOD actuation measurement apparatus, which directly measures the force output during actuation. The theoretical basis for the method, and an early implementation are reported [89].

Once the actuation force is validated, this work further refines the diode-based actuation developed in our lab previously [76, 77]. It is favorable to use a grounded configuration in mechanical actuation because it can provide maximum force, and the force is also independent of the location of the droplet. This provides constant actuation force as long as the applied voltage remains the same. However, when the droplet is used to carry a solid object, it is problematic to provide electrical connection from above. Grounding from below would require a multilayer approach with through holes that would complicate fabrication. Also, currently available EWOD needs electrical feedback for precise positioning [40], which requires additional sensing equipment which would also increase fabrication and electronics cost. Diode-based actuation provides an alternative to potentially solve the above mentioned problems. This work will use the newly developed method to create an open loop control system which could position the droplet without feedback. The precision and the repeatability will be measured experimentally.

In addition, previous EWOD uses individual electrodes to move droplets. The maximum step size was limited by the electrode size. When large travel distance is required (i.e. 100x the droplets diameter), individual addressable electrodes would need a large number of interconnects. Diode-based actuation simplifies the wiring requirements for long-range travel. But, the reliability and repeatability for the newly developed actuation method was not investigated previously. This work will try to quantify, and possibly improve the current technology by demonstrating reliable working devices.

The proposed mechanical actuator could also benefit research areas other than the EWOD community. Using a capillary bridge to perform mechanical actuation such as grasp and release, as well as alignment, have been an active area of research. However, prior work concentrated on the adhesion force created by capillary bridges [1, 18, 22, 86, 92, 93]. This work will complement prior research by using numerical simulations to investigate the compression force exerted by a capillary bridge. When using droplets to support solid objects, the liquid-ambient interface acts as a spring in the vertical direction. Parameters such as the maximum load, fluid volume, gap height and surface tension are tightly coupled. This work will define these parameters in terms of load capability and stiffness, analogous to a linear bearing, which could then be used to design droplet-based actuators.

## **2.7 Conclusion**

This chapter reviewed various droplet actuation methods, their working principles and performance characteristics. Comparing these methods, electrowetting actuation was shown to be the most favorable candidate in droplet-based actuators. Electrowetting is highly reversible, repeatable, and provides relatively large force in the micro to mesoscale. This work will address some of the challenges in designing and implementing electrowetting-based droplet actuation. But first, the electrowetting force will need to be validated. The following chapter will focus on the experimental approach which measures the electrowetting actuation force.



## CHAPTER 3: ELECTROWETTING ACTUATION FORCE<sup>1</sup>

The main goal of this dissertation is to quantify key parameters which can be used to design droplet-based electrowetting actuators. The previous section reviewed the basic electrowetting principle and common configurations for actuation. Their equivalent circuit representations were discussed. Electrowetting-driven droplet actuators and their accompanying performance are listed.

Due to the high actuation force and simplistic design, grounded configuration in electrowetting was proposed to be used as the actuating configuration.

In this section, the force of a grounded electrowetting droplet is experimentally validated by measuring the actuation force and relating it to the driving voltage. The results are compared to the Young-Lippmann equation. This study shows higher surface tension fluids should be used in droplet-based actuators due to the high actuation force and speed. It also shows when the droplet is used to support solid object (constrained shape), the velocity increases with higher surface tension fluids due to the limiting contact line friction force.

### 3.1 Abstract

Electrowetting on dielectric is a phenomenon in which the shape and apparent contact angle of a droplet changes when an electric field is applied across the droplet interface. If the field is asymmetric with respect to the droplet, then a net force can be applied to the droplet. In

---

<sup>1</sup> This chapter was published in *Microfluidics and Nanofluidics* (Ni, Q., Capecchi, D.E., and Crane, N.B., *Electrowetting force and velocity dependence on fluid surface energy*. *Microfluidics and Nanofluidics*, 2015. **19**(1): p. 181-189). Permission is included in Appendix A

this work, we have measured the electrowetting force by confining the droplet shape beneath a glass plate and measuring the force on the plate. The force was measured as a function of voltage for a range of fluids with different surface energy. Measured forces show excellent agreement with predictions based on the Young-Lippmann equation using measured contact angles. Results also show that the electrowetting force is independent of fluid surface energy below saturation, but that the peak force is proportional to the surface tension. This work shows that lowering the surface energy of the fluid can induce larger contact angle change under the same voltage, but it has no beneficial impact on the actuation force in droplet-based actuators. In contrast, velocity tests with deformable droplets show higher speeds for lower surface energy fluids, even above their saturation voltage. However, when the droplet's shape is restrained, the highest velocity is achieved with high surface energy fluids due to the larger electrowetting actuation forces that are applied.

### **3.2 Introduction**

Electrowetting on dielectric (EWOD) uses an external electric field to change the apparent contact angle of a droplet on a dielectric layer. For a grounded droplet configuration, a conductive liquid and a metal substrate are separated by a thin dielectric. Voltage potential is applied between the droplet and the substrate. The contact angle of the droplet follows the Young-Lippmann equation until a certain point which is referred to as the contact angle saturation [23]. EWOD is frequently employed in optical [95], display [96], and lab-on-chip technologies [97] where fluid position and shape are the primary metrics. It also shows promise in mechanical applications including pumps [82], grippers [84], switches and motors [98, 99].

For display and bio-sampling applications, motion velocity is a key metric, as it improves video quality and through-put, respectively. On the other hand, the maximum force the EWOD

droplet can achieve is the primary interest in designing actuators, pumps, and grippers. However, only limited direct measurements of mesoscale electrowetting forces have been reported previously. Common experimental approaches use either capillary rise experiments which calculate the electrowetting force from induced hydrostatic pressure difference [100], or by relating the electrowetting force to the contact angle based on the Laplace pressure across the droplet/ambient interface [101]. Other techniques such as measuring the pressure change inside of a microfluidic channel [62], measuring the capacitance of the droplet [102], or using an attached AFM tip [103] have also been explored. Mannerje et al. [104] has measured the force due to localized EW under applied AC signal, but these measurements are limited by the strength of the wetting to the small rod used to move the droplet. Due to the complex geometry and the dynamics of the contact line, direct force data is scarce.

This paper addresses the gap of experimental investigations in electrowetting forces and their dependence on the fluid properties. In this work, we address how the EW force varies with the applied electrical potential and the surface energy/surface tension ( $\gamma$ ) of the droplet/ambient interface. First, the force relationships for the electrowetting of a droplet with respect to the contact line length are developed. Experimental methods for directly measuring the electrowetting force are described and the results are compared to the conventional contact angle approximation. Velocity of droplets composed of high and low surface energy fluids are compared between a free deformable drop and a constrained drop. Design considerations for EWOD actuators are discussed and the relationship of these measurements to prior velocity testing results are discussed.

### 3.3 Electrowetting Force

For an arbitrary shaped droplet during EWOD actuation, the change in contact angle is induced by the electric field between the fluid/dielectric interface. The force acting near the interface per unit length of contact line can be expressed as:

$$\bar{F} = \frac{\epsilon_0 * \epsilon}{2 * \delta} * \bar{V}^2 \quad \text{Equation 3-1}$$

where  $\epsilon_0$  is the permittivity of free space,  $\epsilon$  is the dielectric constant of the insulating layer, and  $\delta$  is the dielectric thickness [105]. The electrowetting force can be calculated by integrating around the droplet contact line that covers the active electrode (see Figure 3-1):

$$\bar{F} = \frac{\epsilon_0 * \epsilon}{2 * \delta} * \bar{V}^2 \quad \text{Equation 3-2}$$

where ( $\bar{F}$ ) is the force vector and  $\hat{n}$  is the unit normal to the direction of the force.

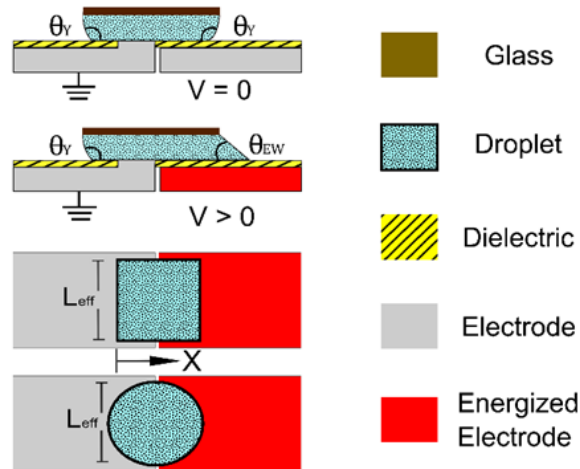


Figure 3-1: A square droplet is created by placing a square glass plate over it. The droplet assumes the shape of the glass plate. One side of the droplet is grounded. When a voltage is applied to the other electrode, the contact line moves only slightly but a force is still applied to the glass plate.

We will consider the case of a droplet wetted to a glass plate that is placed on a hydrophobic ( $CA > 90^\circ$ ) substrate. For small droplet volumes, the droplet is well-approximated by a prism with the cross section of the glass plate [89]. For the simple cases of a rectangular plate or a circular plate that is halfway over the energized electrode (Figure 3-1), the total electrowetting force can be combined with the Young-Lippmann equation and simplified to:

$$F = \frac{\epsilon_0 * \epsilon}{2 * \delta} * V^2 * L_{\text{eff}} = (\text{Cos}(\theta_{\text{EW}}) - \text{Cos}(\theta_Y)) * \gamma * L_{\text{eff}} \quad \text{Equation 3-3}$$

where  $\theta_{\text{EW}}$  is the apparent contact angle under voltage,  $\theta_Y$  is the equilibrium contact angle when  $V = 0$ ,  $\gamma$  is the droplet/ambient interfacial tension,  $L_{\text{eff}}$  is the length of the droplet normal to the force direction at the boundary between the two electrodes. Alternatively, the force can be found by calculating the derivative of the system energy with respect to a displacement in the direction of the force. For the case of a square droplet, the change in  $L_{\text{eff}}$  with voltage and position is negligible so that the energy change in the system is the electrical energy stored in the capacitor formed between the droplet and the electrode [89]. The capacitive energy stored below a square droplet is (see Figure 3-1):

$$E = \frac{1}{2} * C * V^2 = \frac{1}{2} * \left( \frac{\epsilon_0 * \epsilon * X * L_{\text{eff}}}{\delta} \right) * V^2 \quad \text{Equation 3-4}$$

where  $(x*L)$  is the area of the droplet that's covering the working electrode. Taking:

$$F = \frac{dE}{dx} = \frac{1}{2} \left( \frac{\epsilon_0 * \epsilon}{\delta} \right) * V^2 * L_{\text{eff}} \quad \text{Equation 3-5}$$

Equation 3-3 is recovered. It is important to note that according to Equation 3-5, the force is independent of the interfacial tension of the fluids used. So below contact angle saturation, the force should only be a function of the voltage applied.

### 3.4 Experimental Setup

#### 3.4.1 Electrowetting Force Measurement

The experimental configuration is illustrated in Figure 2. A force sensor (NanoScience Instruments FT-270, resolution  $2 \mu\text{N}$ ) was bound to a thin glass fiber (diameter  $\sim 5 \mu\text{m}$ ) using cyanoacrylate. On the other end of the fiber, a glass plate (13.5 x 4.5 x 0.1 mm) was attached using the same method. The glass plate was patterned with  $1 \mu\text{m}$  Cytosol<sup>®</sup> to define two hydrophilic regions separated by a hydrophobic region. One droplet is placed in each hydrophilic region. Due to the uneven pressure distribution inside the droplet under electrowetting actuation, the glass plate tends to tilt when a voltage is applied. Therefore, only the droplet away from the force sensor was actuated during force measurements, and the droplet which was closer to the sensor provided a counter moment to the plate to prevent rotation. As a result, the lateral force of electrowetting was translated through the droplet to the top glass plate and measured by the force sensor with negligible plate tilting.

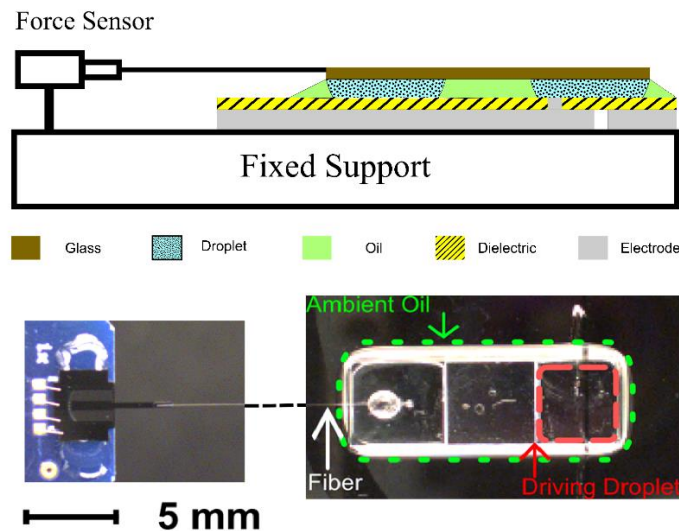


Figure 3-2: Force measurement setup. The illustration on top is the measurement system viewed from the side. The lower left is a magnified view of the force sensor from the top. The lower right is the top view of the glass plate with droplets and oil under the plate.

The substrate was fabricated by evaporating aluminum (400 nm) onto clean glass slides using electron-beam deposition. The aluminum was patterned to form two electrodes using photolithography. A 2  $\mu\text{m}$  ( $\pm 0.15 \mu\text{m}$ , measured by an Alpha-step profilometer) Parylene C coating was deposited using a Parylene lab coater (Specialty Coating System, PSD2010). Finally, a 30 nm Cytop® top coat was applied to render the substrate hydrophobic. Our group and others have reported that anodic electrowetting with weak acid and aluminum improves electrowetting reliability [37, 75]. Therefore, the electrolyte base was chosen to be 0.1 M Citric Acid. Non-ionic, water soluble surfactant (Tergitol™ NP-8, CMC 61 ppm, DOW chemical company) was added with 0.001% and 0.005% by weight concentration. The ambient phase used was silicone oil (OS-30, Dow Corning) or n-hexadecane (99% pure, Alfa Aesar).

The experimental procedures are listed as follows: (i) Before each test run, a scratch was made in the Parylene covering the grounding electrode to provide electrical ground to the droplet. (ii) The fluid of interest (a total of two droplets with volume of 10  $\mu\text{L}$  each) was deposited on the two wetting regions of the top plate manually using a pipette. (iii) The glass plate was lowered onto the substrate to allow the droplets to touch the surface. (iv) Ambient fluid (10  $\mu\text{L}$ ) was pipetted in the gap between the glass plate and substrate. (v) A DC voltage ramp was applied at 1 V/0.2 second and the reading from the force sensor was collected as well as the applied potential (see Figure 3-3). A total of five tests were performed, and each test was done on a new location of the substrate. The total volume of the fluid used was fixed to be 30  $\mu\text{L}$  during all experiments, and the gap height was maintained by the surface tension of the oil/air interface. Therefore, no significant height change was observed with different surfactant concentration.

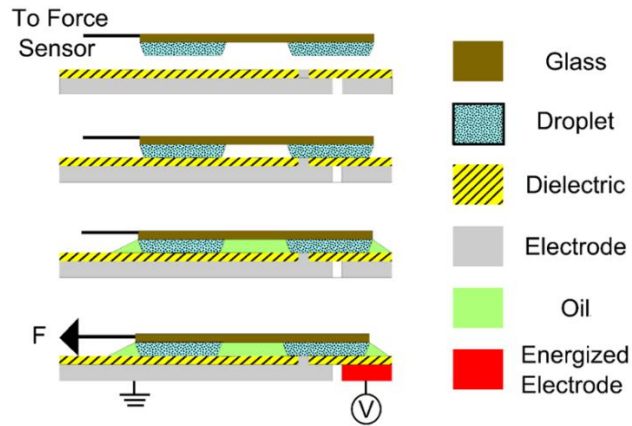


Figure 3-3: Experimental procedure. Droplets of testing fluids were deposited first onto the top plate. Then, the plate was lowered to touch the electrowetting substrate. Ambient fluid was then added. When a voltage was applied, the force on the plate was measured and recorded.

### 3.4.2 Contact Angle Measurements

Contact angle measurement was done on a goniometer fitted with a digital camera and the images were processed using ImageJ software. Contact angle was measured with the same voltage ramp as the force measurements. For solutions with surfactant, the voltage ramp was stopped at 80 Volts. For all other measurements, the voltage was ramped to 120 Volts. Again, a total of five tests were performed for each solution.

## 3.5 Results and Discussion

### 3.5.1 Direct Force Measurements

The measured actuation force is plotted vs. the applied voltage. As the figure shows, regardless of the concentration of the surfactant, the measured force followed the same slope until saturation. The peak force each fluid achieved was proportional to the interfacial surface energy (see Figure 3-4).



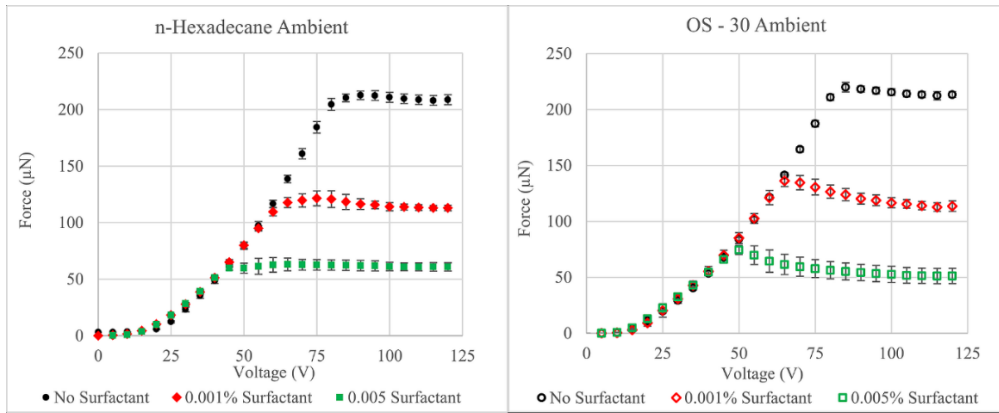


Figure 3-4: Measured electrowetting force vs. the applied voltage. The plot on the left shows the tests performed using n-Hexadecane as the ambient fluid, and the plot on the right using OS-30 silicone oil. No surfactant: 0.1 M citric acid. 0.001% surfactant and 0.005% surfactant: the percentage concentration by weight added to the base solution. The average values of five tests for each material combination are presented with the error bars showing the standard deviation of the results.

### 3.5.2 Contact Angle Measurements

The measured contact angle is plotted vs. voltage applied (see Figure 3-5). All combinations of droplet/fluid and ambient/fluid show contact angle variation from  $\sim 170^\circ$  to  $\sim 60^\circ$ . Surface tension (mN/m) was extracted from the contact angle measurements using methods described by Banpurkar et al. [106] and the values are tabulated in Table 3-1.

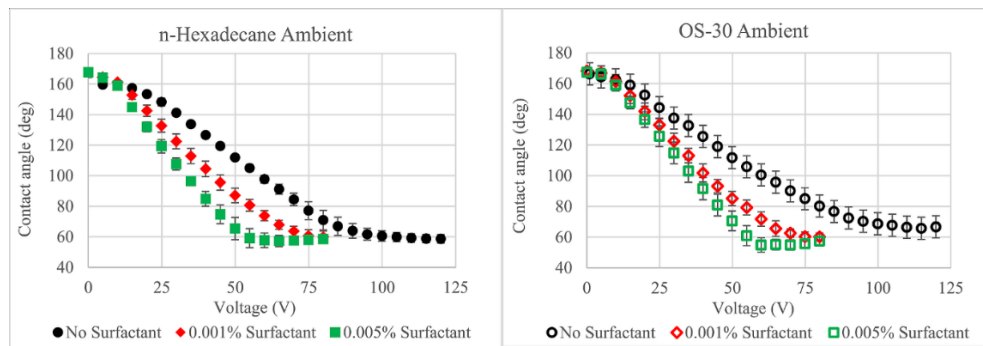


Figure 3-5: Measured contact angle vs. voltage applied. The figure on the left shows tests performed in n-hexadecane ambient and the figure on the right shows tests performed in OS-ambient. No surfactant: 0.1 M citric acid. 0.001% surfactant and 0.005% surfactant: the percentage concentration by weight added to the base solution. The average of five tests is presented. Error bars show the standard deviation of the results.

Table 3-1: Surface tension values (mN/m) extracted from contact angle measurements. The rows are the actuation fluids, and the columns are the ambient oil. Five repetitions were performed for each test, and the average value and their standard deviation are listed.

	n - Hexadecane ambient	OS – 30 ambient
0.1 M Citric Acid	30.9 ± 2.3	36.0 ± 3.6
0.001% by weight Tergitol added	17.2 ± 1.2	18.9 ± 1.1
0.005% by weight Tergitol added	10.7 ± 0.7	12.5 ± 1.1

### 3.5.3 Comparison between Measured Force and Calculated Force from Contact Angle

In order to relate the measured force to the contact angle, the extracted interfacial tension and the average values of the measured contact angle, along with the plate width ( $L_{\text{eff}} = 4.5 \text{ mm}$ ), were used to calculate the electrowetting force using Equation 3-3. These results are compared to the measured electrowetting force in Figure 3-6.

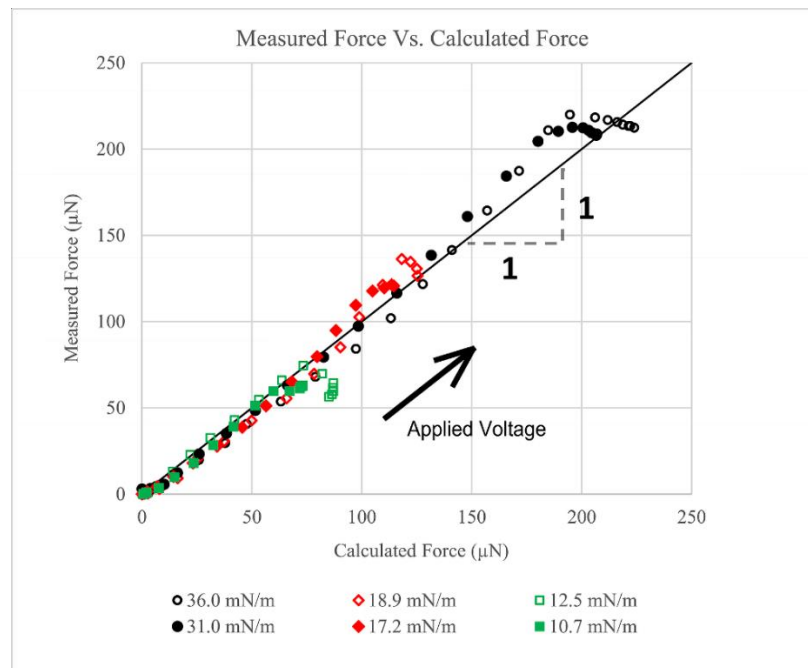


Figure 3-6: The average of the measured electrowetting force is plotted against the average calculated force from the contact angle. The relative surface tension values are used instead of the surfactant concentration. The straight line with the slope of 1 provides a comparison standard for those two methods used.

The measured electrowetting force agrees very well with the calculated force below the saturation voltage. The measured force for most fluids exceeded predictions as the voltage approached the saturation voltage, before dropping below the prediction as the contact angle saturation voltage is exceeded. Although the cause of contact angle saturation is still under intense debate [107, 108], it is possible that in this case, geometry changes of the droplet could cause this increase due to a small increase in  $L_{eff}$  prior to saturation.

The fact that the measured force dropped below the predicted force after contact angle saturation was somewhat difficult to interpret. It was suggested by Jones [87] that the electrowetting force can still increase even after contact angle saturation. Jones also stated that there was no direct evidence to assume the contact angle saturation was limiting the electrowetting force. However, our measurements show only a small excess of force near the contact angle saturation point, after which the force drops below predictions. Thus, the contact angle saturation is a good prediction of the force saturation limits in these geometries. It is possible that these effects are due to size and geometric effects such as droplet spreading on the electrode and/or dewetting from the plate above the saturation voltage. Further work is necessary to address this force limit.

To consider the data differently, forces measured after the onset of saturation were first normalized by the effective length ( $L=4.5$  mm), then plotted against the electrowetting number

( $\eta = \frac{1}{2} \left( \frac{\epsilon_0 * \epsilon}{\gamma * \delta} \right) * V^2$ ) to show the dependence of the force with surface tension of the fluids.

Then, the same normalized forces were plotted against the products of surface tension and the electrowetting number ( $\gamma * \eta = \frac{1}{2} \left( \frac{\epsilon_0 * \epsilon}{\delta} \right) * V^2$ ) to show the voltage dependence of the electrowetting force (shown in Figure 3-7). The figure highlights the design considerations for EWOD-based devices.

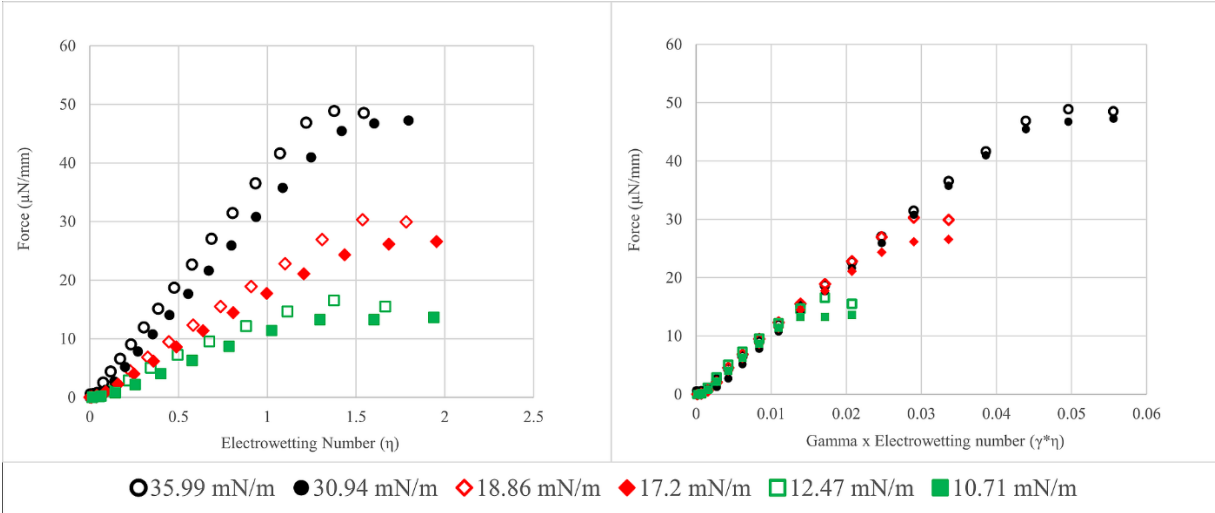


Figure 3-7: Measured unit force before saturation plotted against (a) electrowetting number ( $\eta$ ), left graph, (b) surface tension times electrowetting number ( $\gamma^*\eta$ ), right graph. Interfacial tension values are listed instead of material combination.

At the same electrowetting number, higher surface tension fluids provide higher actuation force (Figure 3-7a). While low energy fluids require less voltage to reach saturation, the actuation force is much larger with high surface energy fluids. Additionally, the electrowetting forces produced by all tested fluids follow the same linear relationship between force and  $V^2$  regardless of the interfacial tension of the fluid, as predicted (Figure 3-7b). So the actuation force is only dependent on the voltage applied prior to saturation. Interestingly, the electrowetting force/length exceeded the interfacial energy of the fluid for all tested fluids; many by 50%. Even with the uncertainty of the contact line length during the force experiments, the applied force/length has clearly exceeded the interfacial energy of the fluids. Thus, it is likely that the force was limited by either the stability of the droplet/substrate interface, or by the wetting force of the droplet acting on the top glass plate. By decreasing the volume of the droplets and/or enhancing wetting to the top glass plate by adding roughness features to the plate, the electrowetting force might be increased further.

In summary, for electrowetting-based actuators, if lower voltage requirements are the primary design consideration, lower surface tension fluids should be used. If the maximum actuation force is the goal of the device, then higher surface tension fluids should be utilized.

### **3.6 Considerations for Electrowetting Velocity**

As discussed above, actuation velocity is important to many electrowetting applications; even where the force is the primary metric of concern, actuation velocity determines the response speed and actuator bandwidth. If the droplet were a rigid body, higher forces would be expected to produce higher accelerations and higher peak velocity. However, Lu et al. [109] has reported that the center of mass of the EWOD droplet reached higher velocity with a higher electrowetting number, which is contrary to this force-based prediction.

To investigate the impact of electrowetting force on actuation speed, two additional sets of experiments were performed in order to compare velocities of different surface energy fluids in the traditional closed electrowetting configuration with a grounded top plate, to the fixed-shape droplet case studied here. Patterned substrates were fabricated using the same method described in an earlier section. The size of the electrodes were 4 x 4.5 mm. For the first set of experiments, a cover plate coated with indium-tin oxide (ITO) was used to provide electrical ground to the droplet. The ITO-covered glass slides were also coated with 30 nm Cytop® to ensure the same hydrophobic surface property. The gap between the top plate and the substrate (400  $\mu\text{m}$ ) was maintained by a plastic shim. The volume of the droplet was 10  $\mu\text{L}$  and the ambient fluid used was OS-30 oil. An initial voltage was applied to the electrode on the left at time  $< 0$  to maintain the position of the droplet at the beginning. Then, the voltage was switched to the electrode on the right at time  $> 0$ . A digital camera above was triggered at 50 Hz to capture the evolution of the droplet as it moved towards the active electrode.

### 3.6.1 Free Deforming Droplet

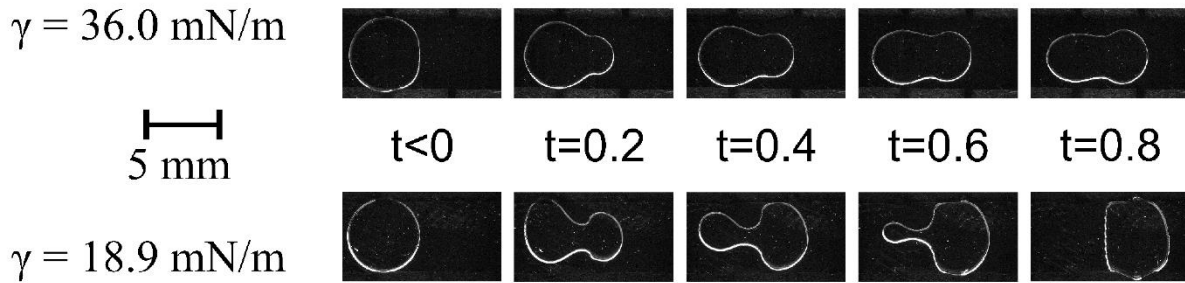


Figure 3-8: Comparing the motion of free deforming droplets sandwiched between two plates during electrowetting actuation. The top row is high surface tension fluid ( $\gamma = 36.0 \text{ mN/m}$ ), and the bottom row is low surface tension fluid ( $\gamma = 18.9 \text{ mN/m}$ ). The time at which the image was taken is listed in seconds. The low surface tension fluid deformed much more during actuation and conformed to the electrode shape much easier. The scale bar is 5 mm. Applied voltage: 70 V, ambient fluid: OS-30. Droplet was grounded through a ITO-covered top plate.

In our experiments, lower surface tension droplets reached the active electrode much faster than high surface tension droplets under the same applied voltage. This is true even when the applied voltage is well above the saturation voltage of the low energy fluid. The images show that the low surface tension droplets were able to stretch more than the higher surface tension droplets at the same applied voltage (Figure 3-8). The characterization of the droplet deformation is beyond the scope of this paper, but contact line friction, viscosity, and contact angle hysteresis all contribute to this behavior [110-113]. Of all these factors, the dynamic contact angle hysteresis and the viscosity of both the ambient fluid and the droplet are thought to be most relevant to the deformation of the droplets (see later section about dynamic contact angles and contact line friction). Under electrowetting actuation, the leading contact angle deforms under the applied potential, and the contact line starts to move. But, the contact line at the top leading edge and both trailing edges (top and bottom) was pinned due to contact angle hysteresis. The induced internal flow, and the shear stress developed due to the viscosity contrast of the ambient and droplet caused the droplet to deform. The deformation on the leading edge of the droplet

increases the effective contact line length on the active electrode, which increases the force. Simultaneously, the low energy surface more readily deforms in response to the resistance of the ambient fluid to reduce the drag force on the droplet. Both effects would act to increase the droplet actuation velocity. The first effect would increase the force on the low energy droplet, while the second would reduce the drag. Additionally, the contact line hysteresis, or contact line friction is often proportional to the surface energy. So, the larger actuation force/contact line length may be partially offset by these contact line losses. These observations are consistent with the results of others [109], but additional studies are needed to provide a complete understanding. Given that lowering the surface tension can lower the operational voltage in the EWOD device, low surface tension fluids are favorable for free droplets.

If the higher speed of low surface energy droplets is related to their ability to change shape readily, this advantage should decrease or be reversed in the case of fixed-shape droplets. As fixed geometries are able to exert the largest forces, this condition is important for maximizing actuation speed. In this case, high surface tension fluid would be expected to provide both high peak force and higher velocity. As a validation, velocity of fixed-shape droplets of different fluid types were measured in the second set of experiments.

### **3.6.2 Fixed-shape Droplet**

The same electrode design was used, but the top cover plate was replaced with a free circular glass plate (diameter: 8 mm, thickness: 100  $\mu\text{m}$ ) that was wetted by the EWOD droplet. A scratch in the Parylene on one electrode was used to provide electrical ground. The oversized plate forced the droplet to wet the top plate and remain circular during motion. Also, the effective length of the droplet was constrained due to the fact that the plate diameter (8 mm) was much larger than the electrode width (4.5 mm). The experiments were performed in air with just

2  $\mu\text{L}$  silicon oil (OS-30) at the interface to minimize contact line friction. Although the experiments were done in air, the oil shell encapsulated the droplet/substrate interface, so the electrowetting force should still depend on the droplet/oil surface tension values. The combined volume of the droplet and ambient oil resulted in a gap height of 400  $\mu\text{m}$ . Potential was applied to one of the electrodes and the movement of the droplet was captured at 50 frames/second. Afterwards, the images were analyzed using a MATLAB routine to track the position of the circular plate, and the centroid of the plate was extracted for each frame. The displacement of the glass plate is plotted against the time in Figure 3-9.

At low voltage (50 V), the droplet displacement was similar for both high and low surface tension fluids. The low surface tension fluid moved slightly faster than the high surface tension fluid. It is possible that the same volume droplet would have a slightly larger contact area with lower surface tension. At high voltage (70 V), the velocity increased for both fluids. However, the constraining top plate limits the spreading, and the higher surface energy fluid achieved much faster motion, as expected from the EW force measurements. Thus, high surface energy fluids are preferred for electrowetting actuations when high velocity of a constrained droplet is needed, or large actuation forces are desired.



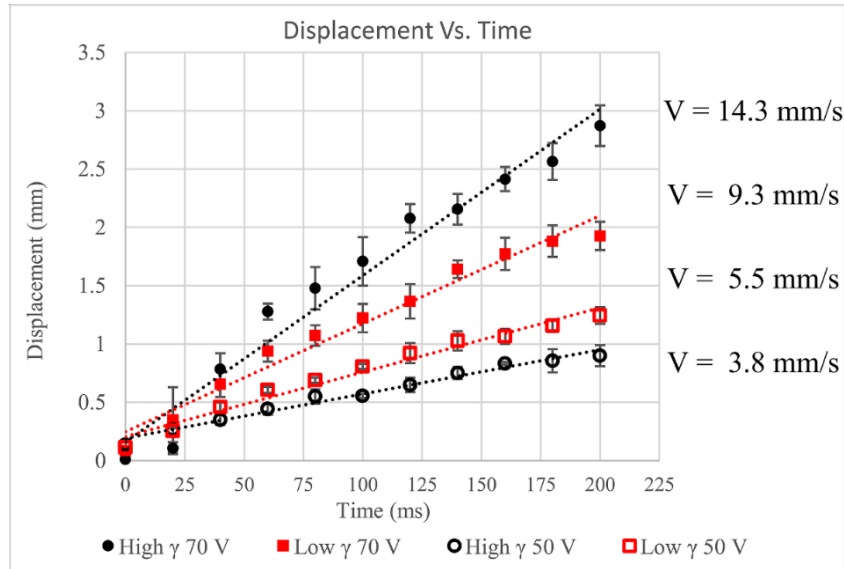


Figure 3-9: Plate speed under electrowetting actuation. A circular plate was carried by the EWOD droplet. The relative displacement of the plate (mm) is plotted against the time (ms) after the voltage was applied. The high surface tension fluid was 0.1 M citric acid (36.0 mN/m) and the low surface tension fluid (18.9 mN/m) was 0.001% surfactant by weight. The maximum voltage (70 V) was below both fluids' saturation voltage. The average velocity of the plate is listed on the right. The average value of 3 tests are presented, and the error bars are the standard deviation of the data

### 3.6.3 Friction Effect

As discussed earlier, the forces opposing motion is a result of the combined effect of viscosity of the fluid, the surface tension, and the contact angle variation during motion (dynamic contact angle). A large amount of detailed studies have been conducted for droplets with a moving contact line for both droplet spreading [113-115] and electrowetting-forced wetting [112, 116, 117]. The frictional force is usually thought to be proportional to the capillary number  $Ca$  ( $Ca = \frac{\mu * U}{\gamma}$ ), where  $\mu$  is the viscosity, and  $U$  is the contact line speed.

For a fixed-shape droplet (in our case, a thin circular cylindrical-shaped droplet), the friction variation can be measured by simply dragging the droplet at a fixed speed. Refer back to Figure 3-2.; the same force measurement setup was used to drag the same fixed-shape droplet

across the same hydrophobic substrate. A linear stage (UTS100CC, Newport Corp.) was used to move the substrate at a given velocity, and the sensor was fixed to the support. The tests were performed for low and high surface tension fluids at 2.5, 5, 7.5 and 15 mm/s. The initial inertial effect was discarded and only the forces at steady-state velocities were reported. The measured forces were normalized by the plate diameter (8 mm) and then plotted against the velocity for each combination (Figure 3-10), and the insert shows the normalized force vs. the capillary number  $Ca$  (using  $1 \text{ mPa}\cdot\text{S}$  for  $\mu$ ).

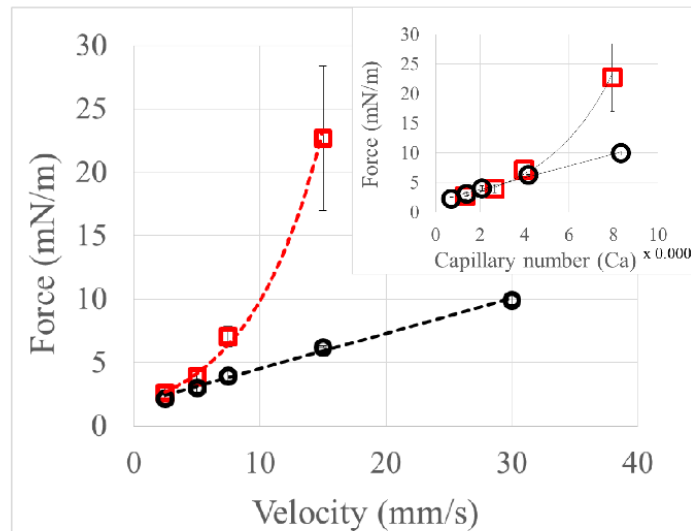


Figure 3-10: Normalized friction force vs. velocity. The velocity for the tests were 2.5, 5, 7.5 and 15 mm/s for all fluids with the additional 30 mm/s for the high surface tension fluid only. The squares are the low surface tension fluids ( $\gamma = 18.9 \text{ mN/m}$ ) and the circles are the high surface tension fluid ( $\gamma = 36.0 \text{ mN/m}$ ). Each data point represents the average of three runs and the standard deviation is presented. The insert is the same force plotted against the capillary number ( $Ca$ ).

During the experiments, a dynamic force oscillation was observed around  $Ca \sim 4 \times 10^{-4}$ , but the force variation was low ( $\sim 0.5 \text{ mN/m}$ ). Plate tilting due to viscous shear was only observed for low surface tension fluids at  $Ca \sim 8 \times 10^{-4}$  (the last data point of low  $\gamma$ ). Also, both

the drag force and the dynamic force oscillations started to increase after the average speed became stable for that particular case. The friction force for high surface tension fluid increased linearly with the capillary number. However, the friction force for low surface tension fluid had much larger gain when the capillary number increased to  $Ca \sim 8 \times 10^{-4}$ . In the dynamic contact angle study conducted by Nelson et al. [112], the dependency of contact line friction in terms of dynamic contact angle hysteresis without electrowetting was fairly weak at  $Ca < 5 \times 10^{-4}$  and the contact angle hysteresis increased after  $Ca > 1 \times 10^{-3}$  for water in air. Our experiments observed the same trend for low surface tension fluids where a large force increase was seen after  $Ca > 5 \times 10^{-4}$ . It is unclear why higher surface tension fluids did not follow the same trend. It is possible that in our experiments, the top plate was carried by the droplet, and the weight of the glass plate contributed to the effect. It is also possible that surface tension changes the slope; since the plate is not rigidly constrained, it could undergo some tilting that might impact the measured forces. However, the plate appeared to remain parallel to the substrate during testing.

Without provoking the hydrodynamic or molecular kinetic theory presented in earlier references [113-115], the data still provides some insight to the interpolation to earlier speed experiments. First, the friction force at a given measured velocity (Figure 3-9) was extracted using a fitted line from Figure 3-10. Assuming the measured friction forces represent the total force opposing the motion during electrowetting actuation, Table 3-2 summarizes the forces and their differences under actuation. The highly non-linear nature of the residual force (the difference between the applied force and the friction force) seems to indicate that there are other additional dissipation mechanisms which are related to both the surface tension and the velocity. Perhaps, like it was pointed out [112], the stick-slip behavior at high electrowetting number actuation has additional impact in the friction force and the electrowetting changes the localized

flow condition around the contact line. Or, it could be the assumption of measured friction force at steady state did not match the transient behavior of electrowetting actuation. More advanced analyzing methods are needed for future studies.

Table 3-2: Measured electrowetting force and the friction force during actuation. All numbers are normalized by their respective length (mN/m)

Surface tension and measured velocity	Electrowetting force	Friction force	Residual force
36.0 mN/m at 14.3 mm/s	36.5	5.7	30.8
36.0 mN/m at 3.8 mm/s	18.7	2.8	15.9
18.9 mN/m at 9.3 mm/s	30.0	8.7	21.2
18.9 mN/m at 5.5 mm/s	19.0	4.5	14.4

At low speed, both the low and high surface tension fluid were under the same actuation force. The contact line friction was slightly higher for the low surface tension droplet. However, the low surface tension droplet moved faster as seen in Figure 3-8.

When the contact line speed increased beyond  $Ca \sim 3 \times 10^{-4}$ , the friction force increased as the speed of the contact line increased. The low surface tension droplet experienced much more friction force than the high surface tension droplet. The additional friction force limits the speed of the low surface tension droplet at high voltage (70 V). For high surface tension fluid, the linear relationship with speed follows a less-step slope. So the high surface tension droplet can travel faster at high voltage. Since high surface tension fluids can reach higher velocity at a given capillary number; they should be used for fixed-shape droplet actuation to maximize both the force and speed.

### 3.7 Conclusion

We have measured the electrowetting force by confining the geometry of a droplet. Below contact angle saturation, the measured force agrees well with the force predicted from contact angle measurements. The measured electrowetting force exceeds the predicted saturation point but declines with increased voltage beyond saturation. Higher surface energy fluids achieve much larger forces than low surface energy fluids. However, droplet velocity is not directly related to the electrowetting force. Free droplet velocity is higher for lower surface energy fluids as compared to higher surface energy fluids. It appears that droplet deformation has a large impact on droplet transportation speed in EWOD of free droplets. The electrowetting number should be used to design EWOD devices for moving droplets as previously reported. However, for a droplet with fixed-shape, the maximum velocity increases with higher surface tension fluids due to the limiting contact line friction force. So as a rule, for a higher force/speed of an EWOD actuator, higher surface tension fluids should be used.

## CHAPTER 4: DROPLET MICRO-STEPPING USING ELECTROWETTING

The goal of this dissertation is to establish the design criteria for a droplet-based mechanical actuator. The previous chapter validated the static actuation force in electrowetting actuation. Design parameters such as surface tension and applied voltage were analyzed. A successful actuator driven by electrowetting requires not only high actuation force but also precise positioning. Conventional electrowetting droplets require complicated fabrication and control schemes to achieve high precision. When designing such actuators, tradeoffs between the speed and precision must be made. This chapter presents a novel electrowetting configuration which uses diodes and simplified open-loop control. By implementing this in a mechanical actuator, challenges in wiring and control could be eliminated.

### 4.1 Abstract

Microfluidic-based mechanical actuation opens new possibilities for positioning and manipulating small, delicate components. However, existing methods are not well-suited to positioning with high resolution. This paper reports a method for precise, open-loop control of droplet position in finite steps by varying the input signal's duty cycle in electrowetting actuation. When wetted to a solid object, both the droplet and the solid can be actuated. Unlike conventional electrowetting actuation methods, positioning resolution in our proposed method can be much smaller than the size of the underlying electrodes without requiring a closed-loop feedback control system. Using a leaky dielectric coating, the electrode/electrolyte combination in our device acts as a simple diode by blocking current in one direction and conducting in the

other. The position of the droplet can be controlled without feedback by varying the duty cycle of the applied AC square wave; each duty cycle corresponds to a unique position on the electrode. The driving mechanism is investigated using a simplified circuit simulation and the position/duty cycle relationship is found to be nonlinear, but symmetric about the center of the electrodes. This approach provides a method for improving open-loop positioning resolution without adding more electrodes. Positioning is within 0.2 mm ( $< 2.5\%$  of the droplet diameter) of the idealized model and repeatability is  $< 0.07$  mm ( $< 0.8\%$  of the droplet diameter).

## 4.2 Introduction

Many techniques are available for microscale actuation including electrostatics, piezoelectrics, thermal expansion, and magnetics [9, 10]. However, these methods are typically characterized by high stiffness and low displacement. Additionally, the actuators are typically many times larger in size compared to the range of motion that they provide. While the high stiffness of piezoelectric and thermal actuators allows them to generate large forces with high precision, this can make it difficult to handle delicate components without damage. Fluidic actuation provides a potential alternative method, with inherent compliance that will protect delicate components [13, 92]. Fluidic actuation could be accomplished by viscous forces due to flows in a bulk liquid [118], but surface tension-based manipulation has proven especially effective in microscale bonding for self-assembly and other applications [1, 14]. Electrowetting is a leading way of manipulating fluids with surface effects.

Electrowetting is a phenomenon in which a fluid interface is deformed by an electric field between an electrode and the fluid. It is commonly implemented with a dielectric covering the electrode in order to reduce reactions. This is termed electrowetting on dielectric (EWOD).

While most applications focus on the movement of droplets or liquid interfaces, droplets have

also been used to perform out of plane mechanical actuation as an alternative to electrostatic actuation [119]. In-plane motion (both linear and rotational) has also been demonstrated. Continuous motion similar to electromechanical motors was demonstrated by Lee and Kim [78] using a method they termed “Continuous electrowetting effect”. Nelson *et. al.* demonstrated the use of embedded diodes to transport a droplet in a continuous linear motion with a constant input voltage [76]. The majority of EWOD actuation has been done in an open-loop stepped system, analogous to a stepper motor. Each electrode acts as the pole piece when the neighboring electrodes are energized in a specific order. Researchers have demonstrated a micro conveyor system - in which electrowetting droplets move a solid reaction platform [64] - as well as a rotational capillary motor driven by EWOD [27].

EWOD-based capillary actuators are much more compact than conventional microactuators - requiring only the droplet and a substrate to support it. There is no need for external machinery other than a voltage input. Since capillary forces dominate gravitational forces below the millimeter scale, the actuation parameters such as maximum travel and force can be tailored to a specific application, and cover a variety of length scales. Most importantly, due to the inherent compliance introduced by the fluidic interface, the delicate parts of capillary actuators can be handled [22]. In order to maximize the actuation force and speed of EWOD droplets, grounding the droplet is usually favored over a floating configuration [72, 80]. However, if a droplet is used to carry solid objects, the droplet must be grounded from below. This increases the routing challenges compared to a ground-from-above scheme, typically used in pure fluidic actuation [31, 63].

The key limitation in EWOD stepping actuation is that when both large travel distance and precise positioning is required, effective actuation becomes challenging. In stepper actuation,



to move multiple droplet diameters, the electrodes must be smaller than the droplet's contact area on the substrate. Control algorithms must turn on/off a large number of electrodes to control the motion [30, 120, 121]. When large travel distance or two-dimensional motion is required, the number of electrodes can rapidly increase, generating significant wiring and control challenges. While smaller electrodes (and thus smaller droplets) increases position resolution, they reduce the vertical load capacity and horizontal actuation force. This also reduces the actuation speed.

Effective mechanical actuation requires sub-droplet positioning resolution with maximum force and speed. Finer motion has been demonstrated by hybrid methods that implement feedback control to move a droplet as small a distance as 1/5 of the electrode [40]. However, this also imposes additional sensing and software requirements that increase the system cost and complexity, while reducing the benefit from utilizing stepped actuation for large-scale motion. Electrowetting actuation systems would benefit from open-loop positioning capability with sub-electrode resolution analogous to electromechanical stepper motors with micro-stepping, which divides each pole into additional segments and provides higher resolution while reducing control complexity.

Previously, we have reported on a bi-directional electrowetting scheme which induces a polarity dependence [26] in the EW response through the use of a passivating conductive layer (aluminum, titanium), and an adaption that uses only two electrode pads to continuously move a droplet [76]. Using a thin dielectric with inherent defects, the leakage current was able to rapidly form and dissolve a thin oxide on metals such as aluminum and titanium using anodic and cathodic polarizations, respectively. The electrolyte/metal interface is effectively an electrochemical diode [77]. This paper shows how AC signals are applied to a diode-based actuation to generate a series of stable equilibrium points for the droplet on a single electrode

pair. The location of the equilibrium varies with the duty cycle of the input waveform. The duty cycle is then varied to move droplets in steps that are a fraction of an electrode in length.

Although both the continuous pumping and step actuation methods are based on the electrochemical diodes, the droplet response is quite different. In continuous actuation, the droplet was actuated as a linear motor with continued actuation force as long as a voltage was applied [76]. In this paper, asymmetric inputs are provided to create a stepper motor with microstepping. Idealized simulation circuit elements were used to understand the voltage response of the system, and to develop a model that relates the electrical input to the droplet position. Finally, the position of the droplet is measured as a function of the duty cycle of the input to verify the prediction of the idealized model to both quantify the accuracy of the position model, and to assess the potential accuracy/repeatability of the approach.

### 4.3 Background

In typical EWOD-driven droplet-spreading experiments, a conductive sessile droplet and the driving electrode are separated by a dielectric coating. A fine wire is inserted into the droplet to serve as the counter electrode. When a voltage is applied between the two electrodes, the droplet spreads out. Either direct current (DC) or alternating current (AC) can be used to supply the voltage. For a grounded droplet, the relationship between the applied voltage ( $V$ ) and the force per unit contact line ( $f$ ) can be expressed by the Young – Lippmann equation for EWOD [71, 94]:

$$f = [\text{Cos}(\theta_{EW}) - \text{Cos}(\theta_0)] * \gamma = \frac{\epsilon\epsilon_0}{2d} V^2 = \frac{1}{2} cV^2 \quad \text{Equation 4-1}$$

where  $\theta_{EW}$ ,  $\theta_0$  are the contact angles with and without the applied voltage,  $\epsilon$  is the relative permittivity,  $\epsilon_0$  is the vacuum permittivity,  $d$  is the dielectric thickness, and  $\gamma$  is the interfacial

tension between the droplet and the ambient. This can also be expressed simply in terms of the capacitance per unit area ( $c$ ). For a DC power supply,  $V$  is simply the voltage from the power source. For an AC supply, the root mean square (RMS) voltage is used.

AC electrowetting has been shown to reduce contact line friction [91] and enhance contact angle modulation by reducing charge injection [122]. The reliability of EWOD devices can also be improved by anodizing the metal electrode in-situ [37, 77, 122]. Anodizing the metal electrode reduces the system's sensitivity to dielectric defects because oxides form and insulate the underlying electrode. Thus, electrolysis is eliminated with DC driving voltages if a positive bias is applied to the substrate, or an AC voltage input that is offset to eliminate/reduce the negative potential applied to the substrate [122]. While the studies discussed above considered grounding the droplet from a wire, the present case examines a configuration which uses coplanar electrodes that are uniformly coated with a leaky dielectric over a passivating electrode. Electrically, this system is best modeled as two diodes in series similar to our prior continuous EW work [26, 76, 77]. While this prior work considered DC input voltages, this considers the impact of AC inputs. Figure 4-1 shows the system configuration, its equivalent circuit representation, and the resulting voltage across each electrode. When a voltage potential is applied, the majority of the voltage drop occurs across the reverse-biased diode so that the actuation force acts towards the higher potential. One side of the droplet is always reverse biased, which reduces the current and resulting electrolysis.

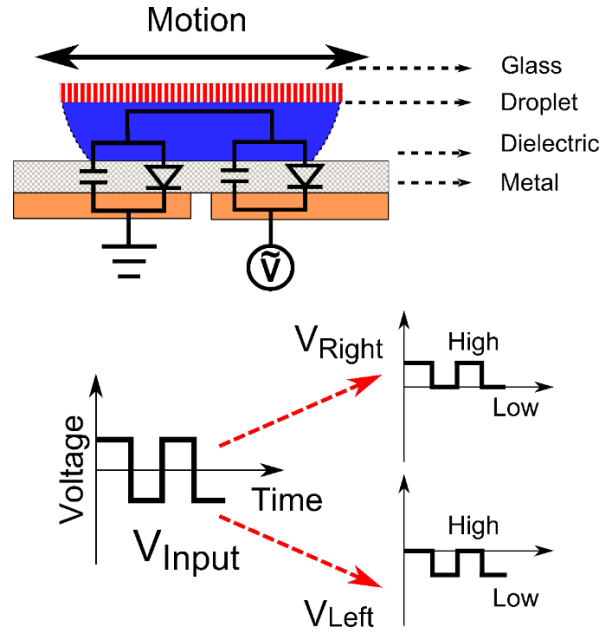


Figure 4-1: Proposed actuation scheme and its equivalent electrical circuit representation. A circular glass plate is carried by the EWOD actuated droplet and an AC square wave input is used ( $V_{Input}$ ). The voltage drop across the dielectric layer on the left and the right side of the droplet is noted as  $V_{Left}$  and  $V_{Right}$ , respectively.

For a symmetric square wave input, the voltage drop across the dielectric might be expected to follow the illustration shown in Figure 4-1. When the excitation voltage is positive, most of the applied voltage drop appears on the right side of the droplet/dielectric interface. When the applied voltage is negative, the voltage drop is mostly concentrated on the left side of the droplet/dielectric interface. The droplet is effectively grounded by one of the electrodes at any given time.

The force acting on the droplet can be expressed using Equation 4-1:

$$f = \frac{\epsilon}{2d} \tilde{V}_{Right}^2 - \frac{\epsilon}{2d} \tilde{V}_{Left}^2 = \frac{c}{2} (\tilde{V}_{Right}^2 - \tilde{V}_{Left}^2) \quad \text{Equation 4-2}$$

In Equation 4-2, the voltages  $\tilde{V}_{Right}^2$  and  $\tilde{V}_{Left}^2$  are the RMS voltages across the dielectric at the right and left side of the droplet; the negative sign indicates the difference of the force direction.

For a square waveform, the RMS voltage can be expressed in terms of its duty cycle input. The duty cycle (D) of a square wave is defined as the ratio of the high pulse time ( $t_1$ ) over the period (T). The time-averaged force over one period is then:

$$f_{net} = \frac{c}{2} * \left( \frac{1}{T} \int_0^{t_1} (V_R^2(t) - V_L^2(t)) * dt + \frac{1}{T} \int_{t_1}^T (V_R^2(t) - V_L^2(t)) * dt \right) \quad \text{Equation 4-3}$$

$$= \frac{c}{2} * [(V_{R(high)}^2 - V_{L(high)}^2) * D + (V_{R(low)}^2 - V_{L(low)}^2) * (1 - D)]$$

where the subscripts high and low indicate the respective voltages at the left and right side of the droplet when the input is positive (high) or negative (low). Equation 4-3 predicts the actuation force from the instantaneous voltage. In reality, it is very difficult to measure the voltage behavior due to the dynamics of the system. In addition, when the droplet is not centered, i.e. the capacitance is not equal between the left and right side, the voltage across the dielectric will change. To better understand the voltage response of the EWOD system, Matlab SimElectronics® was used with ideal elements to show the voltage variation of the circuit. The droplet position and input duty cycle relation were developed using the simulation results.

#### 4.4 Electrical Model and Simulation

Matlab SimElectronics® was used to simulate the idealized circuit behavior using an idealized diode model (piece-wise linear diode with 0.1 V turn-on voltage). The resistance in the system was neglected. The input voltage was set at 1000 Hz and the duty cycle of the input was varied. The effect of droplet position was simulated by varying the capacitance of the left and right capacitor while keeping the total capacitance ( $C_{Left} + C_{Right}$ ) fixed at 1 nF. This models

the case of a droplet constrained by wetting to a plate in order to maintain a constant area of contact as long as the width of the gap between the electrodes is negligible. This condition is adequate for the center regions, but may breakdown at extreme positions.

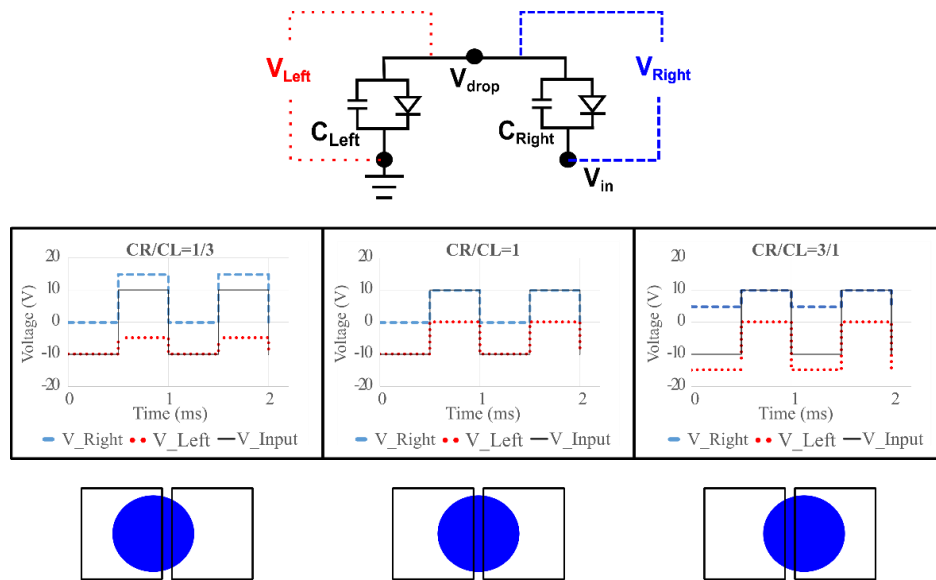


Figure 4-2: Top: the circuit representation of a co-planer electrowetting droplet with idealized diodes.  $V_{drop}$  is the droplet voltage. Middle: the voltage response of the simulated circuit when the capacitance was varied. The supplied signal was a 50% duty cycle square wave at 1000 Hz, -10 V to 10 V. The total capacitance is 1 nF. Bottom: the corresponding droplet positions at a given capacitor ratio. With a 50% duty cycle, the droplets are only stable in the middle position.

Figure 4-2 shows the circuit setup and the voltage variation across the interface at 50% duty cycle for three different droplet positions (capacitance ratios). It was found that the peak voltages were only a function of the capacitance ratio between the two capacitors, regardless of the duty cycle input. When the capacitances were not equal between the left and right side ( $C_{Left} \neq C_{Right}$ ), the capacitor with larger capacitance would drive the voltage of the smaller capacitor above the input voltage. Both of the diodes prevent current conduction in steady-state and the droplet acquires a net charge ( $V_{drop} \neq 0$ ). The value of the respective voltages as a function of the input voltage and the capacitance of the two capacitors are listed in Table 4-1.

Table 4-1: Simulated voltages as a function of the capacitance of the left and right capacitors.  $V_{in}$  is the input voltage. High is when the input is positive and low is when the input is negative.  $V_{Right}$  and  $V_{Left}$  are the voltages across the dielectric at the left and right side of the droplet, respectively.

	$C_{Right} > C_{Left}$		$C_{Right} < C_{Left}$	
	$V_{Right}$	$V_{Left}$	$V_{Right}$	$V_{Left}$
<b>High</b> ( $V = + V_{in}$ )	$ V_{in} $	0	$\frac{2 * C_{Left}}{C_{Right} + C_{Left}} *  V_{in} $	$\frac{C_{Right} - C_{Left}}{C_{Right} + C_{Left}} *  V_{in} $
<b>Low</b> ( $V = - V_{in}$ )	$\frac{C_{Right} - C_{Left}}{C_{Right} + C_{Left}} *  V_{in} $	$\frac{-2 * C_{Right}}{C_{Right} + C_{Left}} *  V_{in} $	0	$- V_{in} $

The area of the circular droplet covering the right and the left electrodes is defined in terms of a total area ratio ( $A_{right} = R_a * A_{Total}$ , and  $A_{Left} = (1 - R_a) * A_{Total}$ ). For a uniform dielectric layer, the capacitance can also be expressed using the area ratio ( $R_a$ ) since  $C = \frac{\epsilon}{d} * A$ . The time-averaged net force is found by integrating the force over a full period. By varying the relative time that the positive and negative voltages are applied (duty cycle), a point can be found where the droplet is in static equilibrium for a given area ratio. Higher voltages (and forces) on one side are offset by a shorter time over which the voltage is applied.

Rewriting Equation 4-3 in terms of the area ratio,

$$f_{net}(R_a, D)$$

Equation 4-4

$$= \begin{cases} \frac{c}{2} * \left[ \left( (2(1 - R_a)V_{in})^2 - ((2 * R_a - 1)V_{in})^2 \right) * D + (0 - V_{in}^2) * (1 - D) \right], & 0 < R_a < 0.5 \\ \frac{c}{2} * \left[ (V_{in}^2 * D) + \left( ((2 * R_a - 1)V_{in})^2 - (-2 * R_a * V_{in})^2 \right) * (1 - D) \right], & 0.5 \leq R_a < 1 \end{cases}$$

$$= \begin{cases} \frac{c}{2} V_{in}^2 * [4D(1 - R_a) - 1], & \&0 < R_a < 0.5 \\ \frac{c}{2} V_{in}^2 * [4 * R_a * (D - 1) + 1], & \&0.5 \leq R_a < 1 \end{cases}$$

Finally, by solving for the area ratio where the net force is zero ( $f_{net} = 0$ ) as a function of duty cycle, the relationship between the input duty cycle, and the area ratio ( $R_{eq}$ ) at which the droplet will be in static equilibrium for the given duty cycle is:

$$R_{eq}(D) = \begin{cases} 1 - \frac{1}{4D}, & 0 < D < 0.5 \\ \frac{-1}{4(D-1)}, & 0.5 \leq D < 1 \end{cases} \quad \text{Equation 4-5}$$

The relationship between the area ratio and the equilibrium position depends on the shape of a droplet. This work will consider the case of a droplet constrained to a circular shape. This generates a nonlinear relationship between position and area ratio. For a rectangular shape, the area ratio would be proportional to the linear position. When a droplet is wetting a solid object, the droplet can be made to maintain a circle or even a square shape by patterning the wetted region to match the desired droplet shape [74]. Thus both shapes are relevant to practical actuation tasks.

Equation 4-4 predicts that the actuating force is linearly dependent on the area ratio. The magnitude of the restoring force increases as the droplet's position moves away from equilibrium. For the idealized case, the input duty cycle is limited from 25% – 75% as any input beyond the range will result in a non-physical value of the area ratio required for static equilibrium ( $R_a < 0$  or  $R_a > 1$ ).

Diodes are required for this actuation mode. With the diodes removed, the droplet would be floating and would always be in equilibrium with equal areas on both electrodes regardless of the input waveform [64]. Without the diodes, the actuation force would not be polarity-dependent.



#### 4.5 Model Validation

To test these predictions, circular plates were placed on 50  $\mu\text{L}$  droplets and the position of the plate was measured as a function of the duty cycle of the applied square wave signal. Signal voltages varied from  $+V_{max}$  to  $-V_{max}$ . Sample substrates were prepared by photolithographically patterning 400 nm of titanium evaporated onto 75 mm x 50 mm clean glass slides (Corning<sup>®</sup>). After patterning, diluted Cytop<sup>®</sup> 809M (2:1 and 1:2 by weight solution to solvent ratio) was spin-coated and annealed according to manufacturer's specifications. The resulting Cytop<sup>®</sup> thickness was  $280 \pm 10$  nm and  $100 \pm 10$  nm, respectively. The thickness of the coating was measured by a Rudolph ellipsometer and verified by an Alfa step profilometer.

The metal film was patterned with a 300  $\mu\text{m}$  gap separating the left and right electrodes. The droplets were 0.1 M citric acid droplets with OS-30 silicone oil ambient. A circular glass plate (diameter 8 mm, thickness 0.1 mm) was carried by the 50  $\mu\text{L}$  droplet. The strong wetting between the droplet and the glass top plate constrained the droplet to remain circular during motion. Electrical signal was generated using a digital function generator (Agilent 33250A) and amplified (Kepco BOP 100-1M). The desired frequency (1000 Hz) was set with the initial duty cycle at 50% to position the droplet/plate at the boundary between the two electrodes. The driving voltage ( $\pm 30\text{V}$ , peak to peak) was chosen because it was the largest voltage without significant electrolysis with a 300 nm thick Cytop coating. After the voltage was switched on, the duty cycle was switched from high (70%), to low (30%), then back for several cycles to eliminate the effect of contact angle hysteresis. Finally, the duty cycle was adjusted to the full opposite of the desired value, and then back. For example, if the desired final input value was 40%, the input would go to 70% and then 40%. If the desired final input value was 65%, the input would go to 30% and then 65%. A digital image was taken from above to measure the

resulting position. The captured images were then analyzed using the Matlab® image analysis tool to find the centroid position of the glass plate.

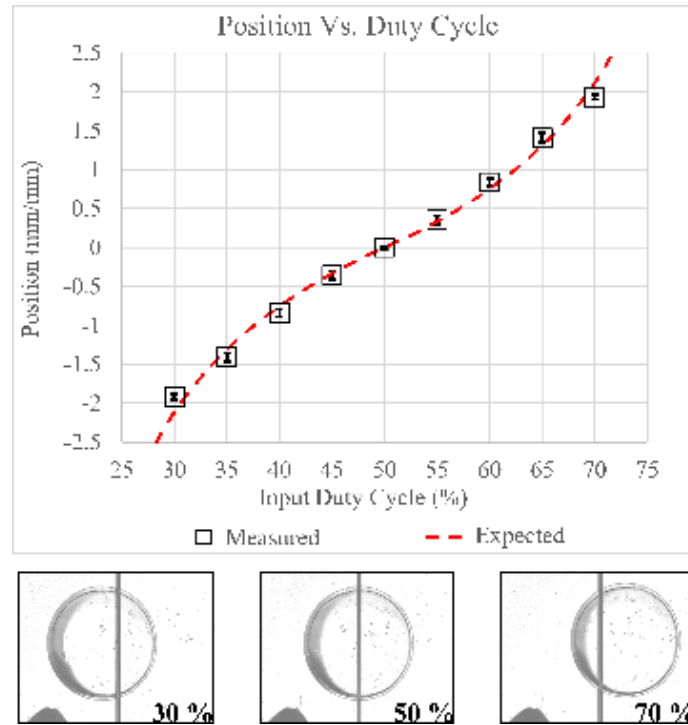


Figure 4-3: The measured plate position vs. duty cycle input. Tests were done using maximum available step size at 30 V<sub>pp</sub>. The squares represent the measured position of the plate centroid. The dashed line is the model prediction based on Equation 5. Five tests were performed for each data point and the standard deviation of the position was reported. The bottom row is images of the plates with the corresponding duty cycle input. For easier viewing, the colors of the images are inverted. The dark line in the middle of the image is the 300 μm gap between the electrodes.

Figure 4-3 compares the measured relationship between the position of the plate and the duty cycle of the input voltage compared to the predictions from idealized diodes. Five tests were performed for each data point. The error bars represent the standard deviation of the results.

Using Equation 4-5, the equilibrium area ratio  $R_{eq}$  was related to the centroid of the circle (accounting for the 300 μm gap), and the predicted centroid position from Equation 4-5 is plotted

against the measured positions. As predicted, the droplet/plate successfully switches between multiple equilibrium positions by changing the input square wave's duty cycle with very repeatable results (a standard deviation of 0.063 mm of the position). While the model based on idealized linear diodes fits the experimental data fairly well, there are deviations - especially at the extreme positions.

One source of the position error may be the difference between the contact area of the droplet and the plate. The model is based on the droplet position, while the experiments measured the plate position. In the oil ambient, the droplet contact area is smaller than the plate diameter, and the deviation could become significant at the extreme positions. To further improve the positioning at the ends, the droplet contact area could be tracked, or a contact angle between the droplet and substrate close to  $90^\circ$  could be used. The other significant error source may be in the assumption of idealized diodes. Real diodes have leakage current which would slow the response of the diodes and would cause larger deviations at the extreme positions.

#### **4.6 Time Response**

The response time of the droplet/plate under different duty cycle step sizes was investigated by applying a step change in the input duty cycle at time  $> 0$ , the plate position was tracked optically at 50 frames/second from above. Duty Cycle steps of 10%, 20%, 30% and 40% were tested. A total of five tests were done for each step size and the resulting average position vs. time information is plotted in Figure 4-4 (left).

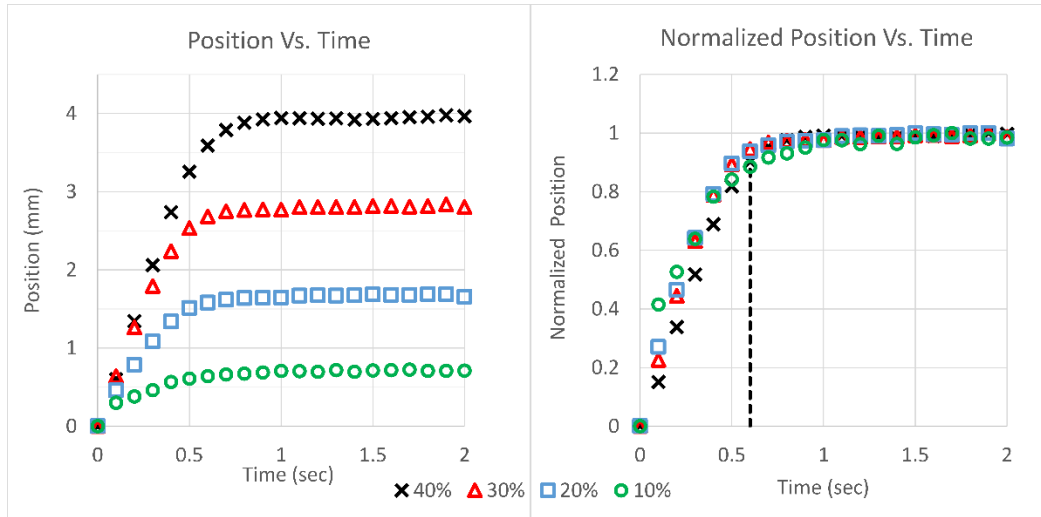


Figure 4-4: Left: the position vs. time plot of the actuated plate under different step changes in duty cycle. A total of five tests were done for each set of data, the average values are plotted. The standard deviations of the positions were between 0.04 and .012 mm (smaller than the markers used). Right: the graph shows the normalized position (dividing the position by its steady state location) vs. time in seconds. All tested cases reached 90% of steady state positions in less than 0.6 second.

Figure 4-4 shows the response in both distance and distance normalized by the steady state position. The characteristic time for the plate to reach 90% of the steady state position was found to be less than 0.6 seconds for the voltage tested; no overshoot was observed. When the step change is applied, the restoring force would be at its maximum. As the droplet moves closer to its final position, the force rapidly decays due to the voltage shift caused by the capacitance change, and dissipative forces such as hydrodynamic shear (both within the droplet and the medium). The combined effects result in a “soft landing” effect which could serve as an additional bonus in moving delicate components.

#### 4.7 Accuracy and Repeatability

To evaluate the dependency of the droplet position on the step size, another series of experiments were performed. The droplet/plate was set at the center first by applying a 50% duty

cycle, and then the input duty cycle was ramped up to 70%, down to 30%, and then back to 50%. The duty cycles were ramped in fixed steps of 10% every 2 seconds and the corresponding position to each input was recorded. All tests were repeated five times on a fresh spot with new droplets. The previous experiments, which used the maximum available step size, were compared to the fixed 10% step sizes. For the two step sizes investigated, the positioning accuracy was measured relative to the predicted position from Equation 4-5 using the idealized linear diodes. The maximum deviation (worst case) from Equation 5 is presented as the accuracy of the system for each condition. The standard deviation in positioning was calculated for each duty cycle input, and the average of the standard deviations across all positions is presented as the bidirectional repeatability. For unidirectional repeatability, the standard deviations of the position was calculated separately for increasing and decreasing duty cycles; the maximum value is listed. The results are listed in Table 4-2, together with the results from previously experiments with the maximum step size.

Since lower voltage is also preferred for many applications, a thinner leaky dielectric with lower input voltage was also investigated. The thickness of the dielectric was  $100 \text{ nm} \pm 10 \text{ nm}$ , and the input voltage was  $10 V_{pp}$  as the largest that avoided electrolysis. The above tests were repeated, and the positioning accuracy and repeatability were calculated for comparison. The data are summarized in Table 4-2. At the lower voltage (thinner dielectric), the repeatability deteriorated significantly, which suggests that fluid friction and other losses are significant relative to the actuation force. Although the unidirectional repeatability did not improve significantly with step size for either sample type, the higher actuation voltage did significantly reduce the variation. The large difference between bidirectional and unidirectional repeatability is likely due to actuation losses from viscous drag and contact line friction. The average

deviation from the prediction (Equation 4-5) was 0.106 mm (2.3% of the plate diameter). The accuracy of the system could be improved by utilizing a more accurate position model, or by substituting an empirical relationship for Equation 5. The repeatability of the system, which is the largest standard deviation from the average position, was 0.063 mm (0.8% of the plate diameter).

Table 4-2: The accuracy and the repeatability of the actuation system as a function of the step size

	30 V <sub>pp</sub> / 300 nm thick Cytop		10 V <sub>pp</sub> / 100 nm Cytop	
	10% Step Size	Max Step	10% Step Size	Max Step
Accuracy (mm)	0.181	0.181	0.293	0.191
Bidirectional Repeatability (mm)	0.153	N.A.	0.204	N.A.
Unidirectional Repeatability (mm)	0.08	0.063	0.189	0.182

Comparing the electrowetting number ( $\eta = \frac{\epsilon\epsilon_0}{2\gamma} * \frac{V^2}{d}$ ) at the testing voltages, the ratio is 3:1 between the thicker coating (300 nm/30V) and thinner coating (100 nm/10V<sub>pp</sub>). Thus, the actuation force should be three times higher for the thick coating/higher voltage combination since the actuation force is proportional to the electrowetting number. On the other hand, contact angle hysteresis which is the difference between the advancing contact and the receding contact angles, or the energy lost per unit contact line [123], can remain fairly constant under EWOD actuation [124]. The higher electrowetting number/actuation force improved repeatability due to the higher applied force relative to the dissipative forces.

Since the actuation force and contact line friction are both proportional to the plate diameter, it is expected that the accuracy and repeatability could scale linearly with the plate/droplet diameter. Smaller plates, should achieve higher positioning accuracy. A surface texture could be introduced to decrease contact angle hysteresis, but may also reduce the electrowetting actuation force due to the reduced droplet/substrate contact area [125]. Li and Mugele have shown that AC electrowetting inputs can significantly decrease the contact line friction effects [91]. It is possible that the contact line friction effects could be reduced by selecting the actuation frequency to maximize this effect. While duty cycle steps below 5% did not show consistent actuation, the applied duty cycle is continuously variable so that any plate position between the extreme testing positions could be achieved using this arrangement.

#### **4.8 Conclusion**

This work demonstrates a novel actuation/control scheme using electrowetting on dielectric with coplanar electrodes. Utilizing the unique diode-like properties of the electrolyte/dielectric/metal combination, AC square waves were used to move a droplet carrying a glass plate in steps that were a fraction of the electrode size. Unlike conventional EWOD driven droplet transportation, multiple stable positions within the electrodes could be reached by adjusting the duty cycle of the input square wave.

An electrical model was simulated using idealized electrical elements. The relationship between the input duty cycle and the responding droplet position was developed based on the simulation results. These results show that the position can be controlled through the central region of the electrode width, but there is no duty cycle that achieves a stable position on the extreme edges of the electrodes. The relation was experimentally validated by measuring plate position as a function of the duty cycle of the input signal. The idealized model matched the

measured positions to within 2.5% of the droplet position. Repeatability of the actuation system was just 0.7% of the droplet diameter for large steps. The repeatability is shown to decrease when taking smaller steps or when actuated at lower voltages. The error is attributed to the contact line friction in the experimental setup. The accuracy of the system could be improved by using a more advanced circuit model which uses non-ideal diodes. These results could also be improved through reduction of contact line friction. Similar positioning repeatability should be possible anywhere within the testing region. This is a substantial improvement in droplet control compared to existing close-loop methods that achieve steps that are only 20% of the droplet size.

In conclusion, by moving the droplet sub-electrode in a deterministic manner, the proposed control scheme could improve the positioning accuracy of the droplet while reducing the electrical wiring complexity inherent in electrowetting systems. A stepped actuation with DC voltage could be used for large motion, and fine positioning accomplished by varying the duty cycle of an AC input. Potentially, this approach could be used to fabricate a droplet-based actuator/positioner to provide a new alternative for compact millimeter-scale actuators which can travel large distances while maintaining the positioning accuracy without the need to incorporate location sensing and feedback control.



## CHAPTER 5: RELIABLE CONTINUOUS ELECTROWETTING USING DIODES

The goal of this dissertation is to establish design parameters for droplet-based mechanical actuators using electrowetting. In mechanical actuators, either stepping or servo-type actuations are possible. The previous chapter demonstrated a novel microstepping technique to improve the precision of the droplet-based actuator. This chapter will show another reliable diode method to increase the reliability and performance of a diode-based actuation which is capable of continuous linear motion just as a servo motor.

### 5.1 Abstract

We demonstrate bi-directional continuous electrowetting by embedding metal-semiconductor diodes in the electrowetting substrate. Unlike conventional electrowetting on dielectric (EWOD), bi-directional continuous electrowetting uses a single electrode pair to actuate a droplet long distances. As long as the voltage potential is maintained between two electrodes, the droplet moves toward the electrode with the higher potential. However, previously reported material systems had limited success in repeated actuation. In this work, diodes based on the Schottky barrier were fabricated by forming contacts between titanium and low concentration n-type silicon. The performance enhancements were evaluated using current-voltage measurements. When the titanium is coated with gold in order to limit electrochemical reactions, the Schottky diodes achieved superior performance compared to previously proposed electrochemical diodes. Droplet speed ranged from 8 mm/s to 240 mm/s. Under repeated

actuation, the speed of the droplet showed no degradation for up to 2000 cycles (experiment duration).

## 5.2 Introduction

Electrowetting uses an external electric field to manipulate discrete droplets on a planar surface [24, 66]. The most common configuration uses multiple electrodes on a substrate to create a voltage gradient under the droplet. The asymmetric voltage changes the apparent contact angles between the front and the back of the droplet to create an energy gradient that generates droplet motion. Comparing to other droplet actuation methods such as magnetics [59] and surface acoustics [57], electrowetting generates larger actuation forces and is simpler to implement [94]. The large force capability of electrowetting-driven actuation enables a wide range of droplet volumes to be manipulated; nanoliter to microliter droplet manipulation is common in electrowetting-based devices [63]. The substrates used can be readily fabricated by conventional semiconductor processes and no external fixtures (channels/supports) are required.

Electrowetting, especially electrowetting on dielectric (EWOD), has been demonstrated in numerous lab-on-a-chip technologies to perform operations such as pumping, mixing, splitting and merging of droplets [63, 97]. EWOD also finds application in the optical field, such as variable focus lenses [32] and reflective display technology [34]. Electrowetting can also be used to move droplets in order to perform mechanical tasks as an alternative to silicon-based micro-electromechanical systems (MEMS); out of plane motion was demonstrated in [86]. Other in-plane actuation demonstrations include rotational/linear fluidic motors [78, 99], droplet-based conveyer system [64] and fluidic switch [126].

For mechanical actuation, common EWOD is analogous to electromagnetic motors in both actuation and control scheme. EWOD uses stepper-type actuation - the electrodes

underneath the droplet are turned on and off sequentially so the droplet can move to the next step. Continuous motion is accomplished by precisely powering each electrode, which is partially covered by the droplet. Similar to electromagnetic stepper motors, EWOD droplet actuation does not require position feedback as long as the actuation speed/force is within the system capability. If the electrode switching frequency is too high, the droplet will miss a step, the motion will stop, and the droplet position will be unknown. Electrical feedback such as impedance metering can be implemented to overcome the problem [40], but additional hardware and control algorithms are required. In addition, the electrodes in EWOD are turned either fully on, or fully off, which requires the droplet to take a full step each time. This in turn poses limitations on the maximum speed the droplet can achieve. This can also introduce additional complications in design and wiring of the system. For example, if the droplet needs to travel a distance of 20 times the droplet diameter, twenty electrodes are needed. Through-hole and multilayer substrates are usually required to accommodate the number of wires and switches needed.

On the other hand, “Continuous Electrowetting Effect” modulates the electrical double layer between liquid metal (mercury) and electrolyte/ambient solution [78]. Continuous motion is achieved by applying a voltage along the length of a channel. The metal droplet will be propelled towards the lower potential electrode as long as the voltage is maintained. The advantage of this type of actuation is the simplified electrode design and control. For linear actuation, only one pair of electrodes are needed. Large travel distances can be easily accomplished without using a large number of electrodes - this also simplifies the control. However, the speed of the droplet is limited by the maximum sustainable voltage of the electrical

double layer (typically less than 1 V), and closed-channel geometry and hazardous material limit the applicable area of continuous electrowetting-driven actuation.

Previously, we reported a different method to achieve continuous electrowetting based on the electrochemical effect of metal/electrolyte combination [26, 76, 77]. Electrolytic solutions were used to form/dissolve a thin protective oxide on valve metals such as aluminum and titanium. The electrolyte/electrode interface is effectively a diode which conducts current in one direction only. While these devices have shown reliable contact angle change [37] and stable performance in pairs [77], these improvements did not translate to the continuous electrowetting prototype devices. All of them have shown poor reliability when tested under repeated actuation. In search of better material combinations, a new type of diode is introduced. This paper reports the results of using embedded Schottky diodes on a high-resistivity silicon substrate to actuate electrolytic droplets. The current/voltage behavior of electrochemical diodes and metal semiconductor diodes are compared by I-V measurements. Working prototypes are demonstrated, and the droplet's speed and reliability data are reported

### **5.3 Operating Principle**

The operating principle of the proposed device is illustrated in Figure 5-1. When the conducting substrate has significant resistance, a voltage gradient is created along the substrate. When the conducting droplet bridges two or more diode sites, the diode at the high potential side (right) is reverse biased and no current is flowing. At the same time, the diode at the lower potential side (left) is forward biased due to the charge accumulation in the droplet. The effective potential difference induced by the substrate reduces the surface energy in the front of the droplet and lowers the apparent contact angle. This in turn, moves the droplet towards the higher voltage electrode. The same cycle repeats when the droplet moves to the next diode sites, the diode at the

front of the droplet is always reverse biased, and the diode at the back side of the droplet is always forward biased. As long as the voltage is maintained between the ends of the substrate, the motion of the droplet is sustained. When the polarity of the voltage is switched, the droplet's motion will follow the higher potential electrode [76].

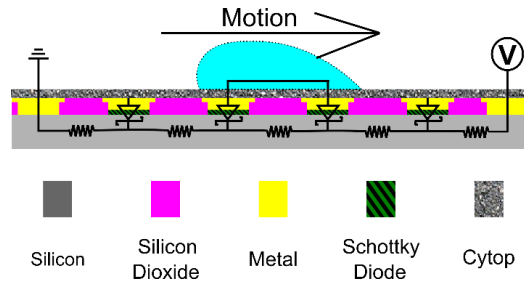


Figure 5-1: Bi-directional continuous electrowetting principle. A voltage is applied between the ends (ohmic contacts) of a resistive substrate. A conductive droplet with negligible resistance bridges two diode sites. The diode at the front of the droplet is reverse biased while the diode at the back of the droplet is forward biased. The asymmetrical voltage experienced by the droplet changes the apparent contact angle at the front of the droplet and moves the droplet towards the higher potential.

#### 5.4 Electrochemical Diodes Combined with Schottky Diode

In our previous bi-directional continuous electrowetting demonstrations, the working diodes were based on electrochemical reactions during actuation. Unlike the electrochemical diodes, which rely on the combination of the electrolyte and the metal interface, Schottky diodes are based on solid-state semiconductor physics which potentially could be used with any conducting fluids. Schottky diodes are based on the potential barrier formed when a metal-semiconductor comes into contact. At thermal equilibrium, the metal-semiconductor interface processes a certain built-in potential to ensure the fermi level is consistent within the junction. The resulting constant fermi level bends the energy band of the semiconductor [127]. For lightly doped n-type silicon, most metals form Schottky barrier contacts. When a positive bias is applied to the metal, the fermi level of the metal is lowered and electrons flow. When the metal is

negatively biased, the fermi energy of the metal increases and the potential barrier blocks current. The rectifying behavior of Schottky diodes have been widely used in the electronic industry due to their fast switching time and low forward voltage drop [128]. In electrowetting, Schottky junction formed by the electrolyte and silicon surface, have been utilized to move droplets by light (photoelectrowetting) [129].

Due to the different diode working mechanisms, the two diodes (electrochemical and Schottky) could be used simultaneously by connecting them in series - the electrochemical diodes work at the metal/electrolyte interface and the Schottky diodes work at the metal/silicon surface. In continuous electrowetting, the droplet is continuously moving from one diode to another, making measurements difficult. Prior work has relied on a modified test arrangement in which a single diode pair is used. For simplicity of measurement, the droplet is simulated by two electrically connected droplets (see Figure 5-2, top). Each droplet sits on an identical diode. A triangular voltage input (ramping pattern: 0 to -50 to +50 to 0 volts at 0.5 volts/20 ms) is applied between the two substrates, and the voltage and current of the droplets are measured using a two channel source meter (Keithley 2612A).

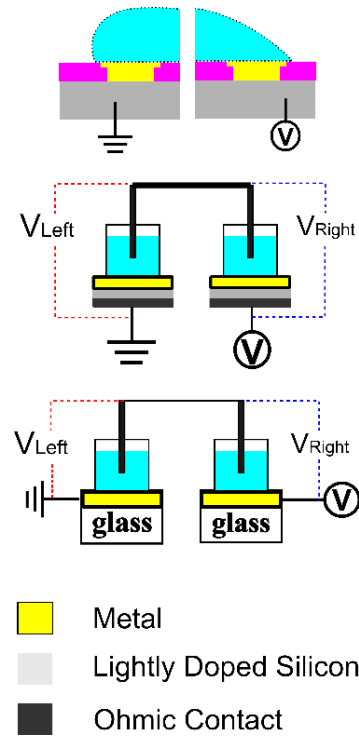


Figure 5-2: Illustration of the tube measurement setup. Top: the droplet under electrowetting actuation was split into two halves. Middle: Schottky and electrochemical diodes in series. Bottom: electrochemical diode alone.

The same cycle was repeated 2000 times with a 5 second off time between the cycles.

The voltage at the right side of the droplet was then calculated, taking the difference between the applied voltage and mid-point voltage. An actuation coefficient ( $\eta_{actuation} = 1 - 2 \frac{V_{drop}}{V_{applied}}$ ) was then calculated using the left and right voltages to determine the effectiveness of the diode system (see derivation in [77]). If the applied potential is positive,  $V_{drop}$  would be the voltage on the left tube, and if the applied voltage is negative,  $V_{drop}$  would be the voltage on the right tube. The value of the actuation coefficient should always vary between 1 and 0. A value of one represents the same actuation force as a grounded droplet system, and is only possible with an ideal diode. When the actuation coefficient is zero, there is no polarity dependence in the “diodes” and no actuation force is produced. The resulting data in terms of actuation coefficient are plotted against the number of testing cycles in Figure 5-3. Each set of combinations were

repeated three times, and the average value was plotted with the error-bars representing the standard deviation of each set.

We have previously reported on diodes based on electrochemical reactions alone using metals and different electrolytes [76, 77]. The best tested combination was titanium (Ti) with sodium sulfate ( $\text{Na}_2\text{SO}_4$ ) electrolyte. This is included as a standard of comparison for the Schottky/electrochemical combined diodes.

The Schottky/electrochemical diode substrates (Figure 5-2, middle) were fabricated using similar methods described in the materials section below, except the ohmic contact was made at the backside of the wafer rather than the ends. I-V measurements with contacting probes confirmed the current rectifying behavior of the Schottky diodes. For electrochemical diode substrates (Figure 5-2, bottom), metal film (titanium or aluminum of 400 nm thickness) was evaporated onto clean glass slides (3 x 2 in, Corning®). Circular plastic tubes (internal diameter: 8 mm, length: 10 mm) were attached to the front side of the diodes using epoxy. Before each test, the tubes were filled with electrolyte (0.1 M  $\text{Na}_2\text{SO}_4$ ), and the electrical connections to the tubes were made by inserting a 1 mm diameter activated titanium electrode inside. All other connections were made using copper wires.



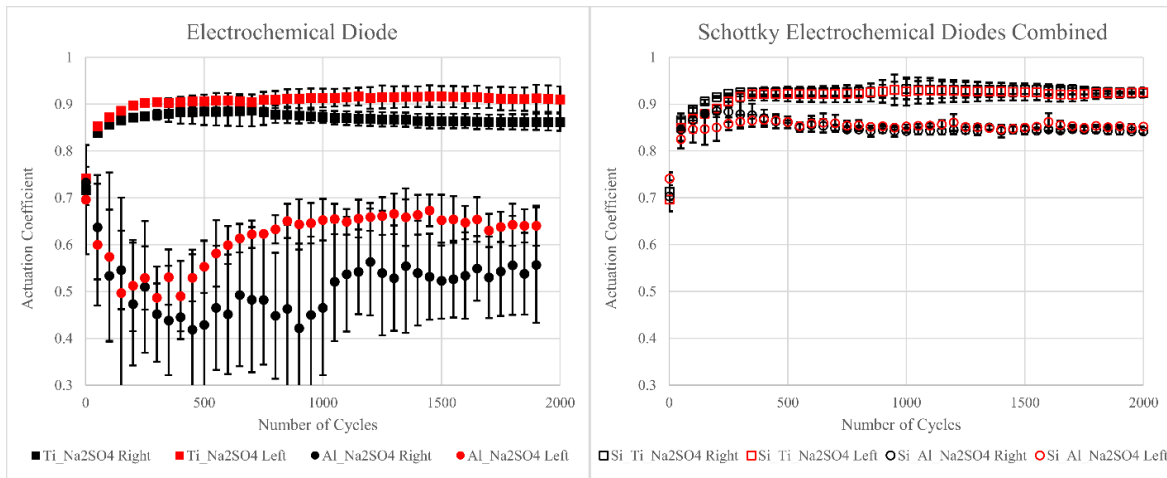


Figure 5-3: The resulting actuation coefficient vs. the number of actuation cycles with 0.1 M concentration  $\text{Na}_2\text{SO}_4$ . The average values and standard deviation of three trials are plotted. Left: the electrochemical diode alone. Right: Schottky combine with electrochemical diodes.

The data suggests the combination of Schottky and electrochemical diodes improved the performance of the electrowetting actuation in several ways. The first is that with the Schottky diodes, the left and right voltages are equal, whereas when electrochemical diodes were used alone, the resulting actuation coefficient was non-symmetrical (Figure 5-3, left). The higher actuation coefficient on the left side indicated a better diode-like behavior for the left metal/electrolyte interface. Since all experiments used a triangular wave - which started from zero, ramped to a negative peak (-50 volts), then positive (50 volts), then zero - the diode on the left would be reverse biased and the diode on the right would be forward biased during the first half of each voltage cycle. This could cause the anodic oxide formation on the metal surfaces being non-symmetric with the oxide being thicker on the left; this would explain the behavior. When electrochemical diodes are combined with Schottky diode, the additional Schottky diode prevented current flow in the initial cycle. As a result, the left and right actuation coefficients remained the same (as seen in the plot on the right side of Figure 5-3).

Additionally, the actuation coefficient was improved significantly with inclusion of Schottky diodes, with the aluminum showing particularly dramatic improvement, and the titanium reaching a value of 0.92. In [77], the combination of aluminum and sodium sulfate was deemed unsuitable due to the poor actuation coefficient. The same behavior was observed when electrochemical diodes were used alone as seen in Figure 5-3, left. But, with the addition of Schottky diodes, the aluminum/sodium sulfate combination achieved a 0.85 actuation coefficient (Figure 5-3, right) after 2000 actuation cycles, compared to 0.65 with the electrochemical diode alone.

However, both diode types showed a lower actuation coefficient during the initial 100 cycles before reaching steady state. The average current magnitudes are presented in Figure 5-4. The error bars show the standard deviation of each data set. The maximum current as seen by the voltage source was the current during the positive voltage sweep, and the minimum current was the current seen by the voltage source during the negative ramp. It is clear that incorporating the Schottky diodes drastically reduced the leakage current over electrochemical diodes alone. However, the initial higher current in the combined diodes still introduces undesirable variation in actuation. Because the Schottky diodes still contain an electrochemical passivating interface (Ti/electrolyte or Al/electrolyte), the electrochemical diode's metal-electrolyte interface still experiences some electrochemical reaction which causes the observed behavior.

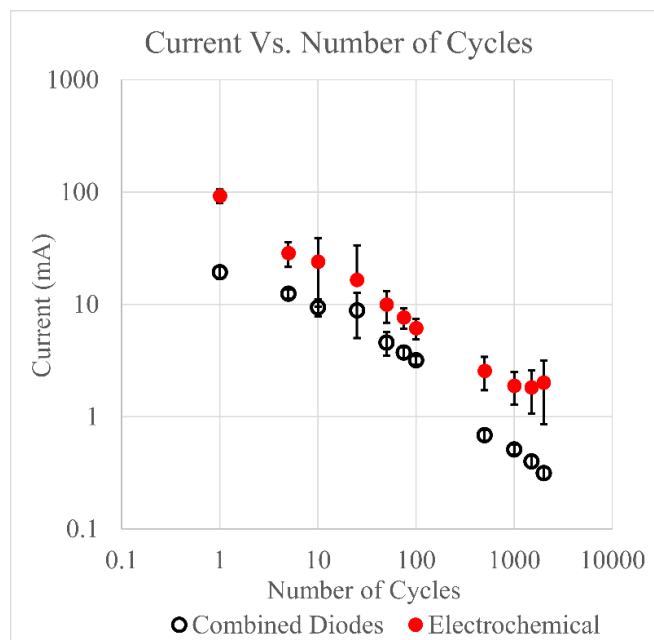


Figure 5-4: Peak current magnitude during cyclic tube tests for electrochemical alone and electrochemical plus Schottky diodes. The average value of three tests are presented and the error bars show the standard deviation of the data.

While these tests show clear benefit from incorporating Schottky diodes, results still change with repeated cycling due to the electrochemical interactions that could hinder the actuation in the initial cycles. To assess this effect, continuous EW actuators were fabricated using both combined electrochemical/Schottky diodes (titanium deposited on silicon and exposed directly to the electrolyte) and Schottky diodes only (500 nm gold overlayer shields the titanium from the electrolyte).

## 5.5 Materials and Fabrication

All substrates used were n-type (Phosphorus), high resistivity silicon wafers (100 mm diameter, 525  $\mu\text{m}$  thick, orientation: 1-0-0 resistivity: 560 -840  $\Omega\text{-cm}$ ). An oxide mask ( $\sim 5000 \text{ \AA}$  thick) was grown using wet oxidation, and was patterned to expose the silicon for end contacts (the extreme left and right points in Figure 5-1). After standard RCA cleaning, phosphorus solid

source diffusion was performed in a Bruce diffusion furnace to establish ohmic contacts for the end electrodes (nitrogen atmosphere, 40 mins at 1000 °C). The diode sites were protected using an oxide mask during diffusion. After diffusion, the oxide mask was removed using 49% concentration hydrofluoric acid (HF). After another round of RCA cleaning, the wafers were processed in the furnace again to drive-in the dopant (oxygen and hydrogen atmosphere, 60 mins at 1050 °C). The resulting oxide film from the drive-in process was then thinned down (HF etch) to a final thickness of 2800 Å ( $\pm 200$  Å), to serve as the dielectric in electrowetting actuation. It was suggested [130] that thermal cycling could drive the dopant in the bulk to the surface of the silicon to alter the dopant concentration profile at the surface. This could interfere with reliable Schottky diode formation, so silicon at those locations were etched to a depth of  $\sim 1$   $\mu\text{m}$  using reactive ion etching (RIE). Titanium (1.5  $\mu\text{m}$ ), or titanium/gold ( $\sim 0.75$   $\mu\text{m}$  each), was then evaporated onto the substrate and patterned by a lift-off process. The resulting diode sites had a silicon contact diameter of 250  $\mu\text{m}$ . The metal spots were designed to be slightly larger than the diode sites (300  $\mu\text{m}$  diameter) so they can cover both the silicon and oxide surfaces. To prevent the test droplet from sliding off the substrate, 100  $\mu\text{m}$  high SU-8 rails were patterned along the length of the wafer, as well as the ends before the ohmic contacts. A  $\sim 30$  nm fluoropolymer Cytop® was applied as the top coat to enhance the non-wetting behavior of the droplet before the substrate was cut into its final dimension (32 x 7 mm). Due to the small thickness of the fluoropolymer coating compared to the oxide, it had negligible contribution to electrowetting actuation.

For all substrates, the actuation area was defined by the SU-8 rails (24 x 3 mm). For droplet speed testing, the diode center-to-center spacing was 2 mm. The spacing was chosen so

that the droplet (60  $\mu\text{L}$ , diameter  $\sim 5\text{mm}$ ) could bridge at least 2 diode sites at any time (see Figure 5-5, top).

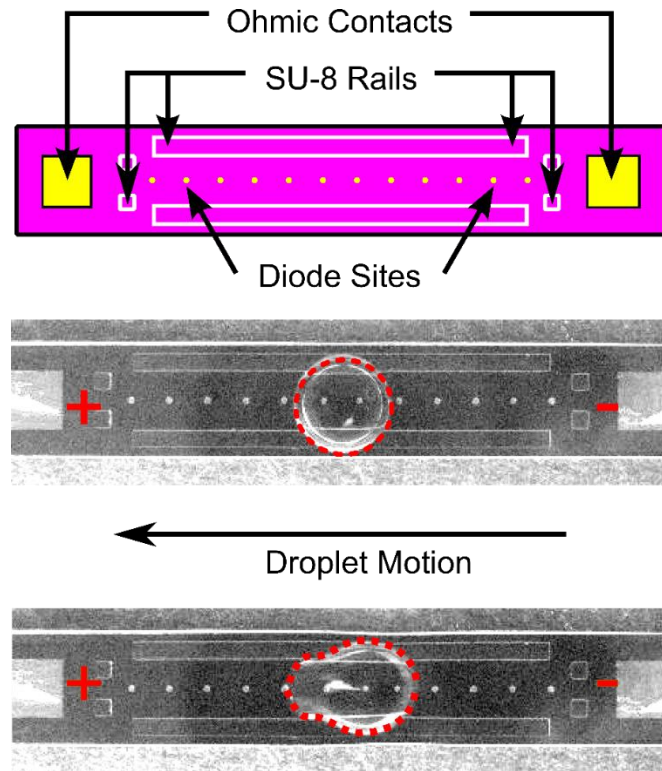


Figure 5-5: Illustration of bi-directional actuation prototype. Top: test prototype design. Middle: droplet actuation under 150V between the ohmic contacts. Bottom: droplet actuation under 210V between ohmic contacts. The positive and negative signs indicate the polarity of applied voltages and the dotted line shows the outline of the droplets.

## 5.6 Electrical Measurements

The fabricated Schottky Diodes were tested using a HP-4145B semiconductor analyzer. The grounding probe was connected to one end of the ohmic contact pad, and the sourcing probe was connected to one of the diode sites. A voltage ramp was applied at the rate of 0.1 Volt/ 0.1 second while the voltage and current were recorded at the same rate. The peak-to-peak voltage ramp was set at -50 to 50 volts. Light and dark ambient conditions, titanium and titanium/gold metal layers, as well as positive and negative ramps were tested with no observable difference between the sets. The I-V curves are presented in Figure 5-6 with the x-axis being the applied

voltage in volts and the y-axis being the measured current in milliamps. The dot number indicates the location of the diode sites, with 1 being closest to the grounding ohmic contact, and 12 being the furthest away from the grounding probe. As expected, all diode sites conducted current when forwardly biased. Their decreasing slopes in the I-V curve show that substrate resistance increases as the spacing between the diode and the end contact increases. The end-to-end contacts showed linear behavior confirming ohmic contacts. The measured end-to-end resistance value was 70.8 k $\Omega$ . Taking account of the test sample dimension (width: 7 mm, thickness: 525  $\mu\text{m}$ , length: 32 mm), the approximated resistivity was 813  $\Omega\text{-cm}$ , which was consistent with the specification from the manufacturer.

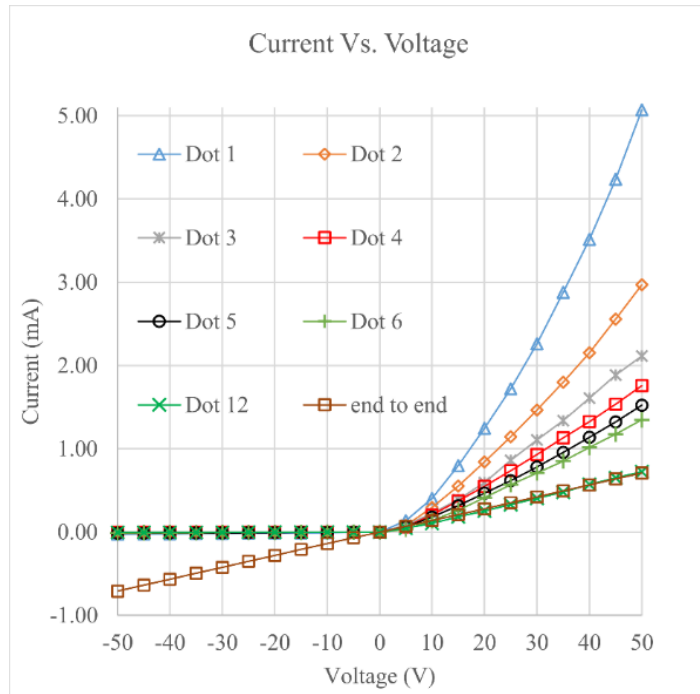


Figure 5-6: Current-voltage measurements of the fabricated Schottky diodes. The x-axis is the measured voltage (V) and the y-axis is the measured current (mA). The dot number indicates the location of the diode sites with 1 being closest to the ohmic contact and 12 being the furthest away. The end to end contacts were also measured to extract the total resistance of the substrate.

## 5.7 Droplet Speed Testing

All tests were performed in an oil ambient (silicon oil OS-30 from Dow Chemical company) to reduce the effect of contact hysteresis. Each test used a fresh 60  $\mu\text{L}$  sodium sulfate aqueous solution with 0.1 M concentration. The ohmic contacts on the end of the test strip were connected to a Masuzada high voltage amplifier. An overhead camera was used to record the position of the droplet. A custom Labview program was used to trigger the camera at a rate of 50 Hz while supplying the voltage signal to the amplifier. The captured images were processed in a Matlab image analysis tool to extract the position of the centroid of the droplet at each time point.

In actual device testing, only limited motion of the droplet was achieved by the electrochemical/Schottky combined diodes. The droplet would move in an unsteady stop/start motion or halt entirely part way. This is likely due to the initial low actuation coefficient in the combined diodes. In contrast, actuators with Schottky diodes alone (titanium electrodes with gold coating) achieved repeatable actuation. Therefore, further experiments were carried out using only the standalone Schottky diodes.

Average droplet velocities were measured by measuring the number of frames taken to traverse the strip. The resulting data is plotted against the actuation voltage in Figure 5-7 and the extracted average velocities range from 8 mm/s (150 V) to 240 mm/s (240 V). A parabolic fit is used to show the relation between the average velocities and the actuation voltages. Since the actuation force is related to the applied voltage squared (Young-Lippmann equation), it seems reasonable that the average velocities scale the same, as shown by other researchers [131, 132].

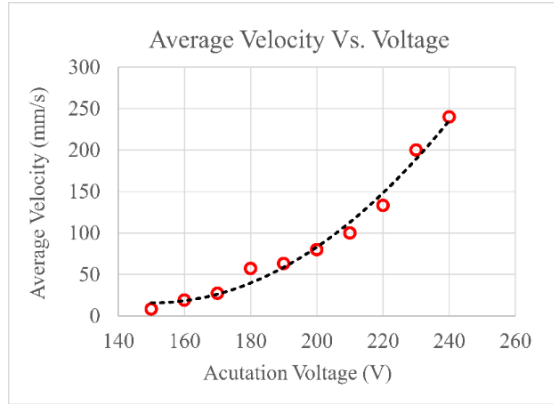


Figure 5-7: The average velocity of the droplet vs. the voltage. The actuation voltages range from 150 V to 240 V between the contacting electrodes (32 mm separation).

The position vs. time plot of the droplet actuation is presented in Figure 5-8, with each line showing a different actuation voltage. The applied voltages between the end contacts range from 150 V (minimum actuation voltage, Figure 5-5 middle), to 240 V (maximum sustainable current by the amplifier), which translates to a voltage gradient of 4.7 V/mm to 7.5 V/mm, respectively. The droplet/position relationship is only reported up to 200 V because at larger voltages, the large actuation force and/or drag forces from the oil ambient deformed the droplet and the image analysis methods could not accurately resolve the boundary of the droplet to extract reliable position data (Figure 5-5, bottom).

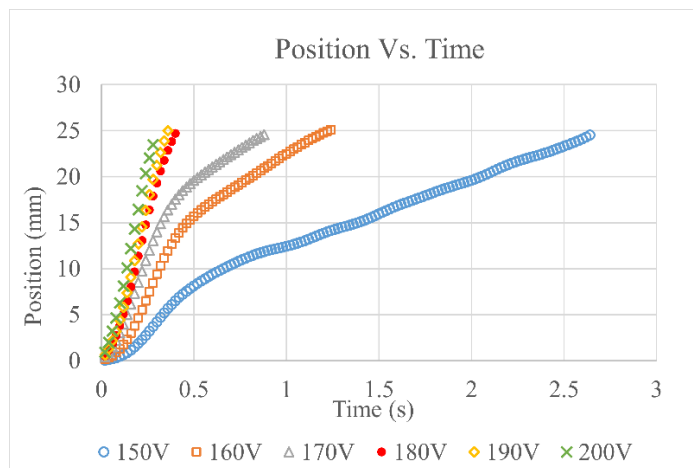


Figure 5-8: Droplet centroid position vs. time for different applied voltages.



For lower voltages ( $<170$  V), the droplet initially gained a higher velocity then reached a lower steady state value, as seen in Figure 5-8, left. For higher voltages ( $>180$  V), the droplet traveled across the entire length of the actuation region without experiencing this deceleration. Longer test samples would be required to see whether the same deceleration would occur at the higher actuation voltages. The decrease in velocity after the initial ramp was possibility due to a combination of factors such as the contact line friction and the viscous shear stress caused by the motion. Due to localized electrowetting force, the resulting contact line friction and viscous shear stress could be significant [132], especially for large sized droplet, as suggested in [131]. In our case, the droplet was under a constant actuation force due to the fixed width of the substrate (the force per unit contact line is fixed), the speed of the droplet increased until the bulk viscous force was fully developed and partially offset some of the actuation force. Additional work is needed to investigate the reason for the deceleration.

## **5.8 Actuation Reliability**

For the above droplet speed tests, the spacing between the diodes was chosen to ensure the droplet could bridge at least 2 diode sites at all times. The number of the diode sites (12 in total) were rather small to provide conclusive evidence on the reliability of the diodes. In addition, due to the relatively high velocity (8 mm/s) of the droplet, repeated actuation became troublesome to implement. In order to test the reliability of the proposed device, additional actuation substrates were fabricated with smaller device area and additional diodes. The device area was decreased to 18 x 3 mm, with the diodes being 100  $\mu\text{m}$  in diameter, and center-to-center spacing being 450  $\mu\text{m}$  with the addition of top and bottom rows. As a result, the total number of diode sites was increased to 105 (Figure 5-9, top). The smaller testing area and additional diode sites could promote break down of the device if the reliability was an issue.

Other parameters such as the droplet volume ( $60 \mu\text{L}$ ) and ambient conditions were the same as before. Since the droplet can now bridge a large number of diodes, this could lower the potential difference between the two sides of the droplet. As a result, a 120 V applied potential achieved a droplet velocity of  $\sim 5 \text{ mm/s}$ . An overhead camera was triggered at 10 Hz to capture the location of the droplet while it was repeatedly actuated back and forth along the length of the actuator. Each testing cycle required the droplet to travel from one end of the electrode to the other and back. Two thousand cycles were completed for the reliability test. The position vs. time of the initial 10 cycles and the final 10 cycles is plotted in Figure 5-9, bottom. Comparing the result, no degradation of the droplet actuation was observed; this indicates the robustness of the device.

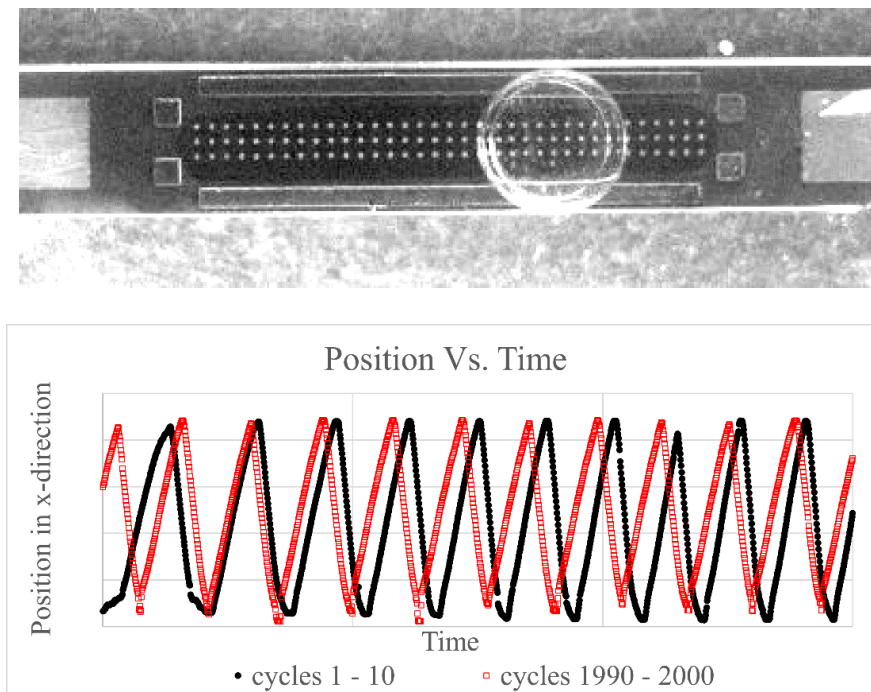


Figure 5-9: Cyclic droplet actuation. Top: substrate used during testing. Bottom: The relative position vs. time plot for the first and the final 10 cycles of the 2000 actuations.

## 5.9 Conclusion

In this paper, metal-semiconductor (Schottky barrier) diodes were embedded into the electrowetting substrate by evaporating titanium metal film on low concentration n-type silicon. The resulting Schottky barrier was used as replacement for the electrochemical diodes in bi-directional continuous electrowetting. From current-voltage measurements, it was found that electrochemical diodes based on passivation/etching metals could limit the performance of the device. By adding a gold overlayer, the Schottky diodes were shielded from electrochemical reaction and device reliability improved. These devices achieved high actuation speeds of 240 mm/s, comparing to the previously reported 32 mm/s [76]. In addition, the minimum actuation voltage was reduced from 291 V/28 mm [76] to 150 V/32 mm, a more than 50% reduction. More importantly, the reliability of the device increased drastically with Schottky diodes. After two thousand cycles of actuation, no device degradation was observed.

Unlike conventional electrowetting on dielectric actuation, bi-directional continuous electrowetting simplifies the control and fabrication needed for manipulating discrete droplets. This work demonstrates a reliable material system for continuous actuation, which when paired with a position feedback mechanism, could enable servo-style actuation. This would complement the primary stepping actuation available in electrowetting, and open additional possibilities to use a droplet for mechanical actuation. The wiring simplification would be particularly powerful if implemented in a two-dimensional actuator.

## CHAPTER 6: VERTICAL LOAD OF DROPLETS

This dissertation identifies the key parameters for a droplet-based mechanical actuator using electrowetting. The relevant information about electrowetting on dielectric and electrowetting-based droplet actuators were presented in the last section. In this chapter, numerical simulation was used to evaluate the load bearing capability of droplet-based actuators. Key design parameters such as the volume of the droplet, the weight (load) the droplet can support, and the vertical stiffness of the actuator are examined in detail. A relationship between these interconnected parameters is established by case studies to provide a tool for designing actuators. Design criteria for droplet-based actuators is summarized at the end of the chapter.

### 6.1 Introduction

Due to scaling relations, capillary force becomes dominant as length decreases below the millimeter scale. Comparing to other forces such as electrostatics and magnetics, capillary force spans across much wider length scales - from micrometer to millimeter [13]. The relatively large magnitude of the capillary force has been exploited by a number of research groups to perform mechanical operations such as grasp and release [22, 133], out of plane self-assembly [14], and vertical actuation via electrowetting [119]. A common grasp and release configuration utilizes the tensile force exerted by a capillary bridge between two wetting surfaces (the contact angle is less than  $90^\circ$ ). When the surfaces are non-wetting (contact angle is greater than  $90^\circ$ ), a compressive force exists when the two surfaces are close together [134, 135] as in Figure 6-1.

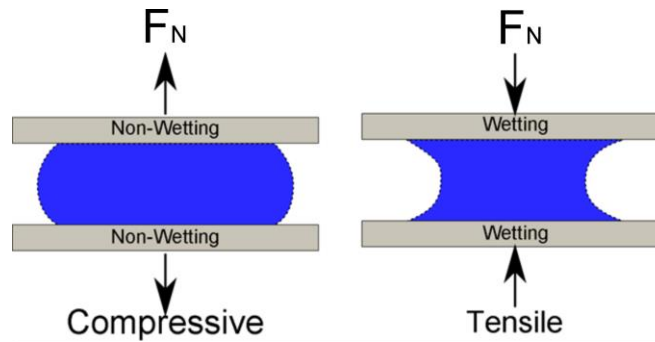


Figure 6-1: Tensile and compressive forces from a capillary bridge formed by two parallel surfaces. When the surfaces are non-wetting, the force pushes the plates apart. When the surfaces are wetting, the force pulls them together.

A new class of bearings based on the capillary bridge was proposed by several groups, and rotating micromachines have been demonstrated [99, 136-139]. The bearing surfaces were patterned by either surface coating and/or surface texture to control the location (and shape) of the droplet. Single droplets, multiple drops, and fluid rings have been used to support vertical loads by surface tension. The advantages of this type of bearing are low friction, wear resistance, and self-centering [136]. In addition, external force/torque can be applied either by an external field on the rotating rotor [139], or through the droplet [99, 138] which could further reduce the device's size. The same principle could be further extended to use droplets to support a vertical load in linear translational motion. Moon and Kim have demonstrated using electrowetting to move droplets which carried a solid platform for biochemical analysis [64]. In their demonstration, a voltage was applied to the actuation substrate which induced a contact angle change within the droplets. This propelled droplet translation, and the droplets transferred the solid platform. Since the droplets need to move relative to the bottom surface, the motion between the droplets and the top surface has to be limited for precise positioning of the top plate. A wetting pattern, either by coating or surface texture, could be the physical barrier to improve positioning reliability.

For linear bearings, the stiffness and load carrying capacity are critical parameters. The vertical stiffness determines the precision of the bearing in the transverse direction under varying loads; the maximum force capability would set the upper normal load limit for the bearings. For rotational bearings, it was noted that the maximum speed of the rotor was highly dependent on the thickness of the droplet due to the viscosity of the fluid [136]. It is important to optimize the load and the fluid volume, which have a large influence on the resulting gap height. The goal of this paper is to develop force and stiffness relationships for circular droplets supporting normal loads between two parallel plates. Analytical approximations are compared to numerical simulation of surface forces using Surface Evolver under varying surface constraints (wetting boundary and/or geometrical boundary). Depending on the wetting properties of the surfaces, different stiffness and load capabilities can be utilized for a droplet-based bearing. Based on these results, design strategies are proposed. This work can serve as a design guideline to implement droplet-based linear bearings in electrowetting driven applications, as well as in designing droplet-based rotating machines.

## 6.2 Normal Force Estimates

In its simplest form, a droplet-based bearing consists of a capillary bridge formed between two parallel surfaces. The interfacial tensions act at the triple point where the liquid, the solid, and the ambient meet. The angle between the liquid and solid is the contact angle. Lambert and co-workers have shown that both the Laplace approach, and the interfacial energy approach are equivalent [140]. Here, we will take the Laplace approach. Given the condition that the characteristic dimension is much less than the capillary length ( $\sqrt{\frac{\gamma}{\rho g}}$ ), where  $\gamma$  is the surface

tension,  $\rho$  the relative density of the droplet and the ambient, and  $g$  the acceleration due to gravity), the effect of gravity on the fluid can be neglected.

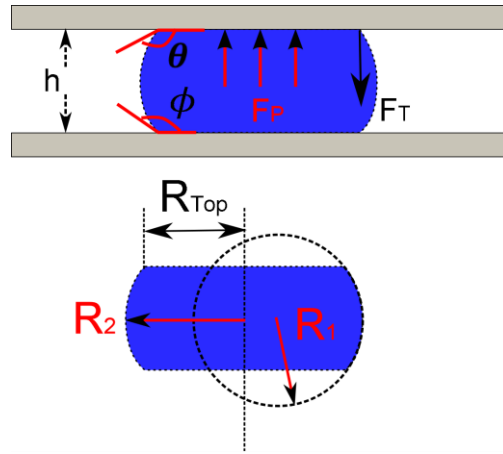


Figure 6-2: Capillary bridge between two parallel surfaces. When the top and bottom contact angles ( $\theta$  and  $\Phi$ ) are greater than  $90^\circ$ , the pressure force ( $F_p$ ) pushes the top plate upwards and the surface tension force ( $F_T$ ) acts downwards to pull the plates together. The two principle radii of curvature ( $R_1$  and  $R_2$ ) can be used to calculate the pressure difference across the interface.  $R_{Top}$  is the contact radius of the droplet to the top plate.

As shown in Figure 6-2, the bottom surface is fixed, and the separation distance ( $h$ ) is known. The forces acting on the top plate are the surface tension force, and the pressure force. The surface tension component acting on the top plate is the vertical force acting downward on the plate:

$$F_T = 2\pi R_{top} * \gamma \sin(\theta) \quad \text{Equation 6-1}$$

where  $\gamma$  is the interfacial tension of the liquid-ambient,  $R_{top}$  is the radius of the contact area, and  $\theta$  is the contact angle of the liquid and top plate. The pressure force, which originates from the pressure jump across the liquid/ambient interface, can be calculate using the Laplace pressure equation:

$$F_P = \pi R_{top}^2 * \Delta P = \pi R_{top}^2 * \gamma \left( \frac{1}{R_1} + \frac{1}{R_2} \right) \quad \text{Equation 6-2}$$

where,  $R_1$  and  $R_2$  are the principle radii of the curved interface. Giving the separation distance ( $h$ ) between the plates, one principle radius can be found by geometry:

$$h = -R_1 * (\text{Cos}(\theta) + \text{Cos}(\phi)) \quad \text{Equation 6-3}$$

where the top contact angle and the bottom contact angle are  $\theta$  and  $\Phi$ , respectively. The pressure can be either positive or negative depending on the contact angles. When both angles are larger than  $90^\circ$ , the pressure is positive, which acts to push the plates apart. When both angles are less than  $90^\circ$ , the resulting negative pressure force will pull the plates together. Now, if the radius of the capillary bridge is much larger than the separation distance ( $R_2 > h$ ), the second principle radius can be approximated by the radius of the plate contact ( $R_2 = R_{top}$ ). Then the total force ( $F_N$ ) on the top plate is then:

$$\begin{aligned} F_N = F_P - F_T &= \pi R_{top}^2 * \gamma \left( \frac{1}{R_1} + \frac{1}{R_2} \right) - 2\pi R_{top} * \gamma \text{Sin}(\theta) && \text{Equation 6-4} \\ &= \pi R_{top} \gamma \\ &* \left[ -\frac{R_{top}}{h} (\text{Cos}(\theta) + \text{Cos}(\phi)) + 1 - 2\text{Sin}(\theta) \right] \end{aligned}$$

Now, the aspect ratio is defined by normalizing the height with the diameter of the droplet ( $\bar{h} = h/2R_{Top}$ ), and is expressed by:

$$\frac{F_N}{\pi D_{top} \gamma} = \frac{-\text{Cos}(\theta) - \text{Cos}(\phi)}{4 * \bar{h}} + 0.5 - \text{Sin}(\theta) \quad \text{Equation 6-5}$$

For droplet-based bearings, the contact radius/diameter of the top surface can be controlled by either surface coating or roughness. Inside of the wetting region, the surface is hydrophilic. Outside of the region, the surface is hydrophobic with a contact angle greater than  $90^\circ$ . For linear motion, our goal is to use the electrowetting effect to actuate the droplet supporting the plate. So, the bottom surface has to be fairly hydrophobic without external input (zero electrowetting voltage). The reaction interest would be the normal load capability of



droplets with a known bottom contact angle. However, the gap height will change with external loads. If the contact line is at the boundary between two wetting regions, the contact angle can assume any value between the interior and exterior wetting angles without moving. With an unknown contact angle, the reaction forces must be found numerically using software such as Surface Evolver [141].

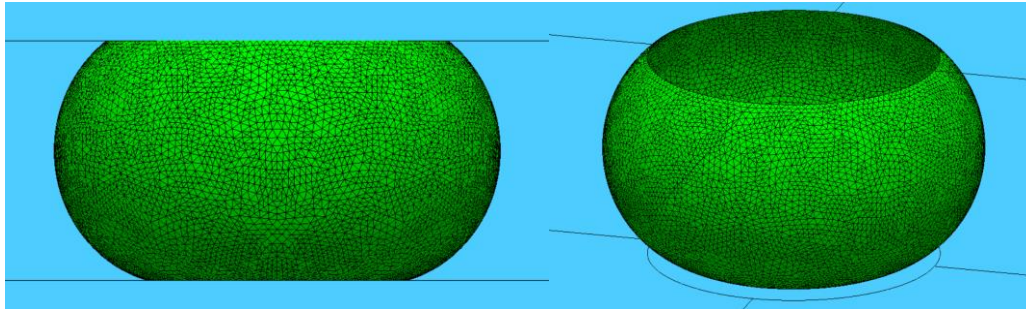


Figure 6-3: Surface evolver model of a droplet between two parallel surfaces.

Surface Evolver calculates the total system energy through a series of surface and line integrals. The equilibrium shape is found by a gradient-based energy minimization. In the simulation, a droplet with defined volume and contact angle condition on the top and bottom plates was constrained between two planes that represented the substrate and moving plate. The effect of gravity was not included in our simulation since the desired operating range of the droplet-based bearing is less than the capillary length (especially the gap height). In practice, the gravitational effect on the fluid forces could be eliminated almost entirely by matching the density of the ambient and the fluid. Once the shape of the surface was found, a small step in the z direction was taken (50  $\mu\text{m}$ ) and the energy was re-calculated. The normal force was found using the principle of virtual work ( $Fz = dE/dz$ ).

## 6.3 Simulation Results

### 6.3.1 Type 1 - Symmetrical Non-wetting

For axisymmetric wetting, the contact angles of the top and bottom are the same ( $\theta=\Phi$ ), and Equation 6-5 reduces to:

$$\frac{F_N}{\pi D_{top} \gamma} = \frac{-\cos(\theta)}{2 * \bar{h}} + 0.5 - \sin(\theta) \quad \text{Equation 6-6}$$

This was used as a benchmark for the Surface Evolver simulation. The surface tension for all types was fixed at 0.072 N/m. The variables used are listed in Table 6-1.

Table 6-1: Simulation parameters used.

Volume of the fluid	5 – 50 $\mu\text{L}$ (5 $\mu\text{L}$ increments)
Contact angle (both top and bottom)	165°, 120°, 110°
Gap height	0.5 – 3.0 mm

By changing the input variables, the normal force at each step is extracted. The resulting forces were normalized by the product of the top contact diameter,  $\pi$  and the surface tension value. The normalized force is plotted against the normalized height in Figure 6-4. When normalized, the force for a given contact angle collapses to a single curve for all droplet volumes. The simulation data (markers) agrees well with Equation 6-6 predictions (solid lines) for small values of aspect ratio for all contact angles and for contact angles closer to 90 degrees. For large contact angles (165°), the calculated force is higher than the simulated force, especially at larger aspect ratios. The error arises from using the contact radius as the principle radius of curvature.

Since the normalized force and the aspect ratio both scale with the diameter of the droplet, for given height, only marginal gain is achieved by using a larger diameter droplet when

the aspect ratio is greater than 0.1. However, a much higher stiffness in the vertical direction can be seen when the aspect ratio is less than 0.1.

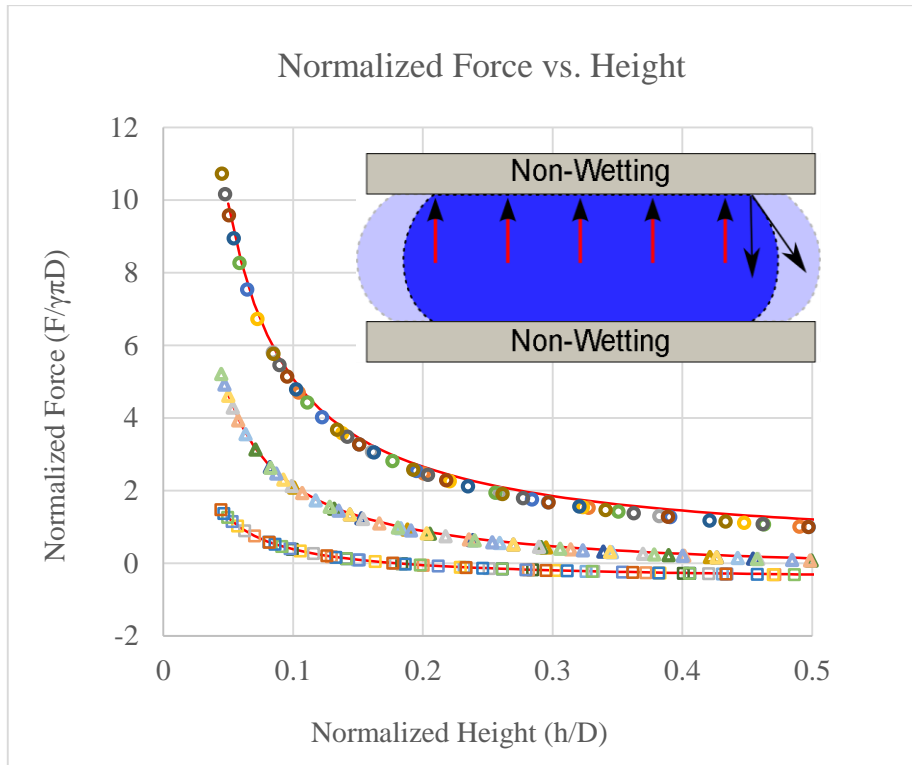


Figure 6-4: Normalized force vs. normalized height, type 1. For a symmetric capillary bridge on a non-wetting surface, the contact angles are the same top and bottom. Circular, triangular, and square marks are the simulation results for contact angles of  $165^\circ$ ,  $120^\circ$ , and  $100^\circ$ , respectively. Each data set includes simulation results for 10 droplet volumes used ( $5 - 50 \mu\text{L}$ ). The solid lines are the calculated values from Equation 6-6.

On hydrophobic surfaces, the surface tension forces act downward, opposite the pressure force. As the contact angle increases, this effect decreases. Figure 6-5 shows the force per unit contact area on the top plate with a  $50 \mu\text{L}$  droplet having various contact angles. As the contact angles increased from  $100^\circ$  to  $165^\circ$ , the force could increase by as much as a factor of 5 or more (see Figure 6-5). Higher contact angles and/or smaller aspect ratios should be used to support larger vertical loads.

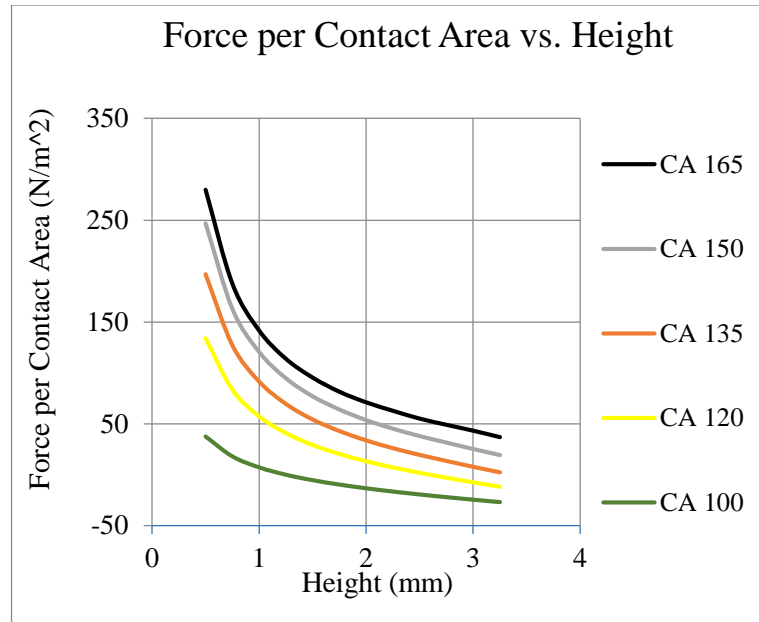


Figure 6-5: Force per unit area as the height changes. Each line indicates the different contact angles used for the top and bottom surfaces. The droplet's volume was fixed at 50  $\mu\text{L}$ .

### 6.3.2 Type 2 - Defined Wetting Region

In a practical bearing, the droplet must be constrained to stay stationary relative to one of the plates, while sliding on the other. This could be done by defining a specific wetting region on one plate, while the other plate remains hydrophobic. To evaluate this non-symmetric wetting, a circular region on the top plate was defined hydrophilic (contact angle =  $10^\circ$ ) with a different wetting radius ( $R_{\text{top}} = 2, 3, \text{ and } 4 \text{ mm}$ ). The bottom and top surface (outside of the wetting area) were both non-wetting (contact angle =  $165^\circ$ ). The droplet's volume was fixed at 50  $\mu\text{L}$ .

Vertical forces were extracted and then normalized by the top contact diameter and compared to Type 1. The results are presented in Figure 6-6. The normalized force follows the same curve at low aspect ratio when the top and bottom contact areas were greater than the hydrophilic region. As the height increases, the top contact line decreases until the edge of the contact line was constrained by the wetting region. The bottom contact area further decreased as

the height increases. The resulting force dropped off much faster in Type 2, especially for a smaller, small wetting radius. While the lower normal force is undesirable, the increased stiffness is favorable for normal positioning accuracy in both rotational and linear bearings. For a given top wetting area, this also allows the bearing to operate at a higher gap height with favorable stiffness. Larger gaps and smaller aspect ratios should reduce the drag introduced by the fluids.

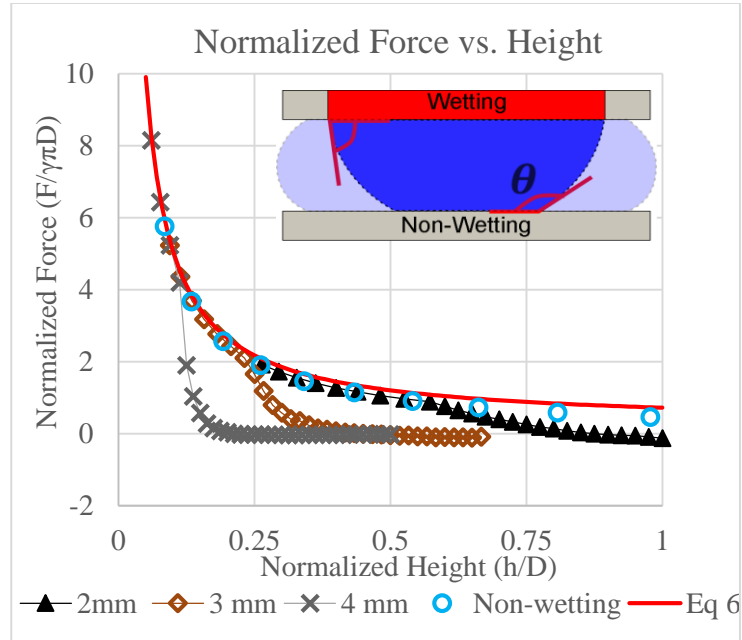


Figure 6-6: Normalized force vs. normalized height, type 2. The force was normalized by the product of the surface tension,  $\pi$ , and the top contact diameter. The circles are the simulation results from Type 1 (symmetric non-wetting, contact angle:  $165^\circ$ ), the line is the prediction from Equation 6-6. The cross, square, and triangle marks are the simulation results for different wetting radii (4, 3, 2 mm) when the droplet's volume was fixed at  $50 \mu\text{L}$ . The inset shows the wetting region on the top plate. As the gap height between the plate decreases, the droplet spreads out to the non-wetting region.

### 6.3.3 Type 3 - Constrained Top Wetting

Physical constraints can also be added to the edge of the wetting region to more reliably constrain the wetting boundary. This could be accomplished using a protruding surface as illustrated in Figure 6-7. The addition of the top overhang structure limits the spreading of the

top contact line so that effective contact angles over  $180^\circ$  (measured relative to the horizontal surface) can be achieved. The resulting force increases at a much faster rate than Type 1 and 2.

This would be the most favorable design for droplet-based bearings. High stiffness and large force could be achieved with larger gap heights when the contact line is constrained by both geometry and wetting. As discussed earlier, the viscous drag introduced by the droplet could impose a speed limit on the bearing. By operating at larger heights, the maximum speed of the bearing could be increased. This design can increase the working range of the bearing from 0.1 aspect ratio ( $h/D$ ) to around 0.5.

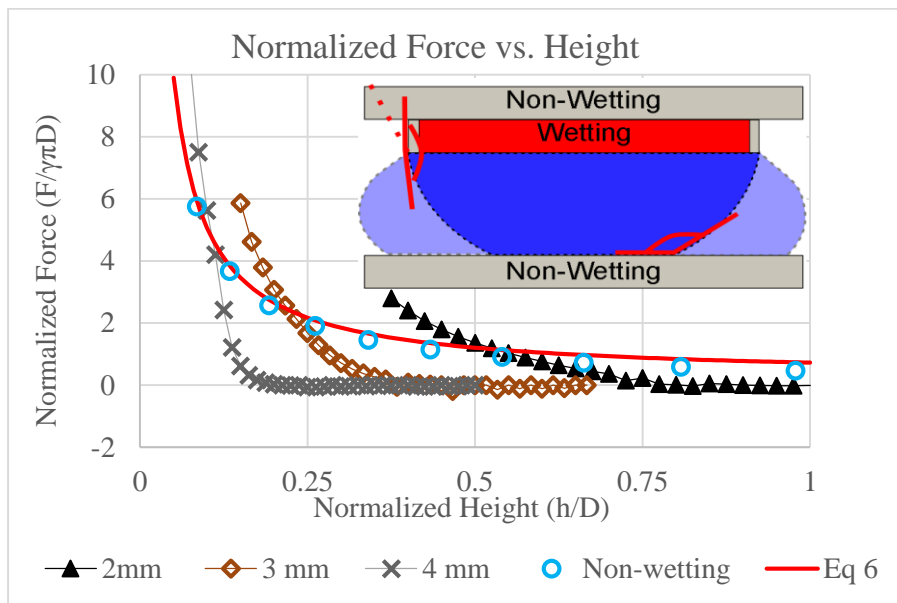


Figure 6-7: Normalized force vs. normalized height, type 3. The circles are the simulation result from Type 1 (symmetric non-wetting, contact angle:  $165^\circ$ , droplet volume  $50 \mu\text{L}$ ). The line is the prediction from Equation 6-6. The cross, square and triangle marks are the simulation results of different wetting radii (4, 3 and 2 mm) when the top wetting area was defined and constrained from moving beyond the geometry. The inset shows the wetting region and geometrical constraint on the top plate. As the gap height between the plate decreases, the bottom of the droplet spreads out, and the top edge is constrained.

#### 6.4 Design Considerations and Application in Electrowetting-based Actuator

To achieve precise translational motion in the x-y plane, the droplet's relative motion to the top plate needs to be minimized. Type 2 presented above limits the relative motion by constraining the contact line. For a given contact area (specified by the wetting and/or geometry), smaller droplet volumes would require less gap height to accomplish the same force. The force/displacement relationship shows the added benefit, in terms of stiffness, when the top edge is constrained (Type 3).

Electrowetting droplet-based actuators have been demonstrated in [64]. Four droplets were used to carry a solid platform in a linear translation. For a given loading parameter, the size and weight of the plate being carried is fixed. Equation 6-6 indicates droplet-based bearings favor large diameter or small gap height. Since the pressure force scales with the diameter squared, larger contact areas can support larger loads. However, a single droplet bearing does not provide much stiffness in the x and y axis [142] and would add additional uncertainty in plate placement [18]. By using multiple droplets, the plate could be constrained by the moments created by the additional droplets. Since two droplets define a line and three droplets define a plane, three droplets would be an appropriate minimum. However, uncertainty in the droplet volume could cause orientation errors. Using additional droplets would average out random volume errors and could improve the positioning accuracy further.

Since the primary goal is to use electrowetting to drive a droplet, the actuation force from the electrowetting could also benefit from additional droplets - the electrowetting force is proportional to the contact line length of the droplet [94], in this case, the droplet diameter [73].

Below are some case studies to demonstrate the tradeoffs when designing such a bearing. All the calculations are based on Equation 6-6. Although the equation is only applicable to type 1

wetting as described above, the calculated force should match closely to type 2 and 3. As for the stiffness, the type 1 solution could still be used as a lower bound for other cases (type 2 and 3). While the stiffness difference between Type 1 and Type 2/3 is substantial at large aspect ratios ( $>0.2$ ), the differences are not as significant at small aspect ratios such that this limit becomes useful. To find the exact stiffness for Type 2/3 cases, simulation software is needed to perform the calculations.

#### 6.4.1 Design Case 1 - Fixed Gap Height

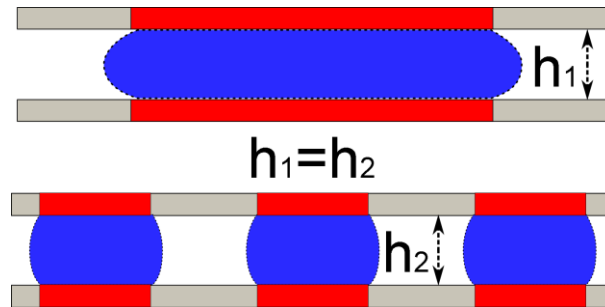


Figure 6-8: Case study 1: fixed gap height (1 mm) and fixed load (1078  $\mu\text{N}$ ). The wetting areas (hydrophilic) are the shaded region. This case compares single vs. multiple droplets for bearing application.

In this first case study (Figure 6-8), the normal force and the gap height are held constant. The number of droplets and the stiffness, as well as the droplet volume are variables. The calculated force should be applicable for all types of wetting, but the calculated stiffness is for type 1 only. From earlier analysis, the stiffness for type 2 and 3 wetting should be higher than the idealized condition presented here.

For a square glass plate (density 2200  $\text{Kg/m}^3$ ) with dimension of 10 x 10 x 0.5 mm, the minimal force needed to support the weight of the plate is 1078  $\mu\text{N}$ . Assuming an air ambient, and that water droplets give a surface tension of 0.072 N/m, and contact angle  $110^\circ$  on a Cytop coating: at 1 mm gap height, a single 6.8 mm diameter droplet would provide sufficient force to



support the droplet. However, due to stability issues mentioned above, multiple droplets are preferred. Table 6-2 shows the impact on the aspect ratio, total area needed by the droplets, and the projected length (the strength of the actuation force) when using multiple droplets. The supporting force is calculated using Equation 6-6, with the assumption that the area occupied by the droplet has straight side walls. This is most accurate for small values of aspect ratio, and contact angles near 90 degrees, and should be a good approximation for these cases ( $h/D < 0.3$ ,  $CA = 110^\circ$ ). The total stiffness is calculated by finding each droplet's stiffness, then modeling them as springs connected in parallel, taking the number of droplets then multiplying by the stiffness of each individual droplet.

Table 6-2: Case study of droplet(s) supporting a fixed load at a constant gap height, the contact angle is  $110^\circ$  top and bottom. The total supporting force is fixed at  $1078 \mu\text{N}$ , and the gap height is at 1 mm.

# of droplets	Volume of each Droplet ( $\mu\text{L}$ )	Aspect Ratio (h/D)	Diameter of the drop (mm)	Total Stiffness (N/m)	Minimum total area required ( $\text{mm}^2$ )	Total projected length (mm)
1	36.3	0.147	6.8	1.8067	36.3	6.8
3	16.6	0.217	4.6	2.48031	49.9	13.8
5	12.6	0.25	4	3.12578	62.8	20
7	10.8	0.27	3.7	3.7443	75.3	25.9

The table above shows the same load could be supported by a number of possible configurations, depending on the design goal. If the force per unit area is the main concern, the larger droplet should be used. If the stiffness is the driving parameter, multiple small droplets could achieve higher stiffness. If the actuation force from electrowetting is to be maximized, the maximum allowable number of droplets should be used due to the larger projected length from multiple droplets.

## 6.4.2 Design Case 2 - Fixed Stiffness and Droplet Diameter

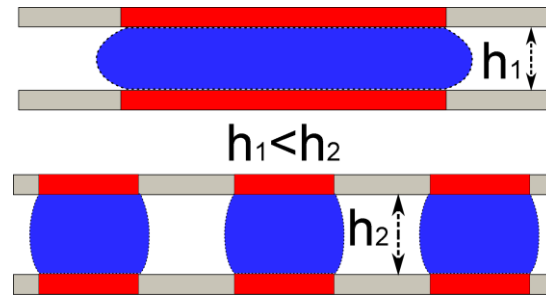


Figure 6-9: Case study 2: fixed stiffness (162 N/m) and fixed droplet diameter. The wetting areas (hydrophilic) are the shaded region. This case evaluates the impact on droplet volume and gap height when designed for stiffness.

Under external disturbance such as gravity, shock, and vibration, the error in positioning could increase drastically. In addition, when the gap height is small, minor displacements in the vertical direction could cause a large droplet diameter change. This could cause the spacing between the droplets to decrease until they merge. To account for the external disturbance, the stiffness needs to be the primary design goal. This case study (Figure 6-9) uses the same loading parameter as above, with the required load fixed at 1078  $\mu\text{N}$ . The total plate area is still 100  $\text{mm}^2$ . Instead of fixing the gap height, this case requires a maximum displacement of the top plate of  $\pm 10 \mu\text{m}$  at 150% overloading. This can be translated to a design requirement of fixed stiffness ( $\frac{1.5 \cdot 1078}{10} \frac{\mu\text{N}}{\mu\text{m}} = 162 \frac{\text{N}}{\text{m}}$ ). Other parameters such as the surface tension and contact angle remain the same (0.072 N/m,  $110^\circ$ , respectively). The same diameter of droplets were used. The gap height could be adjusted by varying the volume of the droplet. The same calculations were performed using Equation 6-6. As seen in Table 6-3, the aspect ratio needs to be small compared to the previous case in order to meet the high stiffness requirement. All other outcomes such as the total area required, and the actuation force are unaffected due to the fixed wetting diameter. The force approximation is suitable for all types of wetting conditions. However, due to the

higher stiffness of type 2/3 wetting, the gap height could be larger for the same stiffness when type 2/3 wetting is employed.

Table 6-3: Case study of droplet(s) with constant stiffness (162 N/m); the contact angle is 110° on top and bottom. The diameter of the top wetting region is the same as in case study 1.

# of droplets	Volume of each Droplet (μL)	Aspect Ratio (h/D)	Diameter of the drop (mm)	Height of the gap (mm)	Minimum total area required (mm <sup>2</sup> )	Total projected length (mm)
1	3.8	0.015452	6.8	0.105	36.3	6.8
3	2.1	0.026764	4.6	0.123	49.9	13.8
5	1.7	0.034553	4	0.138	62.8	20
7	1.6	0.040883	3.7	0.151	75.3	25.9

Another effect of the tradeoffs between design for force and stiffness can be seen in the rapid decrease of droplet volume. About one order of magnitude of reduction in volume is required for the increased stiffness. These small volumes could accentuate another error source, droplet volume variation could impact the alignment precision in the x-y plane. This could be offset by increasing the number of droplets to average out random variations.

## 6.5 Opposing Droplets

For linear bearing applications, the normal force and the stiffness under loading are the primary interests. Higher force enables a larger loading capability and higher stiffness would improve the rigidity of the joint. For optimal stiffness and force in the vertical direction, the plate should have both wetting and geometrical constraints. In addition, a preload on the droplet would force the bearing to operate in a higher stiffness range (case 3). When the supporting droplet(s) are all under the plate, the stiffness is non-linear - the stiffness increases as the gap height reduces. When using density matching the ambient, either the weight of the plate or the droplets can be counter-acted, but one of them would still be affected by gravity. We propose a symmetrical capillary bearing which uses two droplets to apply a preload to the plate. The

resulting force/stiffness could be symmetrical around the middle point, which could further increase the reliability of the device - either orientation around the x-y plane is possible. The simplified case with no wetting contrast is analyzed below (Figure 6-10).

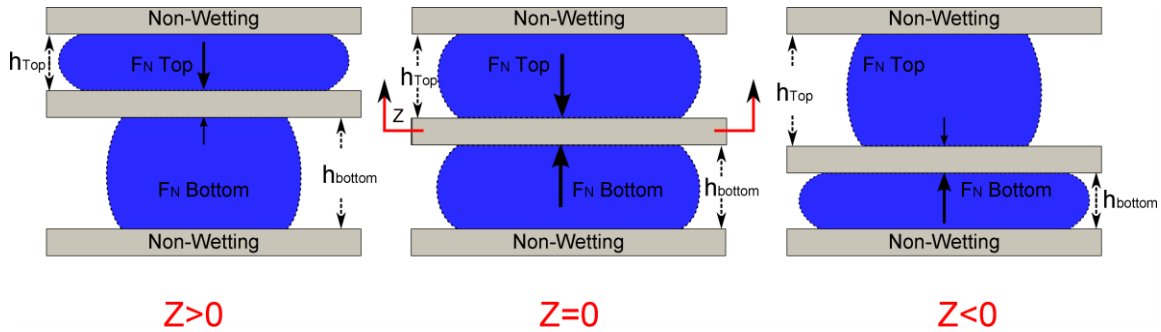


Figure 6-10: Opposing droplet configuration. Two identical droplets are used to provide support on either side of the center plate. Both the top and bottom plates are fixed. The resulting force and stiffness is symmetrical around the midpoint ( $z=0$ ). The left and right illustrations show the droplet shape when the center plate is displaced around the balance point.

To illustrate the force/displacement relationship, calculations based on Equation 6-6 were performed. The force was then normalized by the product of the equilibrium diameter ( $D'$ ) and  $\pi\gamma$ , and the change in height with respect to the middle point ( $dz$ ) was normalized by the equilibrium diameter ( $D'$ ). The results are presented in Figure 6-11. The main assumption is that the weight of the plate is counter-acted by the buoyancy force (plate density  $\approx$  ambient fluid density), and all the plates are non-wetting (type 1). The contact angle values used in the calculation were  $165^\circ$  for both the top and bottom. The maximum allowable height is fixed at 1, 0.5, and 0.25 mm for both the top and bottom gap (without the thickness of the middle plate,  $h_{Top} = h_{Bottom}$ ). The droplets volumes were  $50 \mu\text{L}$  each. In Figure 6-11, the top graph shows that the top and bottom droplets exert the same force, but in opposite directions around the center (dotted lines). The total force follows a non-linear but symmetrical curve (solid line). When designing a bearing, the droplet contact area could be specified, and the height can be tailored to suit a

variety of stiffness ranges. Due to the symmetrical force, the location of the plate and/or the stiffness in the z-direction could be fine-tuned by using either the volume of the droplet, the wetting pattern, or the gap height. Either one of these parameter changes could change the preload on the bearing, which could improve stiffness (demonstrated in Figure 6-11, bottom). As the total gap height decreases, the stiffness of the bearing increases.

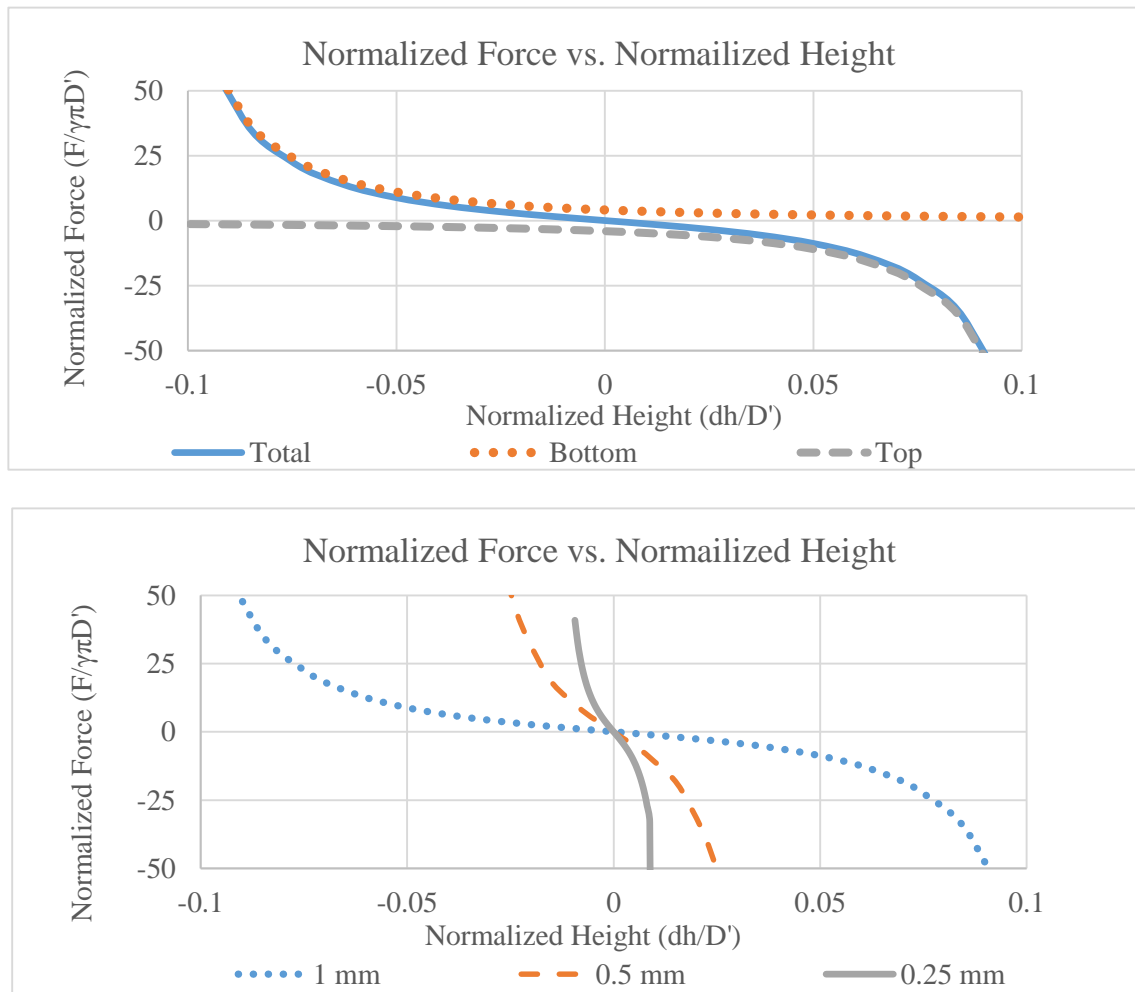


Figure 6-11: Opposing droplet configuration for optimal stiffness and precise z-location. Top: the normalized force from both the top and the bottom droplets are plotted against the normalized height (change in height divided by the nominal droplet diameter,  $dh/D'$ ). The equilibrium height is 1 mm for both the top and bottom gap. Bottom: The gap height is fixed at 0.1, 0.5, and 0.25 mm. As the allowable gap height decreases, the stiffness of the bearing (slope of the lines) increases. The contact angle used in calculations was  $165^\circ$ , and the surface tension value used was 0.072 N/m.

### 6.5.1 Design Case 3 - Droplets with Fixed Gap

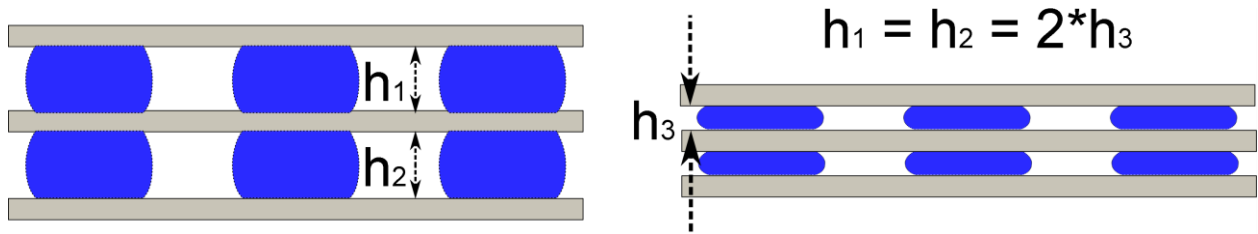


Figure 6-12: Case study 3 and 4: these cases evaluate the two opposing droplet configurations, and the impact on stiffness. Left: case 3, the equilibrium gap height  $h_1$  and  $h_2$  are 1 mm (same as in case study 1). Right: case 4, the equilibrium gap height  $h_3$  is half of the gap height in case 3.

Since viscous shear limits the maximum speed of the droplet-based bearing, the optimal design may require higher gaps (case study 1) while maintaining high stiffness (case study 2). However, for a given gap height, the droplet aspect ratio (droplet volume) will also have a strong impact on the viscous losses, so that it may be possible to optimize both of these parameters. The following case study examines the benefits of implementing a two-opposing droplet configuration.

As before, the contact angle and surface tension are held constant at  $110^\circ$  and  $0.072 \text{ N/m}$ , respectively, and type 1 wetting is used to provide a lower bound approximation of the stiffness. The same droplet volume in design case 1 was used with Equation 6-6 for calculations. The gap height (both  $h_1$  and  $h_2$ ) is 1 mm. The weight of the plate is not included under the assumption that the density of the plate is offset by the ambient liquid. The results are listed in Table 6-4. If the plate/ambient densities do not match, then the plate will be offset in the direction of gravity until the bearing force balances gravity. Higher stiffness designs would result in less gravitational error.

Table 6-4: Case study of droplet(s) with constant height (1 mm) and wetting area. The contact angle is 110° at the top and bottom. The diameter of the top wetting region is the same as in design case 1 (fixed).

# of droplets	Volume of each Droplet (μL)	Aspect Ratio (h/D)	Diameter of the drop at midpoint (mm)	Total Stiffness (N/m)	Minimum total area required (mm <sup>2</sup> )	Total projected length (mm)
1	36.3	0.147	6.8	6.62	36.3	13.6
3	16.6	0.217	4.6	8.63	49.9	27.6
5	12.6	0.25	4	10.66	62.8	40
7	10.8	0.27	3.7	12.6	75.3	51.8

The results suggest that with a given wetting area and gap height, the stiffness could be increased by a factor of 3 or more due to the symmetric droplets. It is worth it to point out that the case study presented here was based on the optimized force study (case 1). Therefore, at equilibrium height (the gap height is the same for the top and bottom), the total force is zero due to the preload. Either by increasing the droplet volume with the same wetting area, or by decreasing the wetting area with the same droplet volume, the stiffness could be further improved. This could also be accomplished by decreasing the gap height.

#### **6.5.2 Design Case 4 - Opposing Droplets with Fixed Gap and Preload (Reduced Gap Height)**

The last case follows the same parameters as in case 3. The wetting area and droplet volume are the same as in case 3, but the gap height is reduced by half (0.5 mm) for both the top and bottom. The results are listed in Table 6-5. The main difference in the resulting stiffness is that by reducing the gap height (a factor of 2), a 5 fold increase of the stiffness is possible (comparing the numbers between case 3 and 4).

Table 6-5: Case study of droplet(s) with constant height (0.5 mm), and wetting area. The contact angle is  $110^\circ$  at the top and bottom. The diameter of the top wetting region is the same as in case study 1 (fixed).

# of droplets	Volume of each Droplet ( $\mu\text{L}$ )	Aspect Ratio (h/D)	Diameter of the drop (mm)	Total Stiffness (N/m)	Minimum total area required ( $\text{mm}^2$ )	Total projected length (mm)
1	18.16	0.073	6.8	29.67	36.3	13.6
3	8.31	0.187	4.6	39.82	49.9	27.6
5	6.28	0.125	4	49.61	62.8	40
7	5.38	0.135	3.7	59.12	75.3	51.8

## 6.6 Conclusion

The normal force of a capillary bridge between two parallel surfaces was analyzed using both Laplace-based calculation, and simulation. Three types, symmetric wetting, top wetting, and constrained top wetting were presented. For top wetting and constrained top wetting, the operating range would need to be around or beyond the wetting boundary, which would cause larger force and higher stiffness.

The optimal design was shown to be the constraints on the wetting region combined with geometrical constraints on the top plate that enable effective contact angles above  $180^\circ$  at the edge of the wetting boundary. Higher stiffness, as well as larger supporting force was achieved by such design.

For ultimate precision, an opposing droplet configuration was proposed. Simplified force analysis showed a symmetrical stiffness response due to the preloading effect. The stiffness could be further fine-tuned by changing the total gap height. For linear droplet bearings actuated by electrowetting, a series of design cases was presented to demonstrate the advantage of using multiple droplets to support the same load. The larger actuation force capability of multiple droplets could improve the speed of the actuator. When designing such actuators, the total area



and the gap height should be the driving parameters to meet the required load and stiffness performance levels.

For opposing droplets, the stiffness of the droplet improves significantly with smaller aspect ratios ( $h/D < 0.1$ ). By introducing wetting contrast, the stiffness improved for higher aspect ratios (0.1 - 1), but the total force also decreased rapidly once the bottom contact area was less than the wetting region on top.

## CHAPTER 7: CONCLUSION AND FUTURE WORK

This dissertation's objective is to quantify key parameters which could be used to design a droplet-based mechanical actuator using the electrowetting phenomenon. The key actuation parameters include the actuation force, positioning accuracy and repeatability, device reliability, and the load carrying capability. The following discussion highlights the main conclusions of the study.

### 7.1 Key Contributions

#### 7.1.1 Electrowetting Force

Unlike other approximation methods - such as capillary height rise, contact angle change, and pressure variation - the electrowetting actuation force as a function of the fluid surface energy was experimentally measured for the first time by confining the droplet's shape to a square glass plate. By restraining the motion of the glass plate in the horizontal direction, the force during electrowetting actuation was measured as a function of the applied voltage and the interfacial tension of the fluid/ambient. The results validate the classical Young-Lippmann equation which governed the relationship between the electrowetting force, the applied voltage, and the surface tension of fluid/ambient. The study concluded that for maximum actuation force, higher surface tension fluids should be used in a droplet-based actuator. For a droplet carrying a solid plate, higher surface tension and higher voltage can achieve higher speed. However, lower surface tension droplets were able to achieve higher actuation speed when they were unconstrained by a plate. This study established the design foundation for droplet-based

actuators using electrowetting effect in terms of: the choice of fluids, the surface tension, and the speed limitations of the system.

### 7.1.2 Novel Electrowetting Actuation-based on Diodes

The second part of this study demonstrates two types of novel electrowetting actuations by embedding diodes into the electrowetting substrate. One is capable of fine positioning, and the other is better suited for large actuation distance. The first type of actuation used the electrochemical reaction between the actuation fluids and the metal substrate. By etching/passivating the electrode in-situ, the contacting interfaces act like two diodes connected back-to-back in series. By varying the input waveform's duty cycle, micro-stepping (sub-electrode motion control) of the droplet was demonstrated to be symmetric and non-linear about the center of the droplet. A simplified circuit model was used to derive the relationship of the input and the position of the droplet. The positioning of the droplet is within 0.2 mm ( $< 2.5\%$  of the droplet diameter) of the idealized model and repeatability error is  $< 0.07$  mm ( $< 0.8\%$  of the droplet diameter). This actuation scheme uses open-loop control to actuate an electrowetting-driven droplet with minimal wiring required. For droplet-based actuators, the micro-stepping eliminates the need for feedback sensing, while provide high positioning accuracy and repeatability. In addition, this actuation could also be applied to other electrowetting-driven droplet actuation in biological applications.

The second type of actuation uses semiconductor principles with embedded Schottky diodes to replace the electrochemical diodes in our previous continuous electrowetting substrate. In contrast to our previously demonstrated prototype, devices based on Schottky diodes reduced the minimum actuation voltage from 300 V to 150 V. In terms of reliability, up to two thousand cycles of repeated actuation were demonstrated in the Schottky diode-based device with no

performance degradation. By using high resistivity silicon, a voltage gradient is created when a potential is maintained between the end contacts. When a droplet bridged two or more diode sites, the diodes block the reverse current and thus creates a potential difference within the droplet which could then move the droplet towards the higher potential electrode. The advantage of this type of actuation is that only two electrodes are needed for large actuation distance (10X or more of the droplet diameter). The velocity of the droplet was measured in relation with the applied voltage and it was found experimentally that the average velocity scales with the applied voltage squared. The maximum velocity was measured to be as high as 240 mm/s. For a droplet-based mechanical actuator, the bi-directional continuous actuation could serve as the driving mechanism - similar to an electromagnetic servo motor - which could achieve high linear speed and large actuation force with minimal wiring.

### **7.1.3 Vertical Force and Stiffness Analysis**

The last part of the study uses the simulation software Surface Evolver to establish the design criteria for a droplet-based actuator in terms of vertical supporting force and stiffness. Depending on the design goal, the variables such as droplet volume, gap height, and the geometrical constraints for the droplet should be considered. The surface tension of the fluids should be as large as possible for optimal loading in the z direction. Due to the fact that the droplet will be driven by electrowetting, either wetting and/or geometrical constraints are needed to limit the relative movement between the droplet and the top plate. It was shown that by introducing additional geometrical constraints which limit the movement of the contact line, the stiffness of the droplet could be improved drastically. This could increase the working normal force of a droplet-based bearing in terms of the minimal gap height. In addition, a two droplet setup was proposed and analyzed in terms of force and stiffness. The results show superior

performance comparing to a single droplet. Additional case studies were performed to demonstrate the effect of single vs. multiple droplets. The results show that by using multiple droplets, the stiffness would increase, as well as the total actuation force from electrowetting. However, minimum required area would also increase as the number of droplet increases.

## **7.2 Future Work**

### **7.2.1 Force and Velocity Considerations**

From the electrowetting force and velocity measurements, the actuation force due to electrowetting was quantified. However, when comparing the electrowetting force and the drag force of the same droplet without the electrowetting effect, a large portion of the actuation force was not accounted for. Specifically, the measured electrowetting force for a constrained droplet was much larger than the measured friction drag force with no electrowetting effect. This indicates that there are additional dissipation mechanism(s) that are voltage dependent - possibly contact angle hysteresis, and dynamic contact line friction - which need to be addressed in future work. Also, for Schottky diode-based actuation, the velocity and time relation indicates a complex response with declining velocity after initial acceleration. This could be due to a possible electrowetting-dependent drag force, non-ideal electrical characteristics of the electrical elements such as the diodes, or coupling between the electrical and fluidic systems. Future work would be needed with concentration in measuring the drag force experimentally to quantify the behavior. A droplet actuation model needs to be developed which accounts for the following effects: the electrowetting actuation force, the speed dependent drag, the initial static friction from the substrate (contact angle hysteresis), the electrowetting force dependent drag, and the viscous drag from the ambient and within the droplet.

For stepping actuation, the idealized circuit model could also benefit from direct characterization of the actuation force. Once the actuation force is measured, the voltage of the droplet could be approximated, and a more refined circuit model that includes additional elements such as turn-on voltage and leakage current could be developed to further increase the precision of the droplet-based actuator.

As for the droplet bearings, the z-axis force and stiffness relation was established in the study by simulation. Experimental verification would be necessary to validate the simulated results. In addition, the x-y stiffness still needs further quantification. How a droplet-based bearing resists disturbances (the actuation via electrowetting) in the same plane could have a large impact on the maximum speed and precision for the actuator. Therefore, additional work is needed to establish the stiffness in the x-y plane.

### **7.2.2 Potential Applications and Future Directions**

Based on the findings of this work, a successful droplet-based mechanical actuator using electrowetting principle can be designed and implemented. The actuator can be used to further enhance the working range of currently available microscale actuators. Possible application areas include assembly of sub-millimeter components, linear or two-dimensional solid platforms that can be carried by droplets. If the droplet itself is used as the actuator, it is also possible to apply principles in hydraulic actuation in the macroscale; droplet-based pistons and fluidic circuits could be implemented. For biological applications, the actuator has the potential to generate droplets and assemble live cells, either for analysis, or tissue engineering.

The future research direction of droplet-based actuators should be concentrated in solving other technology related issues such as device fabrication and packaging. It is still very challenging to create sub-microliter water droplets with high repeatability due to the high surface

tension. For a droplet-based actuator, the volume uncertainty for each droplet has to be minimized. In addition, it is favorable to package the actuator inside a fluidic ambient so the gravity effect could be further reduced. The fabrication and packaging processes/methods will also have to be investigated.

## REFERENCES

1. Crane, N.B., et al., *Fluidic assembly at the microscale: progress and prospects*. Microfluidics and Nanofluidics, 2012. **14**(3-4): p. 383-419.
2. Smith, S.T. and Seugling, R.M., *Sensor and actuator considerations for precision, small machines*. Precision Engineering-Journal of the International Societies for Precision Engineering and Nanotechnology, 2006. **30**(3): p. 245-264.
3. Newport Corporation. 2016; Available from: <http://www.newport.com/>.
4. Kim, W.J. and Sa, Y.K., *Micro-extrusion of ECAP processed magnesium alloy for production of high strength magnesium micro-gears*. Scripta Materialia, 2006. **54**(7): p. 1391-1395.
5. Mehregany, M., Gabriel, K.J., and Trimmer, W.S.N., *Micro Gears and Turbines Etched from Silicon*. Sensors and Actuators, 1987. **12**(4): p. 341-348.
6. Judy, J.W., *Microelectromechanical systems (MEMS): fabrication, design and applications*. Smart Materials and Structures, 2001. **10**(6): p. 1115-1134.
7. Spearing, S.M., *Materials issues in microelectromechanical systems (MEMS)*. Acta Materialia, 2000. **48**(1): p. 179-196.
8. Spengen, W.M.v., Puers, R., and Wolf, I.D., *A physical model to predict stiction in MEMS*. Journal of Micromechanics and Microengineering, 2002. **12**(5): p. 702-713.
9. Bell, D.J., et al., *MEMS actuators and sensors: observations on their performance and selection for purpose*. Journal of Micromechanics and Microengineering, 2005. **15**(7): p. S153-S164.
10. Hubbard, N.B., Culpepper, M.L., and Howell, L.L., *Actuators for micropositioners and nanopositioners*. Applied Mechanics Reviews, 2006. **59**(1-6): p. 324-334.
11. Ouyang, P.R., et al., *Micro-motion devices technology: The state of arts review*. The International Journal of Advanced Manufacturing Technology, 2007. **38**(5-6): p. 463-478.
12. Chang, B., et al., *Low-height sharp edged patterns for capillary self-alignment assisted hybrid microassembly*. Journal of Micro-Bio Robotics, 2014. **9**(1-2): p. 1-10.
13. Mastrangeli, M., *The Fluid Joint: The Soft Spot of Micro- and Nanosystems*. Adv Mater, 2015. **27**(29): p. 4254-72.
14. Syms, R.R.A., et al., *Surface tension-powered self-assembly of microstructures - The state-of-the-art*. Journal of Microelectromechanical Systems, 2003. **12**(4): p. 387-417.



15. Liao, W.J., et al., *Tunable optical fiber filters with magnetic fluids*. Applied Physics Letters, 2005. **87**(15).
16. Mastrangeli, M., et al., *Challenges for Capillary Self-Assembly of Microsystems*. Ieee Transactions on Components Packaging and Manufacturing Technology, 2011. **1**(1): p. 133-149.
17. Hua, L. and Bailey, C., *Dynamic analysis of flip-chip self-alignment*. IEEE Transactions on Advanced Packaging, 2005. **28**(3): p. 475-480.
18. Berthier, J., et al., *Stabilization of the tilt motion during capillary self-alignment of rectangular chips*. Sensors and Actuators a-Physical, 2015. **234**: p. 180-187.
19. Harsh, K.F., Bright, V.M., and Lee, Y.C., *Solder self-assembly for three-dimensional microelectromechanical systems*. Sensors and Actuators a-Physical, 1999. **77**(3): p. 237-244.
20. Zimmermann, M., et al., *Capillary pumps for autonomous capillary systems*. Lab Chip, 2007. **7**(1): p. 119-25.
21. Leu, T.S. and Chang, P.Y., *Pressure barrier of capillary stop valves in micro sample separators*. Sensors and Actuators a-Physical, 2004. **115**(2-3): p. 508-515.
22. Fantoni, G., Hansen, H.N., and Santochi, M., *A new capillary gripper for mini and micro parts*. Cirp Annals-Manufacturing Technology, 2013. **62**(1): p. 17-20.
23. Mugele, F. and Baret, J.C., *Electrowetting: From basics to applications*. Journal of Physics-Condensed Matter, 2005. **17**(28): p. R705-R774.
24. Nelson, W.C. and Kim, C.J., *Droplet Actuation by Electrowetting-on-Dielectric (EWOD): A Review*. Journal of Adhesion Science and Technology, 2012. **26**(12-17): p. 1747-1771.
25. Jones, T.B., *An electromechanical interpretation of electrowetting*. 2005.
26. Crane, N.B., et al., *Bidirectional electrowetting actuation with voltage polarity dependence*. Applied Physics Letters, 2010. **96**(10): p. 104103.
27. Takei, A., Matsumoto, K., and Shomoyama, I., *Capillary motor driven by electrowetting*. Lab Chip, 2010. **10**(14): p. 1781-6.
28. Kaler, K. and Prakash, R., *Droplet Microfluidics for Chip-Based Diagnostics*. Sensors, 2014. **14**(12): p. 23283-23306.
29. Paik, P., et al., *Electrowetting-based droplet mixers for microfluidic systems*. Lab Chip, 2003. **3**(1): p. 28-33.
30. Fair, R.B., *Digital microfluidics: is a true lab-on-a-chip possible?* Microfluidics and Nanofluidics, 2007. **3**(3): p. 245-281.
31. Cho, S.K., Moon, H.J., and Kim, C.J., *Creating, transporting, cutting, and merging liquid droplets by electrowetting-based actuation for digital microfluidic circuits*. Journal of Microelectromechanical Systems, 2003. **12**(1): p. 70-80.

32. Berge, B. *Liquid lens technology: principle of electrowetting based lenses and applications to imaging*. in *Micro Electro Mechanical Systems, 2005. MEMS 2005. 18th IEEE International Conference on*. 2005.
33. Smith, N.R., et al., *Agile wide-angle beam steering with electrowetting microprisms*. *Optics Express*, 2006. **14**(14): p. 6557-6563.
34. Hayes, R.A. and Feenstra, B.J., *Video-speed electronic paper based on electrowetting*. *Nature*, 2003. **425**(6956): p. 383-5.
35. Hendriks, B.H.W., et al., *Electrowetting-based variable-focus lens for miniature systems*. *Optical Review*, 2005. **12**(3): p. 255-259.
36. Schultz, A., et al., *Detailed analysis of defect reduction in electrowetting dielectrics through a two-layer 'barrier' approach*. *Thin Solid Films*, 2013. **534**: p. 348-355.
37. Khodayari, M., Carballo, J., and Crane, N.B., *A material system for reliable low voltage anodic electrowetting*. *Materials Letters*, 2012. **69**: p. 96-99.
38. Dhindsa, M., Kuiper, S., and Heikenfeld, J., *Reliable and low-voltage electrowetting on thin parylene films*. *Thin Solid Films*, 2011. **519**(10): p. 3346-3351.
39. Guha, I.F., Kedzierski, J., and Abedian, B., *Low-voltage electrowetting on a lipid bilayer formed on hafnium oxide*. *Applied Physics Letters*, 2011. **99**(2): p. 024105.
40. Gong, J. and Kim, C.J., *All-electronic droplet generation on-chip with real-time feedback control for EWOD digital microfluidics*. *Lab Chip*, 2008. **8**(6): p. 898-906.
41. Ren, H., Fair, R.B., and Pollack, M.G., *Automated on-chip droplet dispensing with volume control by electro-wetting actuation and capacitance metering*. *Sensors and Actuators B-Chemical*, 2004. **98**(2-3): p. 319-327.
42. Sammarco, T.S. and Burns, M.A., *Thermocapillary pumping of discrete drops in microfabricated analysis devices*. *AIChE Journal*, 1999. **45**(2): p. 350-366.
43. Darhuber, A.A., et al., *Thermocapillary actuation of droplets on chemically patterned surfaces by programmable microheater arrays*. *Microelectromechanical Systems, Journal of*, 2003. **12**(6): p. 873-879.
44. Kotz, K.T., Noble, K.A., and Faris, G.W., *Optical microfluidics*. *Applied Physics Letters*, 2004. **85**(13): p. 2658.
45. Jiao, Z., et al., *Thermocapillary actuation of droplet in a planar microchannel*. *Microfluidics and Nanofluidics*, 2007. **5**(2): p. 205-214.
46. Ulman, A., *Formation and Structure of Self-Assembled Monolayers*. *Chem Rev*, 1996. **96**(4): p. 1533-1554.
47. *Asahi Glass | Chemicals*. 2016; Available from: <http://www.agc.com/kagaku/shinsei/cytop/en/about.html>.
48. Chaudhury, M.K. and Whitesides, G.M., *How to Make Water Run Uphill*. *Science*, 1992. **256**(5063): p. 1539-1541.

49. Bliznyuk, O., et al., *Smart design of stripe-patterned gradient surfaces to control droplet motion*. Langmuir, 2011. **27**(17): p. 11238-45.
50. Sun, C., et al., *Control of water droplet motion by alteration of roughness gradient on silicon wafer by laser surface treatment*. Thin Solid Films, 2008. **516**(12): p. 4059-4063.
51. Yang, J.T., et al., *Droplet Manipulation on a Hydrophobic Textured Surface With Roughened Patterns*. Journal of Microelectromechanical Systems, 2006. **15**(3): p. 697-707.
52. Linke, H., et al., *Self-propelled Leidenfrost droplets*. Phys Rev Lett, 2006. **96**(15): p. 154502.
53. Kruse, C., et al., *Self-propelled droplets on heated surfaces with angled self-assembled micro/nanostructures*. Microfluidics and Nanofluidics, 2015. **18**(5-6): p. 1417-1424.
54. Ok, J.T., et al., *Propulsion of droplets on micro- and sub-micron ratchet surfaces in the Leidenfrost temperature regime*. Microfluidics and Nanofluidics, 2010. **10**(5): p. 1045-1054.
55. Daniel, S., Chaudhury, M.K., and de Gennes, P.G., *Vibration-actuated drop motion on surfaces for batch microfluidic processes*. Langmuir, 2005. **21**(9): p. 4240-4248.
56. Ding, Z.W., Song, W.B., and Ziaie, B., *Sequential droplet manipulation via vibrating ratcheted microchannels*. Sensors and Actuators B-Chemical, 2009. **142**(1): p. 362-368.
57. Wixforth, A., et al., *Acoustic manipulation of small droplets*. Anal Bioanal Chem, 2004. **379**(7-8): p. 982-91.
58. Odenbach, S., *Ferrofluids - magnetically controlled suspensions*. Colloids and Surfaces a-Physicochemical and Engineering Aspects, 2003. **217**(1-3): p. 171-178.
59. Nguyen, N.-T., Ng, K.M., and Huang, X., *Manipulation of ferrofluid droplets using planar coils*. Applied Physics Letters, 2006. **89**(5): p. 052509.
60. Probst, R., et al., *Planar Steering of a Single Ferrofluid Drop by Optimal Minimum Power Dynamic Feedback Control of Four Electromagnets at a Distance*. J Magn Magn Mater, 2011. **323**(7): p. 885-896.
61. Gascoyne, P.R., et al., *Dielectrophoresis-based programmable fluidic processors*. Lab Chip, 2004. **4**(4): p. 299-309.
62. Jones, T.B., et al., *Frequency-Based Relationship of Electrowetting and Dielectrophoretic Liquid Microactuation*. Langmuir, 2003. **19**: p. 7646-7651.
63. Pollack, M.G., Fair, R.B., and Shenderov, A.D., *Electrowetting-based actuation of liquid droplets for microfluidic applications*. Applied Physics Letters, 2000. **77**(11): p. 1725-1726.
64. Moon, I. and Kim, J., *Using EWOD (electrowetting-on-dielectric) actuation in a micro conveyor system*. Sensors and Actuators a-Physical, 2006. **130**: p. 537-544.
65. Chevalliot, S., et al., *Analysis of Nonaqueous Electrowetting Fluids for Displays*. JOURNAL OF DISPLAY TECHNOLOGY, 2011. **7**(12): p. 649-656.

66. Mugele, F. and Baret, J.-C., *Electrowetting: from basics to applications*. Journal of Physics: Condensed Matter, 2005. **17**: p. R705-R774.
67. Papathanasiou, A.G., Papaioannou, A.T., and Boudouvis, A.G., *Illuminating the connection between contact angle saturation and dielectric breakdown in electrowetting through leakage current measurements*. Journal of Applied Physics, 2008. **103**(3): p. 034901.
68. Chevalliot, S., Kuiper, S., and Heikenfeld, J., *Experimental Validation of the Invariance of Electrowetting Contact Angle Saturation*. Journal of Adhesion Science and Technology, 2012. **26**(12-17): p. 1909-1930.
69. Kilaru, M.K., et al., *Strong charge trapping and bistable electrowetting on nanocomposite fluoropolymer: BaTi O<sub>3</sub> dielectrics*. Applied Physics Letters, 2007. **90**(21): p. 212906.
70. Raj, B., et al., *Ion and liquid dependent dielectric failure in electrowetting systems*. Langmuir, 2009. **25**(20): p. 12387-92.
71. Jones, T.B., *More about the electromechanics of electrowetting*. Mechanics Research Communications, 2009. **36**(1): p. 2-9.
72. Cooney, C.G., et al., *Electrowetting droplet microfluidics on a single planar surface*. Microfluidics and Nanofluidics, 2006. **2**(5): p. 435-446.
73. Ni, Q. and Crane, N.B., *Electrowetting Effect: Theory, Modeling, and Applications*. 2015: p. 1-14.
74. Crane, N.B., Mishra, P., and Volinsky, A.A., *Characterization of electrowetting processes through force measurements*. Rev Sci Instrum, 2010. **81**(4): p. 043902.
75. Dhindsa, M., et al., *Electrowetting without electrolysis on self-healing dielectrics*. Langmuir : the ACS journal of surfaces and colloids, 2011. **27**: p. 5665-70.
76. Nelson, C.W., Lynch, C.M., and Crane, N.B., *Continuous electrowetting via electrochemical diodes*. Lab Chip, 2011. **11**(13): p. 2149-52.
77. Khodayari, M., Hahne, B., and Crane, N.B., *Long Life Electrochemical Diodes for Continuous Electrowetting*. Journal of the Electrochemical Society, 2014. **161**(6): p. E105-E111.
78. Lee, J. and Kim, C.J., *Surface-tension-driven microactuation based on continuous electrowetting*. Journal of Microelectromechanical Systems, 2000. **9**(2): p. 171-180.
79. Schertzer, M.J., et al., *An empirically validated analytical model of droplet dynamics in electrowetting on dielectric devices*. Langmuir, 2010. **26**(24): p. 19230-8.
80. Chang, J.H. and Pak, J.J., *Twin-plate electrowetting for efficient digital microfluidics*. Sensors and Actuators B-Chemical, 2011. **160**(1): p. 1581-1585.
81. Cooney, C.G., et al., *Electrowetting droplet microfluidics on a single planar surface*. Microfluidics and Nanofluidics, 2006. **2**(5): p. 435-446.

82. Yoon, E., *A micropump driven by continuous electrowetting actuation for low voltage and low power operations*, in *Technical Digest. MEMS 2001. 14th IEEE International Conference on Micro Electro Mechanical Systems (Cat. No.01CH37090)*. 2001, IEEE. p. 487-490.
83. Beni, G., Hackwood, S., and Jackel, J.L., *Continuous electrowetting effect*. *Applied Physics Letters*, 1982. **40**(10): p. 912-14.
84. Vasudev, A. and Zhe, J., *A capillary microgripper based on electrowetting*. *Applied Physics Letters*, 2008. **93**: p. 103503.
85. Wang, H., et al. *The Capillary Force Actuator: Design, fabrication and characterization*. in *Micro Electro Mechanical Systems (MEMS), 2012 IEEE 25th International Conference on*. 2012.
86. Knospe, C.R. and Haj-Hariri, H., *Capillary force actuators: Modeling, dynamics, and equilibria*. *Mechatronics*, 2012. **22**(3): p. 251-256.
87. Jones, T.B., *An electromechanical interpretation of electrowetting*. *Journal of Micromechanics and Microengineering*, 2005. **15**: p. 1184-1187.
88. Jones, T.B., *On the relationship of dielectrophoresis and electrowetting*. *Langmuir*, 2002. **18**(11): p. 4437-4443.
89. Crane, N.B., Mishra, P., and Volinsky, A.A., *Characterization of electrowetting processes through force measurements*. *The Review of scientific instruments*, 2010. **81**: p. 043902.
90. Joanny, J.F. and Degennes, P.G., *A Model for Contact-Angle Hysteresis*. *Journal of Chemical Physics*, 1984. **81**(1): p. 552-562.
91. Li, F. and Mugele, F., *How to make sticky surfaces slippery: Contact angle hysteresis in electrowetting with alternating voltage*. *Applied Physics Letters*, 2008. **92**(24).
92. Lambert, P., et al. *Design of a Capillary Gripper for a Submillimetric Application*. in *IPAS*. 2016. Springer US.
93. Mastrangeli, M., et al., *Modeling capillary forces for large displacements*. *Microfluidics and Nanofluidics*, 2014. **18**(4): p. 695-708.
94. Ni, Q., Capecci, D.E., and Crane, N.B., *Electrowetting force and velocity dependence on fluid surface energy*. *Microfluidics and Nanofluidics*, 2015. **19**(1): p. 181-189.
95. Smith, N.R., et al., *Agile wide-angle beam steering with electrowetting micropisms*. *Optics Express*, 2006. **14**: p. 6557.
96. Hayes, R.A. and Feenstra, B.J., *Video-speed electronic paper based on electrowetting*. *Nature*, 2003. **425**: p. 383-5.
97. Cho, S.K., Moon, H., and Kim, C.-J., *Creating, transporting, cutting, and merging liquid droplets by electrowetting-based actuation for digital microfluidic circuits*. *Journal of Microelectromechanical Systems*, 2003. **12**: p. 70-80.

98. Sen, P., *A Fast Liquid-Metal Droplet Microswitch Using EWOD-Driven Contact-Line Sliding*. Journal of Microelectromechanical Systems, 2009. **18**: p. 174-185.
99. Takei, A., Matsumoto, K., and Shomoyama, I., *Capillary motor driven by electrowetting*. Lab on a chip, 2010. **10**: p. 1781-6.
100. Chen, J.H. and Hsieh, W.H., *Electrowetting-induced capillary flow in a parallel-plate channel*. Journal of colloid and interface science, 2006. **296**: p. 276-83.
101. Berthier, J., et al., *Actuation potentials and capillary forces in electrowetting based microsystems*. Sensors and Actuators A: Physical, 2007. **134**: p. 471-479.
102. Verheijen, H.J.J. and Prins, M.W.J., *Contact angles and wetting velocity measured electrically*. Review of Scientific Instruments, 1999. **70**: p. 3668.
103. Guan, L., et al., *Nanoscale Electrowetting Effects Studied by Atomic Force Microscopy*. The Journal of Physical Chemistry C, 2009. **113**: p. 661-665.
104. 't Mannetje, D., et al., *Electrically tunable wetting defects characterized by a simple capillary force sensor*. Langmuir : the ACS journal of surfaces and colloids, 2013. **29**: p. 9944-9.
105. Jones, T.B., *More about the electromechanics of electrowetting*. Mechanics Research Communications, 2009. **36**: p. 2-9.
106. Banpurkar, A.G., Nichols, K.P., and Mugele, F., *Electrowetting-based microdrop tensiometer*. Langmuir : the ACS journal of surfaces and colloids, 2008. **24**: p. 10549-51.
107. Papathanasiou, A.G. and Boudouvis, A.G., *Manifestation of the connection between dielectric breakdown strength and contact angle saturation in electrowetting*. Applied Physics Letters, 2005. **86**: p. 164102.
108. Chevalliot, S., Kuiper, S., and Heikenfeld, J., *Experimental Validation of the Invariance of Electrowetting Contact Angle Saturation*. Journal of Adhesion Science and Technology, 2012. **ahead-of-p**: p. 1-22.
109. Lu, H.-W., et al., *A diffuse-interface model for electrowetting drops in a Hele-Shaw cell*. Journal of Fluid Mechanics, 2007. **590**: p. 411-435.
110. Shabani, R. and Cho, H.J., *Flow rate analysis of an EWOD-based device: how important are wetting-line pinning and velocity effects?* Microfluidics and Nanofluidics, 2013. **15**: p. 587-597.
111. Song, J.H., et al., *A scaling model for electrowetting-on-dielectric microfluidic actuators*. Microfluidics and Nanofluidics, 2008. **7**: p. 75-89.
112. Nelson, W.C., Sen, P., and Kim, C.-J.C.J., *Dynamic contact angles and hysteresis under electrowetting-on-dielectric*. Langmuir : the ACS journal of surfaces and colloids, 2011. **27**: p. 10319-26.
113. Snoeijer, J.H. and Andreotti, B., *Moving Contact Lines: Scales, Regimes, and Dynamical Transitions*. Annual Review of Fluid Mechanics, 2013. **45**: p. 269-292.

114. Shikhmurzaev, Y.D., *The moving contact line on a smooth solid surface*. International Journal of Multiphase Flow, 1993. **19**: p. 589-610.
115. Blake, T.D., *The physics of moving wetting lines*. Journal of colloid and interface science, 2006. **299**: p. 1-13.
116. Blake, T.D., Clarke, A., and Stattersfield, E.H., *An Investigation of Electrostatic Assist in Dynamic Wetting*. Langmuir, 2000. **16**: p. 2928-2935.
117. Decamps, C. and De Coninck, J., *Dynamics of Spontaneous Spreading under Electrowetting Conditions*. Langmuir, 2000. **16**: p. 10150-10153.
118. Jiang, L. and Erickson, D., *Directed Self-Assembly of Microcomponents Enabled by Laser-Activated Bubble Latching*. Langmuir, 2011. **27**(17): p. 11259-11264.
119. Knospe, C.R. and Nezamoddini, S.A., *Capillary force actuation*. Journal of Micro-Nano Mechatronics, 2010. **5**(3-4): p. 57-68.
120. Griffith, E.J., Akella, S., and Goldberg, M.K., *Performance Characterization of a Reconfigurable Planar Array Digital Microfluidic System*. 2006: p. 329-356.
121. Lee, J., et al., *Electrowetting and electrowetting-on-dielectric for microscale liquid handling*. Sensors and Actuators a-Physical, 2002. **95**(2-3): p. 259-268.
122. Dhindsa, M., et al., *Electrowetting without electrolysis on self-healing dielectrics*. Langmuir, 2011. **27**(9): p. 5665-70.
123. Gao, L. and McCarthy, T.J., *Contact angle hysteresis explained*. Langmuir, 2006. **22**(14): p. 6234-7.
124. Nelson, W.C., Sen, P., and Kim, C.J., *Dynamic contact angles and hysteresis under electrowetting-on-dielectric*. Langmuir, 2011. **27**(16): p. 10319-26.
125. Heikenfeld, J. and Dhindsa, M., *Electrowetting on superhydrophobic surfaces: Present status and prospects*. Journal of Adhesion Science and Technology, 2008. **22**(3-4): p. 319-334.
126. Sen, P. and Kim, C.J., *A Fast Liquid-Metal Droplet Microswitch Using EWOD-Driven Contact-Line Sliding*. Journal of Microelectromechanical Systems, 2009. **18**(1): p. 174-185.
127. Arscott, S., *Electrowetting and semiconductors*. Rsc Advances, 2014. **4**(55): p. 29223-29238.
128. Olikh, O.Y., *Review and test of methods for determination of the Schottky diode parameters*. Journal of Applied Physics, 2015. **118**(2): p. 024502.
129. Arscott, S., *Moving liquids with light: photoelectrowetting on semiconductors*. Sci Rep, 2011. **1**: p. 184.
130. Jaeger, R.C., *Introduction to microelectronic fabrication*. 2nd ed. ed. Modular series on solid state devices ; v. 5. 2002, Upper Saddle River, N.J: Prentice Hall.

131. Ren, H., et al., *Dynamics of electro-wetting droplet transport*. Sensors and Actuators B: Chemical, 2002. **87**(1): p. 201-206.
132. Bavière, R., Boutet, J., and Fouillet, Y., *Dynamics of droplet transport induced by electrowetting actuation*. Microfluidics and Nanofluidics, 2007. **4**(4): p. 287-294.
133. Lambert, P., et al., *Design of a Capillary Gripper for a Submillimetric Application*, in *Precision Assembly Technologies for Mini and Micro Products: Proceedings of the IFIP TC5 WG5.5 Third International Precision Assembly Seminar (IPAS '2006), 19–21 February 2006, Bad Hofgastein, Austria*, S. Ratchev, Editor. 2006, Springer US: Boston, MA. p. 3-10.
134. Carter, W.C., *The Forces and Behavior of Fluids Constrained by Solids*. Acta Metallurgica, 1988. **36**(8): p. 2283-2292.
135. Fortes, M.A., *Axisymmetric Liquid Bridges between Parallel Plates*. Journal of Colloid and Interface Science, 1982. **88**(2): p. 338-352.
136. Chan, M.L., et al., *Design and characterization of MEMS micromotor supported on low friction liquid bearing*. Sensors and Actuators a-Physical, 2012. **177**: p. 1-9.
137. Liu, T.L., et al. *Electrostatic bottom-driven rotary stage on multiple conductive liquid-ring bearings*. in *Micro Electro Mechanical Systems (MEMS), 2013 IEEE 26th International Conference on*. 2013.
138. Sun, G.Y., et al., *Electrostatic Side-Drive Rotary Stage on Liquid-Ring Bearing*. Journal of Microelectromechanical Systems, 2014. **23**(1): p. 147-156.
139. Yoxall, B.E., et al., *Rotary Liquid Droplet Microbearing*. Journal of Microelectromechanical Systems, 2012. **21**(3): p. 721-729.
140. Lambert, P., et al., *Comparison between two capillary forces models*. Langmuir, 2008. **24**(7): p. 3157-3163.
141. Brakke, K., *The Surface Evolver*. Exp. Math, 1992. **1**: p. 141.
142. Mastrangeli, M., et al., *Lateral capillary forces of cylindrical fluid menisci: a comprehensive quasi-static study*. Journal of Micromechanics and Microengineering, 2010. **20**(7): p. 075041.



## APPENDIX A: COPYRIGHT PERMISSIONS

Below is the copyright permission from the publisher for the use of Figure 2-2.

### JOHN WILEY AND SONS LICENSE TERMS AND CONDITIONS

Feb 24, 2016

This Agreement between Qi Ni ("You") and John Wiley and Sons ("John Wiley and Sons") consists of your license details and the terms and conditions provided by John Wiley and Sons and Copyright Clearance Center.

License Number	3814931229122
License date	Feb 23, 2016
Licensed Content Publisher	John Wiley and Sons
Licensed Content Publication	AIChE Journal
Licensed Content Title	Thermocapillary pumping of discrete drops in microfabricated analysis devices
Licensed Content Author	Timothy S. Sammarco, Mark A. Burns
Licensed Content Date	Apr 16, 2004
Pages	17
Type of use	Dissertation/Thesis
Requestor type	University/Academic
Format	Print and electronic
Portion	Figure/table
Number of figures/tables	1
Original Wiley figure/table number(s)	Figure 1
Will you be translating?	No
Title of your thesis / dissertation	Droplet Based Mechanical Actuation Utilizing Electrowetting Effect
Expected completion date	May 2016
Expected size (number of pages)	80
Requestor Location	Qi Ni 7235 55th Ave. N.  SAINT PETERSBURG, FL 33709 United States Attn: Qi Ni
Billing Type	Invoice
Billing Address	Qi Ni 7235 55th Ave. N.  Saint Petersburg, FL 33709 United States Attn: Qi Ni

Below is the copyright permission from the publisher for the use of Figure 2-4.

**SPRINGER LICENSE  
TERMS AND CONDITIONS**

Feb 24, 2016

This is a License Agreement between Qi Ni ("You") and Springer ("Springer") provided by Copyright Clearance Center ("CCC"). The license consists of your order details, the terms and conditions provided by Springer, and the payment terms and conditions.

**All payments must be made in full to CCC. For payment instructions, please see information listed at the bottom of this form.**

License Number	3815460693514
License date	Feb 24, 2016
Licensed content publisher	Springer
Licensed content publication	Microfluids and Nanofluids
Licensed content title	Self-propelled droplets on heated surfaces with angled self-assembled micro/nanostructures
Licensed content author	Corey Kruse
Licensed content date	Jan 1, 2015
Volume number	18
Issue number	5
Type of Use	Thesis/Dissertation
Portion	Figures/tables/illustrations
Number of figures/tables/illustrations	1
Author of this Springer article	No
Order reference number	None
Original figure numbers	Fig.1
Title of your thesis / dissertation	Droplet Based Mechanical Actuation Utilizing Electrowetting Effect
Expected completion date	May 2016
Estimated size(pages)	80
Total	0.00 USD
Terms and Conditions	

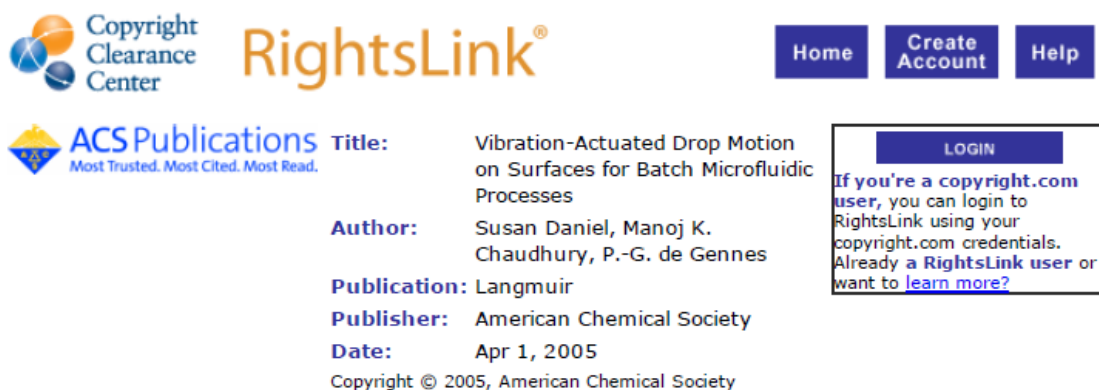
**Introduction**

The publisher for this copyrighted material is Springer. By clicking "accept" in connection with completing this licensing transaction, you agree that the following terms and conditions apply to this transaction (along with the Billing and Payment terms and conditions established by Copyright Clearance Center, Inc. ("CCC"), at the time that you opened your Rightslink account and that are available at any time at <http://myaccount.copyright.com>).

**Limited License**

With reference to your request to reuse material on which Springer controls the copyright,

Below is the copyright permission from the publisher for the use of Figure 2-5.



The screenshot shows the Copyright Clearance Center RightsLink interface. At the top left is the Copyright Clearance Center logo. To its right is the RightsLink logo. Further right are three buttons: Home, Create Account, and Help. Below the logo is the ACS Publications logo with the tagline "Most Trusted. Most Cited. Most Read." To the right of the ACS logo is the article information:

**Title:** Vibration-Actuated Drop Motion on Surfaces for Batch Microfluidic Processes  
**Author:** Susan Daniel, Manoj K. Chaudhury, P.-G. de Gennes  
**Publication:** Langmuir  
**Publisher:** American Chemical Society  
**Date:** Apr 1, 2005  
Copyright © 2005, American Chemical Society

On the right side of the interface, there is a LOGIN button and a text box that reads: "If you're a copyright.com user, you can login to RightsLink using your copyright.com credentials. Already a RightsLink user or want to learn more?"

#### PERMISSION/LICENSE IS GRANTED FOR YOUR ORDER AT NO CHARGE

This type of permission/license, instead of the standard Terms & Conditions, is sent to you because no fee is being charged for your order. Please note the following:

- Permission is granted for your request in both print and electronic formats, and translations.
- If figures and/or tables were requested, they may be adapted or used in part.
- Please print this page for your records and send a copy of it to your publisher/graduate school.
- Appropriate credit for the requested material should be given as follows: "Reprinted (adapted) with permission from (COMPLETE REFERENCE CITATION). Copyright (YEAR) American Chemical Society." Insert appropriate information in place of the capitalized words.
- One-time permission is granted only for the use specified in your request. No additional uses are granted (such as derivative works or other editions). For any other uses, please submit a new request.

If credit is given to another source for the material you requested, permission must be obtained from that source.

BACK

CLOSE WINDOW

Copyright © 2016 Copyright Clearance Center, Inc. All Rights Reserved. [Privacy statement](#). [Terms and Conditions](#). Comments? We would like to hear from you. E-mail us at [customercare@copyright.com](mailto:customercare@copyright.com)

Below is the copyright permission from the publisher for the use of Figure 2-10.



The screenshot shows the IEEE RightsLink interface. At the top left is the Copyright Clearance Center logo. To its right is the RightsLink logo. Further right are navigation buttons for Home, Create Account, and Help. Below the logo is a blue box with the IEEE logo and the text: 'Requesting permission to reuse content from an IEEE publication'. To the right of this box is a list of metadata: Title: A Capillary Microgripper Using Electrowetting; Conference Proceedings: University/Government/Industry Micro/Nano Symposium, 2008. UGIM 2008. 17th Biennial; Author: Abhay Vasudev; Jiang Zhe; Publisher: IEEE; Date: 13-16 July 2008; Copyright © 2008, IEEE. To the right of the metadata is a LOGIN button and a text box that says: 'If you're a copyright.com user, you can login to RightsLink using your copyright.com credentials. Already a RightsLink user or want to learn more?'.

### Thesis / Dissertation Reuse

**The IEEE does not require individuals working on a thesis to obtain a formal reuse license, however, you may print out this statement to be used as a permission grant:**

*Requirements to be followed when using any portion (e.g., figure, graph, table, or textual material) of an IEEE copyrighted paper in a thesis:*

- 1) In the case of textual material (e.g., using short quotes or referring to the work within these papers) users must give full credit to the original source (author, paper, publication) followed by the IEEE copyright line © 2011 IEEE.
- 2) In the case of illustrations or tabular material, we require that the copyright line © [Year of original publication] IEEE appear prominently with each reprinted figure and/or table.
- 3) If a substantial portion of the original paper is to be used, and if you are not the senior author, also obtain the senior author's approval.

*Requirements to be followed when using an entire IEEE copyrighted paper in a thesis:*

- 1) The following IEEE copyright/ credit notice should be placed prominently in the references: © [year of original publication] IEEE. Reprinted, with permission, from [author names, paper title, IEEE publication title, and month/year of publication]
- 2) Only the accepted version of an IEEE copyrighted paper can be used when posting the paper or your thesis on-line.
- 3) In placing the thesis on the author's university website, please display the following message in a prominent place on the website: In reference to IEEE copyrighted material which is used with permission in this thesis, the IEEE does not endorse any of [university/educational entity's name goes here]'s products or services. Internal or personal use of this material is permitted. If interested in reprinting/republishing IEEE copyrighted material for advertising or promotional purposes or for creating new collective works for resale or redistribution, please go to [http://www.ieee.org/publications\\_standards/publications/rights/rights\\_link.html](http://www.ieee.org/publications_standards/publications/rights/rights_link.html) to learn how to obtain a License from RightsLink.

If applicable, University Microfilms and/or ProQuest Library, or the Archives of Canada may supply single copies of the dissertation.

Below is the copyright permission from the publisher for the use of Figure 2-11.

**ELSEVIER LICENSE  
TERMS AND CONDITIONS**

Feb 25, 2016

This is a License Agreement between Qi Ni ("You") and Elsevier ("Elsevier") provided by Copyright Clearance Center ("CCC"). The license consists of your order details, the terms and conditions provided by Elsevier, and the payment terms and conditions.

**All payments must be made in full to CCC. For payment instructions, please see information listed at the bottom of this form.**

Supplier	Elsevier Limited The Boulevard, Langford Lane Kidlington, Oxford, OX5 1GB, UK
Registered Company Number	1982084
Customer name	Qi Ni
Customer address	7235 55th Ave. N. Saint Petersburg, FL 33709
License number	3815780937690
License date	Feb 25, 2016
Licensed content publisher	Elsevier
Licensed content publication	Sensors and Actuators A: Physical
Licensed content title	Using EWOD (electrowetting-on-dielectric) actuation in a micro conveyor system
Licensed content author	Ilju Moon, Joonwon Kim
Licensed content date	14 August 2006
Licensed content volume number	130
Licensed content issue number	n/a
Number of pages	8
Start Page	537
End Page	544
Type of Use	reuse in a thesis/dissertation
Portion	figures/tables/illustrations
Number of figures/tables/illustrations	1
Format	both print and electronic
Are you the author of this Elsevier article?	No
Will you be translating?	No
Original figure numbers	Fig 2

Below is the copyright permission from the publisher for the use of chapter 3.



# RightsLink®

[Home](#)
[Account Info](#)
[Help](#)



**Title:** Electrowetting force and velocity dependence on fluid surface energy

**Author:** Qi Ni

**Publication:** Microfluidics and Nanofluidics

**Publisher:** Springer

**Date:** Jan 1, 2015

Copyright © 2015, Springer-Verlag Berlin Heidelberg

Logged in as:  
Qi Ni

Account #:  
3000999311

LOGOUT

### Order Completed

Thank you for your order.

This Agreement between Qi Ni ("You") and Springer ("Springer") consists of your license details and the terms and conditions provided by Springer and Copyright Clearance Center.

Your confirmation email will contain your order number for future reference.

[Get the printable license.](#)

License Number	3866961313353
License date	May 13, 2016
Licensed Content Publisher	Springer
Licensed Content Publication	Microfluidics and Nanofluidics
Licensed Content Title	Electrowetting force and velocity dependence on fluid surface energy
Licensed Content Author	Qi Ni
Licensed Content Date	Jan 1, 2015
Licensed Content Volume	19
Licensed Content Issue	1
Type of Use	Thesis/Dissertation
Portion	Full text
Number of copies	2
Author of this Springer article	Yes and you are the sole author of the new work
Order reference number	None
Title of your thesis / dissertation	Droplet Based Mechanical Actuation Utilizing Electrowetting Effect
Expected completion date	May 2016
Estimated size(pages)	80
Requestor Location	Qi Ni 7235 55th Ave. N.  SAINT PETERSBURG, FL 33709 United States Attn: Qi Ni
Billing Type	Invoice
Billing address	Qi Ni 7235 55th Ave. N.  Saint Petersburg, FL 33709 United States Attn: Qi Ni

## APPENDIX B: SURFACE EVOLVER SIMULATION CODE

```
gravity_constant 0 // 0gravity
parameter dr_volume = 10e-9 //[m^3]*10^-9 --> [uL]
parameter top_angle = 165 // interior angle between plane and surface, degrees
parameter bottom_angle = 165 // interior angle between plane and surface, degrees
parameter top_angle_inside = 10 // interior angle of the top surface
parameter bottom_angle_inside = 165 // interior angle of the bottom surface
parameter xoff = 0 //offset of teh top surface
parameter yoff = 0 // offset of teh bottom surface
parameter rad_top = 0.001
parameter rad_bottom = 0.001
parameter zh = 0.001 // separation of plates [m]
parameter RD = 1 //relative density
parameter LV_tension = 0.072 // surface tensin , only needed when setting constraint 1 with -
cos(theta)*gamma
#define dr_size (sqrt(dr_volume/zh))
#define side_d (dr_size/2) //
#define outside (sqrt(dr_volume/zh)+0.005)
#define vol dr_size^2*zh
//define toparea sum(facet where color == red, area)
//define bottomarea sum(facet where color == green, area)
// Contact surface tensions
#define UPPERT (cos(top_angle*pi/180)*LV_tension) // virtual tension of facet on plane
#define LOWERT (-cos(bottom_angle*pi/180)*LV_tension)
#define upper_inside_t (cos(top_angle_inside*pi/180)*LV_tension)
#define lower_inside_t (-cos(bottom_angle_inside*pi/180)*LV_tension)
quantity Atop INFO_ONLY method edge_vector_integral
vector_integrand:
  q1: -(y)
  q2: 0
  q3: 0
quantity Abottom INFO_ONLY method edge_vector_integral
vector_integrand:
  q1: -(y)
  q2: 0
  q3: 0
constraint 1 /* the lower plate */
formula: z = 0
```

```

energy: // for contact angle
e1: -y/2 / (x^2 + y^2) *
    ((x^2 + y^2 < rad_bottom^2) ?
    (lower_inside_t * (x^2 + y^2)) : \
    (lower_inside_t * rad_bottom^2 + LOWERT * (x^2 + y^2 - rad_bottom^2)))
e2: x/2 / (x^2 + y^2) *
    ((x^2 + y^2 < rad_bottom^2) ?
    (lower_inside_t * (x^2 + y^2)) : \
    (lower_inside_t * rad_bottom^2 + LOWERT * (x^2 + y^2 - rad_bottom^2)))
e3: 0
constraint 2 /* the upper plate */
formula: z = zh
energy: // for contact angle and gravitational energy under missing facets
e1: (y-yoff)/2 / ((x-xoff)^2 + (y-yoff)^2) *
    (((x-xoff)^2 + (y-yoff)^2 < rad_top^2) ?
    (upper_inside_t * ((x-xoff)^2 + (y-yoff)^2)) : \
    (upper_inside_t * rad_top^2 + UPPERT * ((x-xoff)^2 + (y-yoff)^2 - rad_top^2)))
e2: -(x-xoff)/2 / ((x-xoff)^2 + (y-yoff)^2) *
    (((x-xoff)^2 + (y-yoff)^2 < rad_top^2) ?
    (upper_inside_t * ((x-xoff)^2 + (y-yoff)^2)) : \
    (upper_inside_t * rad_top^2 + UPPERT * ((x-xoff)^2 + (y-yoff)^2 - rad_top^2)))
e3: 0
content: // This is independent of pad shape
c1: (y-yoff) * zh / 2
c2: -(x-xoff) * zh / 2
c3: 0
constraint 3 nonnegative //lower barrier
formula: z
constraint 4 nonpositive //upper barrier
formula: z - zh
constraint 5 //display top wetting
formula: x^2 + y^2 = rad_top^2
constraint 6 // display lower wetting
formula: x^2 + y^2 = rad_bottom^2
//constraint 5 nonpositive
//formula: (x-(dr_size/2))^2 +(y-(dr_size/2))^2 - RR^2
vertices
1 side_d side_d 0 constraint 1 /* 4 vertices on lower plate */
2 -side_d side_d 0 constraint 1
3 -side_d -side_d 0 constraint 1
4 side_d -side_d 0 constraint 1
5 side_d side_d zh constraint 2 /* upper plate */
6 -side_d side_d zh constraint 2
7 -side_d -side_d zh constraint 2
8 side_d -side_d zh constraint 2

```



```

9 0.005      0.005      0.0 /* for lower plane */
10 0.005     -0.005     0.0
11 -0.005    -0.005     0.0
12 -0.005    0.005     0.0
13 0.005     0.005     zh /* for upper plane */
14 0.005     -0.005     zh
15 -0.005    -0.005     zh
16 -0.005    0.005     zh
edges /* given by endpoints and attribute */
1 1 2  constraint 1 Abottom /* 4 edges on lower plate */
2 2 3  constraint 1 Abottom
3 3 4  constraint 1 Abottom
4 4 1  constraint 1 Abottom

5 5 6  constraint 2 Atop /* upper plate */
6 6 7  constraint 2 Atop
7 7 8  constraint 2 Atop
8 8 5  constraint 2 Atop
9 1 5  constraints 3,4
10 2 6  constraints 3,4
11 3 7  constraints 3,4
12 4 8  constraints 3,4
13 9 10 no_refine bare constraint 6 /* for lower plate display only */
14 10 11 no_refine bare constraint 6
15 11 12 no_refine bare constraint 6
16 12 9  no_refine bare constraint 6
17 13 14 no_refine bare constraint 5 /* for upper plate display only */
18 14 15 no_refine bare constraint 5
19 15 16 no_refine bare constraint 5
20 16 13 no_refine bare constraint 5
faces /* given by oriented edge loop */
1 1 10 -5 -9 constraints 3,4 tension LV_tension color green
2 2 11 -6 -10 constraints 3,4 tension LV_tension color green
3 3 12 -7 -11 constraints 3,4 tension LV_tension color green
4 4 9 -8 -12 constraints 3,4 tension LV_tension color green
//5 13 14 15 16 no_refine density 0 fixed color -1 //green /* lower plate for display */
//6 17 18 19 20 no_refine density 0 fixed color -1 //red /* upper plate for display */
//7 1 2 3 4 density 0 color green
//8 5 6 7 8 density 0 color red
bodies /* one body, defined by its oriented faces */
1 1 2 3 4 volume dr_volume density 1000*RD
read
s
q

```

```

re := {refine edges where on_constraint 1 }
re1 := {refine edges where on_constraint 2}
target_tolerance := 1e-15

// vertical force on upper pad by central differences.
dz := .00005
do_zforce := { oldzh := zh; zh := zh + dz;
  set vertex z z+dz*z/oldzh; recalc; // uniform stretch
  energy1 := total_energy -
    body[1].pressure*(body[1].volume - body[1].target);
  oldzh := zh; zh := zh - 2*dz;
  set vertex z z-2*dz*z/oldzh; recalc; // uniform stretch
  energy2 := total_energy -
    body[1].pressure*(body[1].volume - body[1].target);
  zforce := -(energy1-energy2)/2/dz;
  printf "vertical force: %20.15f\n",zforce;
  // restore everything
  oldzh := zh; zh := zh + dz;
  set vertex z z+dz*z/oldzh; recalc; // uniform stretch
}

// Typical evolution
gogo := {re; re1; g50; re; re1; r; g50; u; V 100; V 100; g50; r; u; V 100; g50; r; u; V 10; hessian;
g 50; u; u; u; V 100; hessian; v;
  do_zforce;
}

// find bottom and top contact angles
botedge := {
  foreach facet ff where ff.edge[1] on_constraint 1 ||
  ff.edge[2] on_constraint 1 || ff.edge[3] on_constraint 1 do
  printf "cos theta=%f,\ttheta=%f\n", ff.x3/ff.area, 180/pi*acos(ff.x3/ff.area); }

topedge := {
  foreach facet ff where ff.edge[1] on_constraint 2 ||
  ff.edge[2] on_constraint 2 || ff.edge[3] on_constraint 2 do
  printf "cos theta=%f,\ttheta=%f\n", ff.x3/ff.area, 180-180/pi*acos(ff.x3/ff.area); }

//unit step for force calculation
EPS := .00005

// Ken Brakke's generic force calculation method
forcex := {
  olde := TOTAL_ENERGY;

```

```

oldv := body[1].volume;
set vertex x (x>zh)?(x+EPS):(x + EPS*(x/zh));
recalc;
vdiff:=body[1].volume-oldv;
set vertex x (x>zh)?(x-EPS):(x - EPS*(x/zh));
PRINT -(TOTAL_ENERGY - olde-body[1].pressure*vdiff)/EPS;
recalc; }

forcey := {
olde := TOTAL_ENERGY;
oldv := body[1].volume;
set vertex y (y>zh)?(y+EPS):(y + EPS*(y/zh));
recalc;
vdiff:=body[1].volume-oldv;
set vertex y (y>zh)?(y-EPS):(y - EPS*(y/zh));
PRINT -(TOTAL_ENERGY - olde-body[1].pressure*vdiff)/EPS;
recalc; }

forcez := {
olde := TOTAL_ENERGY;
oldv := body[1].volume;
set vertex z z + EPS*(z/zh);
zh := zh + EPS;
// Zuping := EPS;
recalc;
vdiff:=body[1].volume-oldv;
new_energy_1 := TOTAL_ENERGY - body[1].pressure * vdiff;

set vertex z z - 2*EPS*(z/zh);
zh := zh - 2*EPS;
recalc;
new_energy_2 := total_energy - body[1].pressure *
                (body[1].volume - body[1].target);
force_z := -(new_energy_1 - new_energy_2)/2/EPS;

set vertex z z + EPS*(z/zh);
zh := zh + EPS;
recalc; }

// These are the evolve parameters

longest := 1.5 * rad_top // Just < largest initial length
shortest := 0.000001 // whatever
mini := 0.03 * zh

```

```

gos := 60
iters := 1

// Report gives the current status.
report := { v; c; printf "Max length= %f, min length= %f, target
%f\n\n",longest,(shortest>longest/3)?longest/3:shortest,mini; }

// Go-on just evolves "gos" times or until the scale gets ridiculously small.
goon := {g; jj:=1; if scale>1e-8 then {
  while(jj<gos && scale>1e-6) do {g; jj:=jj+1;}}

// Iterate combines edge refinement, tiny edge elimination, and evolution/
// equiangulation; with vertex averaging for a coarse mesh.
iterate := {
  refine edges where length >= longest;
  delete edges where length < longest/3 and length < shortest;
  u; u; if longest > 2*mini then { V; u; };
  goon; }

// Evolve uses iterate with slow reduction of the maximum edge length to
// robustly approach a good solution on a fine mesh.
evolve := {
  while longest >= mini do {
    report;
    longest := longest * 0.9;
    u;
    iterate;
    if iters>1 then {
      ii:=2;
      while ii < iters do {
        u;
        iterate;
        ii := ii+1; };
      iterate; };
    report; do_zforce;}

keepon := {
  gos := 20;
  ii := 1;
  while ii <= 10 do {
    V; iterate; report; ii := ii +1;
  }
}

// output data to file

```

```

printf "" >>> "outputfile.dat"
printf
"LV_tension\tVolume\tHeight\tCA_top\tCA_bottom\tPressure\tArea_top\tArea_bottom\tzforce\n"
>> "outputfile.dat";

gogo2 := {gogo;
  printf
"%15.15g\t%15.15g\t%15.15g\t%15.15g\t%15.15g\t%15.15g\t%15.15g\t%15.15g\t%15.15g\n",
LV_tension, body[1].volume, zh, top_angle, bottom_angle,
  body[1].pressure, Atop.value, Abottom.value, zforce >> "outputfile.dat";
}

gogo3 := {evolve; printf
"%15.15g\t%15.15g\t%15.15g\t%15.15g\t%15.15g\t%15.15g\t%15.15g\t%15.15g\t%15.15g\n",
LV_tension, body[1].volume, zh, top_angle, bottom_angle,
  body[1].pressure, Atop.value, Abottom.value, zforce >> "outputfile.dat"; }

loop_gogo := { for ( htvar := 0.00039 ; htvar >= 0.0001333333333333 ; htvar -=
1.7777777777778E-6 ) //use gogo

  for (cavar := 100 ; cavar <= 165 ; cavar += 5)
  { replace_load "droplet_between_plate_different_angle.fe";
    zh := htvar; top_angle := cavar; bottom_angle := cavar;
    dr_size := sqrt(dr_volume/zh);

    gogo2;

  };
}
loop_gogo2 := { for ( htvar := 0.0015 ; htvar <= 0.004 ; htvar += 0.0001) //use evolve
//for (cavar := 100 ; cavar <= 165 ; cavar += 5)

  { replace_load "droplet_between_plate_different_angle.fe";
    zh := htvar;

//top_angle := cavar; bottom_angle := cavar;
    dr_size := sqrt(dr_volume/zh);

    longest := 1.5 * rad_top; // Just < largest initial length

```

```
shortest := 0.00001 ;  
mini := 0.03 * zh;  
gos := 60;  
iters := 1;  
gogo3;
```

```
};  
}
```

```
dd := {evolve; keepon; forcez;forcex;  
}
```